Title
Multimodality MRI-based Brain Network Analysis: Applications to Genetic Risk for Alzheimer's Disease

Author
Brown, Jesse Aaron

Publication Date
2013

Peer reviewed|Thesis/dissertation

UNIVERSITY OF CALIFORNIA

Los Angeles

Multimodality MRI-based Brain Network Analysis: Applications to Genetic Risk for Alzheimer's Disease

A dissertation submitted in partial satisfaction of the requirements for the degree

Doctor of Philosophy in Neuroscience

By

Jesse Aaron Brown

2013

ABSTRACT OF THE DISSERTATION

Multimodality MRI-based Brain Network Analysis:

Applications to Genetic Risk for Alzheimer's Disease

by

Jesse Aaron Brown

Doctor of Philosophy in Neuroscience

University of California, Los Angeles, 2013

Professor Susan Y. Bookheimer, Chair

Whole-brain structural and functional connectivity networks can be assessed using diffusion-weighted MRI (DW-MRI) and functional MRI (fMRI), respectively. When the brain is parcellated into its constituent subregions, specific methods quantify the relative connectivity strengths between pairs of regions. The calculation of connectivity between all pairs of regions produces a connectivity matrix. With such a matrix, mathematical methods from graph theory characterize the network for global properties of integration, segregation, and robustness. At the regional level, these methods quantify specific properties such as connection density, convergence, and isolation. In this work, we apply these methods to understand how the possession of the Apolipoprotein E ε4 allele, the primary genetic risk factor for late-onset Alzheimer's Disease (AD), contributes to global and local alterations of structural and functional connectivity. In Chapter 2, we find that DW-MRI-based fiber tractography networks in aging APOE-4 carriers exhibit accelerated negative correlations between age and clustering coefficient, a measure of local axonal connection density. This trend occurs simultaneously with reductions in global cortical thickness and decrease performance on episodic memory tests. In a highly similar population, we examined fMRI-based functional connectivity networks during

performance on an episodic memory task (Chapter 3). APOE-4 carriers demonstrated reduced activation during memory encoding in the entorhinal cortex, a locus of early disease change in Alzheimer's disease. The degree of activation in this region correlated with the amount of functional brain integration, suggesting a global basis for local alterations in neuronal activity. In Chapter 4, we assessed hippocampal functional and structural connectivity during episodic memory consolidation in healthy young adults. Results indicate that elevated functional connectivity in a hippocampal-cortical network was important for the process of consolidation. The structural connections of this network all traversed the parahippocamal gyrus, an area of known structural atrophy in individuals at genetic risk for AD. In Chapter 5 we describe a web-based tool for the public sharing and analysis of brain connectivity matrices, and then apply it to reveal substantial differences in the topology of whole brain structural and functional networks. Finally, Chapter 6 contains a model of cortico-hippocampal connectivity that unifies the findings from these studies.

The dissertation of Jesse Aaron Brown is approved.

Joaquin M. Fuster

Barbara Knowlton

Paul M. Thompson

Fred W. Sabb

Susan Y. Bookheimer, Committee Chair

University of California, Los Angeles

2013

I dedicate this work to my parents, who gave me the freedom to wander and wonder

TABLE OF CONTENTS

ACKNOWLEDGEMENTS

There are a great many people to thank and attribute for their considerable contributions to this work. First I have to thank my advisor, Dr. Susan Bookheimer. Susan is a brilliant, astoundingly prolific and diverse scientist. Her instincts are like lasers that cut holes through nonsense. Her encouragement and enthusiasm from the get-go were essential to the success of the projects described here, and to my growth in general. Her support for those in her extended lab family is a force to be reckoned with. I think my future postdoctoral advisor put it well when he described her as my "staunch advocate." She exudes trust in those that work for her and this creates a very collaborative, positive environment to work in – in short, a great place to be a graduate student.

The group of individuals that I have worked with in the Bookheimer and Cohen labs are unforgettable. From the early, sparsely populated days working with Arne Ekstrom, Nanthia Suthana, Ali Burggren, Teena Moody, Laurel Martin-Harris, James Kyle, and probable CIA operative Adam Bazih, to the "more particles in the same space makes everything hotter" recent times with Brian Renner, Mike Jones, Leonardo Cristov Moore, Kevin Terashima, Tessa Harrison, Pamelita Douglas, Hongjing Xia, Edward Lau, Andrew Cho, Agatha Lenartowicz, Wesley Kerr, and Malina Revett, I've always felt surrounded by warmth (emotional and physical), light (intellectual and flickering fluorescent), and energy (despite frequent outages). Oh, and Hoffman2, how could I forget you. Your parallelism knows no bounds.

My family was vital in the provision of freedom to find this path. There was never any "you should be a doctor, you should be a lawyer…" It was simply, do what you love, and that's the end of the story. I come from a family that is scientifically fascinated (and fascinating) but not scientists by trade. Nonetheless, they were always eager to hear about the latest findings in the brain world and tell their friends. I love my mom, dad, and sister to no end, and I'm looking forward to moving to San Francisco where my sister and I can be up close and in person.

A broad swath of friends ensured the preservation of, or at least the frequent return to, my sanity throughout graduate school. My old friends in San Diego were always a great escape from the science bubble. I love them all and they are without a doubt, being fruitful and multiplying. My new friends in Los Angeles have been great companions for exploring this megalopolis and kicking around the world at conferences in Barcelona, San Francisco, Beijing, Chicago, Quebec City, New Orleans, Brisbane, Oahu, and so on. A starving student I was not.

I've lost some people along the way and those are the breaks. People that are not in my life physically will not be forgotten and have left canyon-sized impressions on me.

My committee members – Joaquin Fuster, Barbara Knowlton, Fred Sabb, and Paul Thompson – have provided steady support and affirmation throughout this process and I'm very grateful for their contributions to this work. I also received considerable guidance and had many long science discussions with both Mark Cohen and Jack Van Horn, both of whom I consider unofficial members of my committee.

Lastly, I'd like to thank my previous advisor, Dr. Francisco Asturias. He took a chance on me when no one else had, encouraged me, and helped put me on this path. I had to knock on a lot of doors to break into this field. He answered, and I hope I will be able to do the same for others down the road.

I would be remiss not to mention the financial support that has kept me on my feet the past five plus years: a national research service award (F31AG035438-01), NIH grants P01-AG025831, AG13308, P50 AG 16570, MH/AG58156, MH52453, AG10123, M01-RR00865, and a Neuroimaging Training Program T31 training fellowship from NIH grants R90 DA022768 and T90 DA023422.

VITA

2003	B.A. Cognitive Science University of California, Berkeley Berkeley, California
2004-2005	Lead Quality Assurance Engineer Mforma Americas San Diego, California
2005-2007	Research Technician The Scripps Research Institute, Asturias Laboratory La Jolla, California
2008	UCLA Quality of Graduate Education Award FSL/Freesurfer Course Brisbane, Australia
2009	UCLA Neuroimaging Training Program Training Fellowship
2009	UCLA Quality of Graduate Education Award New Horizons in Brain Imaging Conference Waikaloa, Hawaii
2009-2012	Ruth L. Kirchstein National Research Service Award "Myelin Integrity and Connectivity in Subjects at Risk for Alzheimer Disease"
2010	Teaching Assistant Systems Neuroscience University of California, Los Angeles
2010	UCLA Brain Research Institute/Semel Institute Graduate Student Travel Award for Society for Neuroscience
2010	New Horizons in Brain Imaging Fellow Award Oahu, Hawaii
2013 (upcoming)	UCLA BRI Samuel Eiduson Student Lecture
2013-2015 (anticipated)	Postdoctoral Scholar University of California, San Francisco San Francisco, California

PUBLICATIONS

Jesse A. Brown, Jeffrey D. Rudie, Anita Bandrowski, John D. Van Horn, Susan Y. Bookheimer. The UCLA Multimodal Connectivity Database: A web-based platform for connectivity matrix sharing and complex network analysis (2012). *Frontiers in Neuroinformatics*. 28 November 2012.

Donatello Arienzo, Alex Leow, **Jesse A. Brown**, Liang Zhan, Johnson GadElkarim, Sarit Hovav, Jamie D. Feusner . Abnormal brain network organization in body dysmorphic disorder (2013). *Neuropsychopharmacology.* Jan 15 2013.

JD Rudie, **JA Brown**, D Beck-Pancer, LM Hernandez, EL Dennis, PM Thompson, SY

Bookheimer, M Dapretto. Altered Functional and Structural Brain Network Organization in Autism (2012). *Neuroimage: Clinical*. 15 November 2012.

JD Rudie, LM Hernandez, **JA Brown**, D Beck-Pancer, NL Colich, P Gorrindo, PM Thompson, DH Geschwind, SY Bookheimer, P Levitt, and M Dapretto. Autism-Associated Promoter Variant in MET Impacts Functional and Structural Brain Networks (2012). *Neuron.* Sep 6; 75(5):904-15.

John B. Colby, Jeffrey D. Rudie, **Jesse A. Brown**, Pamela K. Douglas, Mark S. Cohen, Zarrar Shehzad (2012). Insights into multimodal imaging classification of ADHD. Front. Syst. Neurosci. 6:59.

Emily L. Dennis, Neda Jahanshad, Jeffrey D. Rudie, **Jesse A. Brown**, Kori Johnson, Katie L. McMahon, Greig I. de Zubicaray, Grant Montgomery, Nicholas G. Martin, Margaret J. Wright, Susan Y. Bookheimer, Mirella Dapretto, Arthur W. Toga, Paul M. Thompson (2012). Abnormal Structural Brain Connectivity in Healthy Carriers of the Autism Risk Gene, CNTNAP2. *Brain Connectivity*, 2012 Feb 29.

Jesse A. Brown, Kevin H. Terashima, Alison C. Burggren, Linda M. Ercoli, Karen J. Miller, Gary W. Small, Susan Y. Bookheimer (2011). Brain network local interconnectivity loss in aging APOE-4 allele carriers. *Proc Natl Acad Sci*. Dec 20;108(51):20760-5.

Donix M, Ercoli LM, Siddarth P, **Brown JA**, Martin-Harris L, Burggren AC, Miller KJ, Small GW, Bookheimer SY (2011). Influence of Alzheimer Disease Family History and Genetic Risk on Cognitive Performance in Healthy Middle-Aged and Older People. *Am J Geriatr Psychiatry*. 2011 Feb 24.

Danielle S. Bassett, **Jesse A. Brown**, Vibhas Deshpande, Jean M. Carlson, Scott T. Grafton (2011). Conserved and variable architecture of human white matter connectivity. *Neuroimage* 54(2):1262-79.

Natcha Opalka, **Jesse Brown**, William J. Lane, Kelly-Anne F. Twist, Robert Landick, Francisco J. Asturias, Seth A. Darst (2010). Complete Structural Model of *Escherichia coli* RNA Polymerase from a Hybrid Approach. *PLoS Biology* 8(9): e1000483.

Yuchiro Takagi, Guillermo Calero, Hirofumi Komori, **Jesse A. Brown**, Andres Ehrensberger, Andy Hudmon, Francisco J. Asturias, Roger D. Kornberg (2006). Head Module Control of Mediator
Interactions. *Molecular Cell* 23:355-364.

Chapter 1

Introduction

The hippocampus and surrounding structures in the medial temporal lobe (MTL) are essential for episodic memory encoding and retrieval (Squire et al., 2004). The specialized role of the hippocampus in the formation of memories based on multisensory input is largely explained by its connectivity with the cerebral cortex. Cortical systems such as the visual processing network have a hierarchical connectivity pattern, aggregates input at progressively fewer number of regions, converging at the top of the hierarchy in the entorhinal cortex. This extrahippocampal area acts as a gateway that funnels inputs from the cortex into the hippocampus (Felleman and Van Essen, 1991).

Variations in the functional and structural properties of the MTL relate to individual variations in memory capability that result from intrinsic individual differences (Wig et al., 2008), normal aging , and disease processes such as Alzheimer's Disease (AD) (Greicius et al., 2004) (Salat et al., 2010). MTL structures are of particular interest in AD for two primary reasons: 1) episodic memory is the hallmark impairment in AD and 2) the earliest signs of cellular pathology in AD appear in the MTL (Braak and Braak, 1991; Gómez-Isla et al., 1996). The evolving understanding of AD indicates a network-based process of degeneration (Delbeuck et al., 2003) (Raj et al., 2012) with potential origins in the MTL (De Calignon et al., 2012). It is critical to investigate the earliest changes in MTL connectivity that occur in individuals with high risk for AD, as conferred by aging and genetic risk, in order to understand fundamental disease processes and develop highly sensitive biomarkers.

Recent advances in magnetic resonance imaging (MRI) hardware and pulse sequence development have enabled characterization of brain structure and function at improved spatial and temporal resolutions with higher signal to noise ratio and better tissue-type contrast. In parallel, rapidly advancing statistical and mathematical methods have enabled the assessment of brain connectivity, both functionally through blood-oxygen level dependent (BOLD) signal

covariations across the brain, and structurally through the detection of continuous streamlines of water diffusion parallel to myelinated fiber sheaths in the brain's white matter. These developments have enabled the characterization of the macroscale connectivity of an individual's brain possible within an hour-long MRI scanning session. Following is a description of these different MRI-based modalities and how they are used to quantify structural and functional brain connectivity within individuals. These measures are then compared across individuals to assess differences that appear to be driven by factors such as genetic variability and/or aging (see Chapters 2 and 3) and contribute to individual performance differences on psychological tests of memory performance (see Chapters 2 and 4).

DTI and Structural Network Analysis

Diffusion-weighted MRI is a technique that exploits the properties of water diffusion in different types of brain tissue to observe microstructural properties. The most common version of diffusion weighted MRI today is Diffusion Tensor Imaging, or DTI. Using modern 3T MRI scanners and DTI pulse sequences, one can obtain a highly accurate image of the brain's white matter. DTI tractography is a method for systematically tracking similar orientations of diffusion throughout the brain's white matter. The fiber bundles derived from DTI tractography are striking reproductions of known brain anatomical structures including the corpus callosum, corticospinal tract, corona radiata, arcute fasciculus, cingulum bundle, and so forth. Viewing software enables virtual dissections, isolation of specific bundles or subsets of fibers, and calculation of statistics regarding a track group's mean FA, mean length, or density of fibers. However, these analyses cannot reveal anything about global properties of fiber connectivity.

To deal with this problem, Patrick Hagmann and colleagues adapted a method to quantify global connectivity patterns from Diffusion Spectrum Imaging (a high-powered variant of DTI) tractography and analyze them in their seminal 2008 publication (Hagmann et al., 2008). For a group of five subjects, they obtained DSI and structural T1 scans. The structural scans

were analyzed with the Freesurfer software package (http://surfer.nmr.mgh.harvard.edu/) to obtain cortical parcellations (Fischl and Dale, 2000). These cortical regions were registered to DSI space. Next, all fibers were counted that connected any pair of regions. These track count were tabulated in a matrix, the structural connectivity matrix.

Structural connectivity matrices can equivalently be obtained with DTI tractography and fiber counting between brain regions derived either from a cortical parcellation or an atlas. These connectivity matrices, also known as graphs, describe the strength of connection between any pair of regions. These matrices are typically analyzed using graph theory, a branch of mathematics with methods to formally analyze a pattern of connections ("edges") between different entities ("nodes"). Specific regional and global metrics measure the local and global efficiency of information processing by quantifying the density of connections between regions and the distance over which information must transfer. This analysis technique has been increasingly employed in neuroimaging studies to characterize structural and functional brain networks (Bullmore and Sporns, 2009). Network-based measures of structural and functional brain connectivity are more sensitive to alterations that are not apparent in gross structure (e.g. cortical thickness or white matter integrity) because they consider each region's integration into the global unit rather than as an independent entity. Convergent evidence from these studies (Iturria-Medina et al., 2008) indicates that brain networks exhibit small worldness, a balance of two properties: high local efficiency, a dense clustering of connections among physically adjacent regions, and high global efficiency, a relatively short distance information must travel between any two nodes in the network. Small worldness is always calculated with respect to a network with an equivalent number of nodes and edges but a random wiring pattern.

It is hypothesized that the small-world configuration is an optimum reached by natural selection to balance functional segregation and integration, minimize metabolic cost, and maintain tolerance to injury or disease (Sporns, 2010). Recent studies suggest that the human brain has been optimized for nearly maximal cost efficiency (Bassett et al., 2010) and that

various neurological diseases may shift the brain towards suboptimal cost efficiency (Bassett et al., 2009). Individual variations in the white matter integrity of these networks have been shown to predict episodic long-term memory performance in older individuals (Charlton et al., 2010).

fMRI and Functional Connectivity

The coupling of blood oxygenation changes between different brain regions in fMRI data is known as functional connectivity. The degree of functional connectivity between two regions is statistically quantified by correlating the regional BOLD intensity timeseries'. It has been shown that the degree of functional connectivity between regions correlates with more direct neuronal measures of communication (Lee et al., 2010), relates to the degree of structural connectivity between the regions (Honey et al., 2009), and is predictive of variations in behavior (Hampson et al., 2006). The two main divisions in functional connectivity experimentation are resting state and task-based fMRI. Resting state fMRI is as simple as it sounds: a subject sits passively in the scanner while a BOLD scan sequence runs. The subject is typically instructed to rest passively but remain awake, either with eyes closed or open and fixating on a target. The researcher analyzes these data by selecting a seed region of interest, obtaining the mean regional timeseries, and searching for other regions whose timeseries' significantly correlate. Alternatively, data-driven methods like Independent Component Analysis (ICA) detect spatial sets of regions that are maximally correlated with each other and maximally independent of the remaining regions in the brain. These different methods have converged on the finding that there are distinct networks within the brain that are spatially distributed, intrinsically active, and statistically semi-independent (anti-correlated in some cases). The most well characterized network is the default mode network, a set of brain regions whose activity tends to increase when an individual is internally focused and decrease when the subject orients attention externally. This network, originally described by Greicius and colleagues (Greicius et al., 2003), has many semi-overlapping formulations but is generally agreed to include the retrosplenial

cortex/posterior cingulate, medial prefrontal cortex, and angular gyrus. A number of other coherent functional networks have subsequently discovered including the executive (Corbetta and Shulman, 2002), salience (Seeley et al., 2007), motor (Power et al., 2011), and vision subnetworks. One remarkable finding regarding these networks is there is a high spatial correspondence between these networks at rest with and during active task performance, suggesting that even the resting brain is highly "active" (Smith et al., 2009).

Another application of seed-based resting state fMRI is to obtain the functional connectivity matrix, analogous to the structural connectivity matrix described above. To obtain a functional connectivity matrix, a set of brain regions are registered to an individual's BOLD scan to obtain a regional mean timeseries. The statistical correlation coefficients between all pairs of regional timeseries' are stored in a matrix that describes the connection "strength" between any two regions. Graph theory methods are applied to assess these functional networks for global integration, local modularity, to assess which nodes in the network serve as communication hubs. Analysis of such networks has revealed the same characteristic balance of global and local connectivity, the so-called small worldness (Achard and Bullmore, 2007). These networks have proven sensitive in detecting developmental trajectories that reshape the pattern of functional connectivity (Dosenbach et al., 2010) and clinical abnormalities such as reduced modularity in schizophrenia patients (Alexander-Bloch et al., 2010).

Task-based functional connectivity methods have been developed to assess changes in connectivity patterns that occur when an individual performs a specific behavior. While correlations in regional activity do suggest communication, more sophisticated approaches are required to infer causal interactions and/or condition-specific modulations. Friston and colleagues have been responsible for the development of many of these techniques, among them Psychphysiological Interactions (PPI) (Friston et al., 1997). PPI is a method for detecting interactions between regions that are greater during one phase of a task than another. Specifically it looks for regional interactions over and above their co-activation to the task. This

method detects task-specific modulations of regional interaction, though the directionality of this connection cannot be inferred. The analysis of directional causal interactions in fMRI data is termed effective connectivity. Structural Equation Modeling (SEM) is one such method for testing the network structure of functional activity among a set of regions (Büchel and Friston, 1997) (Stein et al., 2007). The experimenter hypothesizes a specific connectivity graph (including directional connections) and obtains a statistic that reports how well the data fit that graph. They next compare between subjects or conditions to infer differences in functional network structure. Individual differences in resting state functional connectivity networks are known to relate to differences in memory ability in normal adults (Wig et al., 2008). Furthermore, memory-related subnetworks involving the hippocampus demonstrate specific impairment during episodic memory retrieval in individuals with mild cognitive impairment (Bai et al., 2009), supporting the specificity of this technique for probing compromised memory systems.

APOE and Alzheimer's Disease

Among individuals aged 60 and above, the likelihood of developing late-onset (non-familial) Alzheimer's Disease (AD) starts at 1% and increases two-fold every five years. Though progression of the disease is sporadic, the most typical cognitive symptoms are episodic memory deficits, language disturbances, and visuospatial problems. The current set of criteria developed by the NINCDS-ADRDA classify subjects in definite (clinical diagnosis and histological confirmation), probable (typical clinical syndrome with histological confirmation), or possible (atypical clinical symptoms with no alternative diagnoses).

While old age is the primary risk factor for developing AD, the disease also has known genetic risk factors, the primary one being the apolipoprotein E (APOE) epsilon 4 allele. 15-20% of the population carries at least one e4 allele. Individuals in this group are three to four times more likely to develop AD and have a younger mean age of onset than do carriers of the e3 allele (Corder et al., 1993).

The *apoe* protein mobilizes and transports cholesterol and lipids, vital materials for the synthesis of new cell membranes and the repair of existing cell membranes in the brain. apoe has also recently been shown to catalyze the degradation of amyloid-beta (Aβ) fragments (Jiang et al., 2008). The ε2, e3, and e4 variants of APOE have progressively decreased efficiency for both cholesterol transport and Aβ clearance (Mann et al., 2004). Myelin has the highest cholesterolconcentration of any tissue in the central nervous system, making it particularly sensitive to different APOE isoforms. Structural and functional studies of e4 carriers and non-carriers have revealed numerous brain differences across the lifespan (Bookheimer and Burggren, 2009). e4 carriers have also been shown to exhibit earlier signs of cognitive decline with aging (Caselli et al., 2004). Convergent evidence suggests that age-related brain changes in e4 carriers precede any associated cognitive decline (Caselli et al., 2004). Because older, cognitively normal e4 carriers possess an interaction of the two main AD risk factors, they are a critical target for identifying neuroimaging biomarkers of AD risk.

Structural Alterations in APOE/AD

Alzheimer disease is characterized by the accumulation of Aβ plaques and neurofibrillary tangles distributed throughout both gray and white matter in the brain. These changes begin in a silent preclinical phase that can last for decades before cognitive symptoms appear (Johnson et al., 2007). The MTL is typically the first region to exhibit cortical atrophy. Within the MTL, the entorhinal cortex appears to significantly thin before other subregions of hippocampal area have been affected in cognitively normal e4 carriers (Burggren et al., 2008; Reiman et al., 1998). Though the cause of this thinning remains unclear, there is evidence that reduced myelination of entorhinal afferents may results in cortical isolation and eventual atrophy (Salat et al., 2010). These efferent fibers are among the late-myelinating brain regions that have been demonstrated to exhibit early AD sensitivity. Association cortices begin myelinating later in lifespan than do sensory/motor core regions and have significantly less dense myelination (Braak and Braak,

1996). Oligodendrocytes in late-myelinating regions have a slower turnover rate and less capacity for myelin repair. The MTL, orbitomedial prefrontal cortex, and posterior cingulate have all been shown to exhibit increased white matter degradation in subjects at-risk for AD vs. normally aging adults (Bartzokis et al., 2007a). Additionally, e4 carriers have an accelerated rate of white matter degradation in late-myelinating regions of the brain, including the frontal lobe (Bartzokis et al., 2006). Bartzokis and colleagues employed an internet analogy to describe how white matter serves to increase axonal "bandwidth", citing that myelination increasing action potential speed 10-fold and decreasing the refractory period 34-fold (Bartzokis et al., 2008).

Functional Disruptions in APOE/AD

Task-based fMRI studies of e3 and e4 carriers have produced mixed results (Trachtenberg et al., 2010). Older, cognitively normal e4 carriers have shown increased fMRI activation during verbal episodic encoding and retrieval (Bookheimer et al., 2000) (Bondi et al., 2005) (Han et al., 2007), though this finding has not been strictly reproduced (Filippini et al., 2011). The subjects in Bookheimer et al.'s study performed a verbal episodic memory task (the same task used in this proposal) and demonstrated increased activation in the left hippocampal area, left prefrontal cortex, inferior and superior parietal lobes and anterior cingulate gyrus in e4 carriers vs. non-carriers. They found that initial increases in activation were reduced two years later. Specifically, decreases in mean percent signal change in the left hippocampal area correlated with decreased composite memory scores based on a complete neuropsychological battery (Braskie et al., 2009). These results align with the compensation hypothesis, which proposes that these pre-symptomatic increases in net activation may be a compensatory effect whereby additional cortical areas are recruited in order to augment the reduced processing capacity of affected networks (Han and Bondi, 2008). We hypothesize that disconnectivity between canonical episodic memory regions may initiate the process of compensation and ultimately result in decreased performance.

The majority of rs-fMRI studies in subjects with genetic risk for AD have focused on the default mode network (DMN). Filippini and colleagues found that young APOE e4 carriers (mean age=25) had higher default mode network coherence during rs-fMRI (Filippini et al., 2009). Fleisher and colleagues found that in older subjects, at-risk subjects (e4 carriers with a family history of AD) had stronger correlation between a seed in the posterior cingulate and several other nodes in the DMN (Fleisher et al., 2009). Sheline and colleagues focused on healthy e4 carriers without significant Ab deposition and reported altered patterns of resting-state functional connectivity with precuneus (Sheline et al., 2010a), finding both increases and decreases. In Chapter 3, we perform both task-based and pseudo-resting state analyses with the subjects in this study and systematically compare our results with these previous studies.

Global Network Disruptions in AD

A growing body of recent research suggests that disconnection is a major component of AD symptoms (Delbeuck et al., 2003). This makes AD and AD genetic risk particularly amenable to study with complex brain network analysis, a methodology for quantifying the brain's communication integration, efficiency, and robustness. Our DTI-based network analyses in healthy e4 carriers (Chapter 2) was the first such analysis. However, a recent network-based DTI tractography analysis of AD patients assessed characteristic path length, a measure of the average distance information must transfer between brain regions. In general, a shorter average distance for information to transfer is considered more efficient, given that there is a more metabolic and structural cost required to transmit information over a longer distance. In that study, AD patients had significantly higher characteristic path length than control individuals, indicating reduced global efficiency (Lo et al., 2010). He and colleagues examined structural networks in AD patients derived from cortical thickness regional correlations. They assessed the clustering, a measurement of how tightly interconnected regions are. They also quantified the ratio of clustering to path length, or "small worldness", a measure of the balance between local

and global integration. The AD patients had higher local clustering and longer global path length, indicative of an altered small-world architecture (He et al., 2008). Resting state fMRI studies of AD patients have consistently revealed network deficits including reduced functional activity in the default mode network (Greicius et al., 2004), a loss of small world properties in whole brain functional connectivity networks (Supekar et al., 2008), and reduced functional connectivity of distributed memory networks in the hippocampus and prefrontal cortex resulting in impaired global integration (Grady et al., 2001). Default mode network hubs in the posterior cingulate, precuneus and medial prefrontal cortex have also been shown to exhibit a striking overlap with the sites of greatest Aβ deposition in AD (Buckner et al., 2009). Patients with Mild Cognitive Impairment (MCI), a stage that often precedes Alzheimer's Disease, have also demonstrated connectivity deficits including reduced structural and functional integration of the hippocampus and posterior cingulate with the rest of the brain (Zhou et al., 2008). Resting state fMRI studies among older, cognitively normal individuals carrying the e4 allele have shown patterns of both higher and lower functional connectivity with respect to non-carriers. Thus, while specific alterations in structural and functional connectivity emerge in Alzheimer's Disease, it is clear that risk factors like the e4 allele impact connectivity differences long before disease symptoms manifest.

Data Sharing and Neuroinformatics

In addition to the rapid developments in hardware, software, and analysis methods that have taken place in neuroimaging, one additional advancement is noteworthy: the cultural shift towards broad data sharing (Milham, 2012). Broad efforts are now underway to collect and publicly share very large multimodal MRI datasets. Among these are the 1000 Functional Connectomes project for studying functional connectivity (Biswal et al., 2010), the Human Connectome Project for studying structural and functional brain connectivity (http://www.humanconnectome.org/), the Alzheimer's Neuroimaging Initiative (http://www.adni-

info.org/) for characterizing structural brain changes related to Alzheimer's Disease. In Chapter 5, we discuss the development of a website that serves as a repository and web-based analysis engine for connectivity matrices derived from structural and functional neuroimaging data. This tool allows for the access and rapid assessment of datasets of interest and contains data from individuals with multiple diseases/disorders including Alzheimer's Disease, Autism Spectrum Disorder, and Attention Deficit Hyperactivity Disorder. The connectivity matrices derived from all the studies in this dissertation have already been or will be publicly shared there in the future.

Chapter 1 References

Achard, S., Bullmore, E., 2007. Efficiency and Cost of Economical Brain Functional Networks. PLoS Comput Biol 3, e17.

Alexander-Bloch, A.F., Gogtay, N., Meunier, D., Birn, R., Clasen, L., Lalonde, F., Lenroot, R., Giedd, J., Bullmore, E.T., 2010. Disrupted Modularity and Local Connectivity of Brain Functional Networks in Childhood-Onset Schizophrenia. Front Syst Neurosci 4.

Bai, F., Zhang, Z., Watson, D.R., Yu, H., Shi, Y., Yuan, Y., Zang, Y., Zhu, C., Qian, Y., 2009. Abnormal functional connectivity of hippocampus during episodic memory retrieval processing network in amnestic mild cognitive impairment. Biol. Psychiatry 65, 951–958.

Bartzokis, G., Lu, P.H., Geschwind, D.H., Edwards, N., Mintz, J., Cummings, J.L., 2006. Apolipoprotein E genotype and age-related myelin breakdown in healthy individuals: implications for cognitive decline and dementia. Arch Gen Psychiatry 63, 63–72.

Bartzokis, G., Lu, P.H., Geschwind, D.H., Tingus, K., Huang, D., Mendez, M.F., Edwards, N., Mintz, J., 2007. Apolipoprotein E affects both myelin breakdown and cognition: implications for age-related trajectories of decline into dementia. Biol. Psychiatry 62, 1380–1387.

Bartzokis, G., Lu, P.H., Tingus, K., Mendez, M.F., Richard, A., Peters, D.G., Oluwadara, B., Barrall, K.A., Finn, J.P., Villablanca, P., Thompson, P.M., Mintz, J., 2008. Lifespan trajectory of myelin integrity and maximum motor speed. Neurobiol Aging.

Bassett, D.S., Bullmore, E.T., Meyer-Lindenberg, A., Apud, J.A., Weinberger, D.R., Coppola, R., 2009. Cognitive fitness of cost-efficient brain functional networks. Proceedings of the National Academy of Sciences 106, 11747–11752.

Bassett, D.S., Greenfield, D.L., Meyer-Lindenberg, A., Weinberger, D.R., Moore, S.W., Bullmore, E.T., 2010. Efficient physical embedding of topologically complex information processing networks in brains and computer circuits. PLoS Comput. Biol 6, e1000748.

Biswal, B.B., Mennes, M., Zuo, X.-N., Gohel, S., Kelly, C., et al., 2010. Toward discovery science of human brain function. Proc. Natl. Acad. Sci. U.S.A. 107, 4734–4739.

Bondi, M.W., Houston, W.S., Eyler, L.T., Brown, G.G., 2005. fMRI evidence of compensatory mechanisms in older adults at genetic risk for Alzheimer disease. Neurology 64, 501–508.

Bookheimer, S., Burggren, A., 2009. APOE-4 Genotype and Neurophysiological Vulnerability to Alzheimer's and Cognitive Aging. Annu. Rev. Clin. Psychol. 5, 343–362.

Bookheimer, S.Y., Strojwas, M.H., Cohen, M.S., Saunders, A.M., Pericak-Vance, M.A., Mazziotta, J.C., Small, G.W., 2000. Patterns of Brain Activation in People at Risk for Alzheimer's Disease. N Engl J Med 343, 450–456.

Braak, H., Braak, E., 1991. Neuropathological stageing of Alzheimer-related changes. Acta Neuropathol. 82, 239–259.

Braak, H., Braak, E., 1996. Development of Alzheimer-related neurofibrillary changes in the neocortex inversely recapitulates cortical myelogenesis. Acta Neuropathol 92, 197–201.

Braskie, M.N., Small, G.W., Bookheimer, S.Y., 2009. Entorhinal cortex structure and functional MRI response during an associative verbal memory task. Hum Brain Mapp 30, 3981–3992.

Büchel, C., Friston, K.J., 1997. Modulation of connectivity in visual pathways by attention: cortical interactions evaluated with structural equation modelling and fMRI. Cerebral Cortex 7, 768 –778.

Buckner, R.L., Sepulcre, J., Talukdar, T., Krienen, F.M., Liu, H., Hedden, T., Andrews-Hanna, J.R., Sperling, R.A., Johnson, K.A., 2009. Cortical Hubs Revealed by Intrinsic Functional Connectivity: Mapping, Assessment of Stability, and Relation to Alzheimer's Disease. J. Neurosci. 29, 1860–1873.

Bullmore, E., Sporns, O., 2009. Complex brain networks: graph theoretical analysis of structural and functional systems. Nat Rev Neurosci 10, 186–98.
Burggren, A.C., Zeineh, M.M., Ekstrom, A.D., Braskie, M.N., Thompson, P.M., Small, G.W., Bookheimer, S.Y., 2008. Reduced cortical thickness in hippocampal subregions among cognitively normal apolipoprotein E e4 carriers. Neuroimage 41, 1177–83.
Caselli, R.J., Reiman, E.M., Osborne, D., Hentz, J.G., Baxter, L.C., Hernandez, J.L., Alexander, G.G., 2004. Longitudinal changes in cognition and behavior in asymptomatic carriers of the APOE e4 allele. Neurology 62, 1990–1995.
Charlton, R.A., Barrick, T.R., Markus, H.S., Morris, R.G., 2010. The relationship between episodic long-term memory and white matter integrity in normal aging. Neuropsychologia 48, 114–122.
Corbetta, M., Shulman, G.L., 2002. Control of goal-directed and stimulus-driven attention in the brain. Nat. Rev. Neurosci. 3, 201–215.
Corder, E.H., Saunders, A.M., Strittmatter, W.J., Schmechel, D.E., Gaskell, P.C., Small, G.W., Roses, A.D., Haines, J.L., Pericak-Vance, M.A., 1993. Gene dose of apolipoprotein E type 4 allele and the risk of Alzheimer's disease in late onset families. Science 261, 921–3.
De Calignon, A., Polydoro, M., Suárez-Calvet, M., William, C., Adamowicz, D.H., Kopeikina, K.J., Pitstick, R., Sahara, N., Ashe, K.H., Carlson, G.A., Spires-Jones, T.L., Hyman, B.T., 2012. Propagation of Tau Pathology in a Model of Early Alzheimer's Disease. Neuron 73, 685–697.
Delbeuck, X., Van der Linden, M., Collette, F., 2003. Alzheimer's disease as a disconnection syndrome? Neuropsychol Rev 13, 79–92.
Dosenbach, N.U.F., Nardos, B., Cohen, A.L., Fair, D.A., Power, J.D., Church, J.A., Nelson, S.M., Wig, G.S., Vogel, A.C., Lessov-Schlaggar, C.N., Barnes, K.A., Dubis, J.W., Feczko, E., Coalson, R.S., Pruett, J.R., Barch, D.M., Petersen, S.E., Schlaggar, B.L., 2010. Prediction of Individual Brain Maturity Using fMRI. Science 329, 1358 –1361.
Felleman, D.J., Van Essen, D.C., 1991. Distributed hierarchical processing in the primate cerebral cortex. Cereb. Cortex 1, 1–47.
Filippini, N., Ebmeier, K.P., Macintosh, B.J., Trachtenberg, A.J., Frisoni, G.B., Wilcock, G.K., Beckmann, C.F., Smith, S.M., Matthews, P.M., Mackay, C.E., 2011. Differential effects of the APOE genotype on brain function across the lifespan. Neuroimage 54, 602–610.
Filippini, N., MacIntosh, B.J., Hough, M.G., Goodwin, G.M., Frisoni, G.B., Smith, S.M., Matthews, P.M., Beckmann, C.F., Mackay, C.E., 2009. Distinct patterns of brain activity in young carriers of the APOE-ε4 allele. Proceedings of the National Academy of Sciences 106, 7209 –7214.
Fischl, B., Dale, A.M., 2000. Measuring the thickness of the human cerebral cortex from magnetic resonance images. Proc. Natl. Acad. Sci. U.S.A 97, 11050–11055.
Fleisher, A.S., Sherzai, A., Taylor, C., Langbaum, J.B.S., Chen, K., Buxton, R.B., 2009. Resting-state BOLD networks versus task-associated functional MRI for distinguishing Alzheimer's disease risk groups. NeuroImage 47, 1678–1690.
Friston, K.J., Buechel, C., Fink, G.R., Morris, J., Rolls, E., Dolan, R.J., 1997. Psychophysiological and modulatory interactions in neuroimaging. Neuroimage 6, 218–29.
Gómez-Isla, T., Price, J.L., McKeel, D.W., Jr, Morris, J.C., Growdon, J.H., Hyman, B.T., 1996. Profound loss of layer II entorhinal cortex neurons occurs in very mild Alzheimer's disease. J. Neurosci. 16, 4491–4500.
Grady, C.L., Furey, M.L., Pietrini, P., Horwitz, B., Rapoport, S.I., 2001. Altered brain functional connectivity and impaired short-term memory in Alzheimer's disease. Brain 124, 739–56.

Greicius, M.D., Krasnow, B., Reiss, A.L., Menon, V., 2003. Functional connectivity in the resting brain: A network analysis of the default mode hypothesis. Proceedings of the National Academy of Sciences of the United States of America 100, 253 –258.
Greicius, M.D., Srivastava, G., Reiss, A.L., Menon, V., 2004. Default-mode network activity distinguishes Alzheimer's disease from healthy aging: Evidence from functional MRI. Proceedings of the National Academy of Sciences of the United States of America 101, 4637–4642.
Hagmann, P., Cammoun, L., Gigandet, X., Meuli, R., Honey, C.J., Wedeen, V.J., Sporns, O., 2008. Mapping the Structural Core of Human Cerebral Cortex. PLoS Biology 6, e159 EP –.
Hampson, M., Driesen, N.R., Skudlarski, P., Gore, J.C., Constable, R.T., 2006. Brain Connectivity Related to Working Memory Performance. The Journal of Neuroscience 26, 13338 –13343.
Han, S.D., Bondi, M.W., 2008. Revision of the apolipoprotein E compensatory mechanism recruitment hypothesis. Alzheimer's and Dementia 4, 251–254.
Han, S.D., Drake, A.I., Cessante, L.M., Jak, A.J., Houston, W.S., Delis, D.C., Filoteo, J.V., Bondi, M.W., 2007. Apolipoprotein E and traumatic brain injury in a military population: evidence of a neuropsychological compensatory mechanism? Journal of Neurology, Neurosurgery & Psychiatry 78, 1103 –1108.
He, Y., Chen, Z., Evans, A., 2008. Structural Insights into Aberrant Topological Patterns of Large-Scale Cortical Networks in Alzheimer's Disease. J. Neurosci. 28, 4756–4766.
Honey, C.J., Sporns, O., Cammoun, L., Gigandet, X., Thiran, J.P., Meuli, R., Hagmann, P., 2009. Predicting human resting-state functional connectivity from structural connectivity. Proceedings of the National Academy of Sciences 106, 2035–2040.
Iturria-Medina, Y., Sotero, R.C., Canales-Rodríguez, E.J., Alemán-Gómez, Y., Melie-García, L., 2008. Studying the human brain anatomical network via diffusion-weighted MRI and Graph Theory. NeuroImage 40, 1064–1076.
Jiang, Q., Lee, C.Y.D., Mandrekar, S., Wilkinson, B., Cramer, P., Zelcer, N., Mann, K., Lamb, B., Willson, T.M., Collins, J.L., Richardson, J.C., Smith, J.D., Comery, T.A., Riddell, D., Holtzman, D.M., Tontonoz, P., Landreth, G.E., 2008. ApoE Promotes the Proteolytic Degradation of A[beta]. Neuron 58, 681–693.
Johnson, S.C., Ries, M.L., Hess, T.M., Carlsson, C.M., Gleason, C.E., Alexander, A.L., Rowley, H.A., Asthana, S., Sager, M.A., 2007. Effect of Alzheimer Disease Risk on Brain Function During Self-Appraisal in Healthy Middle-Aged Adults. Arch Gen Psychiatry. 64, 1163–1171.
Lee, J.H., Durand, R., Gradinaru, V., Zhang, F., Goshen, I., Kim, D.-S., Fenno, L.E., Ramakrishnan, C., Deisseroth, K., 2010. Global and local fMRI signals driven by neurons defined optogenetically by type and wiring. Nature 465, 788–792.
Lo, C.-Y., Wang, P.-N., Chou, K.-H., Wang, J., He, Y., Lin, C.-P., 2010. Diffusion Tensor Tractography Reveals Abnormal Topological Organization in Structural Cortical Networks in Alzheimer's Disease. J. Neurosci. 30, 16876–16885.
Mann, K.M., Thorngate, F.E., Katoh-Fukui, Y., Hamanaka, H., Williams, D.L., Fujita, S., Lamb, B.T., 2004. Independent effects of APOE on cholesterol metabolism and brain A{beta} levels in an Alzheimer disease mouse model. Hum. Mol. Genet. 13, 1959–1968.
Milham, M.P., 2012. Open Neuroscience Solutions for the Connectome-wide Association Era. Neuron 73, 214–218.
Power, J.D., Cohen, A.L., Nelson, S.M., Wig, G.S., Barnes, K.A., Church, J.A., Vogel, A.C., Laumann, T.O., Miezin, F.M., Schlaggar, B.L., Petersen, S.E., 2011. Functional Network Organization of the Human Brain. Neuron 72, 665–678.
Raj, A., Kuceyeski, A., Weiner, M., 2012. A Network Diffusion Model of Disease Progression in Dementia. Neuron 73, 1204–1215.

Reiman, E.M., Uecker, A., Caselli, R.J., Lewis, S., Bandy, D., De Leon, M.J., De Santi, S., Convit, A., Osborne, D., Weaver, A., Thibodeau, S.N., 1998. Hippocampal volumes in cognitively normal persons at genetic risk for Alzheimer's disease. Ann Neurol 44, 288–91.

Salat, D.H., Tuch, D.S., Van der Kouwe, A.J.W., Greve, D.N., Pappu, V., Lee, S.Y., Hevelone, N.D., Zaleta, A.K., Growdon, J.H., Corkin, S., Fischl, B., Rosas, H.D., 2010. White matter pathology isolates the hippocampal formation in Alzheimer's disease. Neurobiol. Aging 31, 244–256.

Seeley, W.W., Menon, V., Schatzberg, A.F., Keller, J., Glover, G.H., Kenna, H., Reiss, A.L., Greicius, M.D., 2007. Dissociable intrinsic connectivity networks for salience processing and executive control. J. Neurosci 27, 2349–2356.

Sheline, Y.I., Morris, J.C., Snyder, A.Z., Price, J.L., Yan, Z., D'Angelo, G., Liu, C., Dixit, S., Benzinger, T., Fagan, A., Goate, A., Mintun, M.A., 2010. APOE4 Allele Disrupts Resting State fMRI Connectivity in the Absence of Amyloid Plaques or Decreased CSF A{beta}42. J. Neurosci. 30, 17035–17040.

Smith, S.M., Fox, P.T., Miller, K.L., Glahn, D.C., Fox, P.M., Mackay, C.E., Filippini, N., Watkins, K.E., Toro, R., Laird, A.R., Beckmann, C.F., 2009. Correspondence of the brain's functional architecture during activation and rest. Proceedings of the National Academy of Sciences 106, 13040 –13045.

Sporns, O., 2010. Networks of the Brain, 1st ed. The MIT Press.

Squire, L.R., Stark, C.E.L., Clark, R.E., 2004. The Medial Temporal Lobe*. Annual Review of Neuroscience 27, 279–306.

Stein, J.L., Wiedholz, L.M., Bassett, D.S., Weinberger, D.R., Zink, C.F., Mattay, V.S., Meyer-Lindenberg, A., 2007. A validated network of effective amygdala connectivity. NeuroImage 36, 736–745.

Supekar, K., Menon, V., Rubin, D., Musen, M., Greicius, M.D., 2008. Network analysis of intrinsic functional brain connectivity in Alzheimer's disease. PLoS Comput. Biol 4, e1000100.

Trachtenberg, A.J., Filippini, N., Mackay, C.E., 2010. The effects of APOE-epsilon4 on the BOLD response. Neurobiol Aging.

Wig, G.S., Grafton, S.T., Demos, K.E., Wolford, G.L., Petersen, S.E., Kelley, W.M., 2008. Medial temporal lobe BOLD activity at rest predicts individual differences in memory ability in healthy young adults. Proceedings of the National Academy of Sciences 105, 18555 –18560.

Zhou, Y., Dougherty Jr, J.H., Hubner, K.F., Bai, B., Cannon, R.L., Hutson, R.K., 2008. Abnormal connectivity in the posterior cingulate and hippocampus in early Alzheimer's disease and mild cognitive impairment. Alzheimer's and Dementia 4, 265–270.

Chapter 2

Brain Network Local Interconnectivity Loss in Aging APOE-4 Carriers[1]

Jesse A. Brown, Kevin H. Terashima, Alison C. Burggren, Linda M. Ercoli, Karen J. Miller, Gary W. Small and Susan Y. Bookheimer

Abstract

Old age and possession of the APOE-4 allele are the two main risk factors for developing later onset Alzheimer's disease (AD). Carriers of the APOE-4 allele have known differences in intrinsic functional brain network activity across the lifespan. These individuals also demonstrate specific regional differences in gray and white matter gross structure. However, the relationship of these variations to whole brain structural network connectivity remains unclear. We performed diffusion tensor imaging (DTI), T1 structural imaging, and cognitive testing on aging APOE-4 non-carriers (n=30; mean age=63.8+/-8.3) and APOE-4 carriers (n=25; mean age=60.8+/-9.7). Fiber tractography was used to derive whole brain structural graphs and graph theory was applied to assess structural network properties. Network communication efficiency was determined for each network by quantifying local interconnectivity, global integration, and the balance between these – the small worldness. Relative to non-carriers, APOE-4 carriers demonstrated an accelerated age-related loss of mean local interconnectivity (r=-.64, p=<.01) and regional local interconnectivity declines in the precuneus (r=-.69), medial orbitofrontal cortex (r=-.6), and lateral parietal cortex (r=-.62). APOE-4 carriers also showed significant age-related loss in mean cortical thickness (r=-.44, p<.05). Cognitively, APOE-4 carriers had significant negative correlations of age and performance on two episodic memory tasks (p<.05). This genotype-specific pattern of structural connectivity change with age thus appears related to changes in gross cortical structure (i.e. cortical thickness) and cognition, potentially affecting the rate and/or spatial distribution of AD-related

[1] *Proc Natl Acad Sci*. Dec 20, 2011 ; 108(51):20760-5.

[2] *Frontiers in Neuroinformatics*. 28 November 2012. doi: 10.3389/fninf.2012.00028

pathology.

Introduction

Although increasing age is the primary risk factor for developing Alzheimer's disease (AD), the disease also has known genetic risk factors. The sole confirmed genetic variant is the apolipoprotein E epsilon 4 allele (*APOE*-4) (Naj et al., 2011) of which 15-20% of the Caucasian population carries at least one copy. Individuals in this group are three to four times more likely to develop AD and have a younger mean age at onset than APOE-4 non-carriers (Corder et al., 1993). The APOE protein functions as the principal cholesterol transporter in the brain and affects diverse cellular processes including development, plasticity, and repair in both gray and white matter (Mahley, 1988). Neuroimaging studies of APOE-4 carriers and APOE-4 non-carriers (APOE-4 NCs) have revealed numerous structural and functional brain differences across the lifespan (Bookheimer and Burggren, 2009). While APOE-4 carriers have been shown to exhibit earlier signs of cognitive decline with aging (Caselli et al., 2004), some genotype-specific brain differences appear before cognitive decline (Reiman et al., 2005) (Small et al., 2000) (Small et al., 2009) (Bookheimer et al., 2000). APOE-4 carriers aged 60 and above are at elevated risk for developing AD (Corder et al., 1993) and are thus a critical target for identifying neuroimaging biomarkers of AD risk that accompany cognitive decline associated with disease risk.

Neuronal atrophy is known to follow a characteristic trajectory in AD, originating in temporal, parietal, and limbic cortices and eventually spreading to frontal regions (Thompson et al., 2003). A growing body of recent research has demonstrated that disconnection between regions is a major component of AD, resulting in specific cognitive deficits such as episodic memory loss (Delbeuck et al., 2003). White matter degradation is concomitant with gray matter loss in AD, typically originating in regions which undergo myelination late in development (Stricker et al., 2009) (Salat et al., 2010). This loss of axonal myelination reduces the fidelity of communication

between brain regions (Bartzokis et al., 2007b), adversely affecting neuronal synchrony (Stam et al., 2007). This makes AD and AD genetic risk particularly amenable to study with complex brain network analysis, a methodology for quantifying the brain's communication integration, efficiency, and robustness (Rubinov and Sporns, 2010).

Diffusion Tensor Imaging (DTI) tractography quantifies the density of white matter-insulated axonal bundles that connect different regions of the brain. It is a primary method for characterizing the brain's white matter or "structural" network (Hagmann et al., 2008). Structural brain networks inferred from DTI tractography can be reduced to connectivity matrices or "graphs" that describe the strength of connection between any pair of brain regions. These matrices are typically analyzed using graph theory, a branch of mathematics with methods to formally analyze a pattern of connections ("edges") between different entities ("nodes"). Specific regional and global metrics measure the local and global efficiency of information processing by quantifying the density of connections between regions and the distance over which information must transfer. This analysis technique has been increasingly employed in neuroimaging studies to characterize both structural and functional brain networks (Bullmore and Sporns, 2009). Network-based measures of structural and functional brain connectivity can be more sensitive to alterations that are not apparent in gross structure (e.g. cortical thickness or white matter integrity) because they consider each region's integration into the global unit rather than as an independent entity. Convergent evidence from these studies (Iturria-Medina et al., 2008) (Achard and Bullmore, 2007) indicates that brain networks exhibit small worldness, a balance of two properties: high local clustering, a dense interconnectivity among physically adjacent regions, and high global efficiency, a relatively short distance information must travel between any two nodes in the network.

Several independent lines of evidence implicate reduced network connectivity in AD. A recent network-based DTI tractography analysis of AD patients by Lo and colleagues (Lo et al., 2010) assessed characteristic path length, a measure of the average distance information must

transfer between brain regions. In general, a network in which there is a shorter average distance for information to transfer is considered more efficient, given that there is a more metabolic and structural cost required to transmit information over a longer distance. Lo et al. found that AD patients had significantly higher characteristic path length than control individuals, indicating reduced global efficiency. Resting state fMRI connectivity studies of AD patients have also consistently revealed network deficits. Reduced functional connectivity in the brain's default mode network (DMN) is a hallmark of AD (Greicius et al., 2004). This network is comprised of the posterior cingulate, medial prefrontal cortex, lateral inferior parietal cortex, lateral inferior temporal cortex, anterior cingulate, medial temporal lobe, and precuneus (Margulies et al., 2009) (Mevel et al., 2011). The DMN is highly metabolically active, particularly when an individual has internally focused attention, such as during episodic memory retrieval (Raichle et al., 2001) (Kim et al., 2010). Importantly, DMN hubs in the posterior cingulate, precuneus and medial prefrontal cortex have also been shown to exhibit a striking overlap with the sites of greatest Aβ deposition in AD (Buckner et al., 2009). A resting state fMRI study in AD patients investigating whole brain functional connectivity networks revealed a loss of both local and global integration (Supekar et al., 2008). Patients with Mild Cognitive Impairment (MCI), a stage that often precedes Alzheimer's Disease, have also demonstrated connectivity deficits including reduced structural and functional integration of the hippocampus and posterior cingulate with the rest of the brain (Zhou et al., 2008).

In cognitively normal APOE-4 carriers, structural brain connectivity has primarily been assessed looking at gross measures of white matter integrity such as fractional anisotropy (FA) and apparent diffusion coefficient (ADC). In older APOE-4 carriers, age-related decreases in myelination (Bartzokis et al., 2006) and FA (Ryan et al., 2011) have been observed that are more rapid than non-carriers, particularly in the frontal and temporal lobes. There is substantial evidence that older APOE-4 carriers perform worse than non-carriers on episodic memory tests (Tuminello and Han, 2011). Regardless of the mechanism, it is clear that AD risk factors like the

APOE-4 allele impact brain structural and functional differences long before AD symptoms manifest.

Here we used diffusion tensor imaging (DTI) and a hybrid probabilistic/deterministic tractography approach to characterize fiber network topology in aging, cognitively normal subjects with genetic risk for AD. We analyzed the fiber networks of APOE-4 non-carriers and APOE-4 carriers for path length, clustering, and small worldness in order to assess local and global variations in network topology that may be associated with cognitive decline and precede the conversion AD.

Results

Cognitive Performance

Cognitive scores on all neuropsychological tests were compared for APOE-4 carriers and non-carriers using two-sample two-tailed t-tests (**Table 1**). No significant between-group differences were found with the exception of the Mini-Mental State Exam (MMSE). However, when MMSE was included as a covariate in subsequent statistical analyses it did not affect any statistical results. Relationships between age and cognitive performance were tested in two ways. First, within genotype group, partial correlations were calculated between age and each neuropsychological measure, controlling for gender, years of education, and family history of dementia. Second, a stepwise regression was run, starting with a model of APOE status (carrier or non-carrier), gender, age, APOE x age interaction, years of education, and family history of dementia (yes or no). APOE-4 carriers exhibited significant age-related cognitive declines on the Wechsler memory scale, logical memory delayed recall portion (Delay Total LM; partial r=-.44, p=.038) and Rey Osterrith Complex Figure, delayed recall (Delay ROF; partial r=-.57, p=.005) (**Figure S1**). APOE-4 non-carriers had no significant age-related declines on these tests. The stepwise regression found the APOE x age interaction to be significant for both the Delay Total LM (p=.015) and Delay ROF (p=.001) tests.

Characteristic (mean±SD)	APOE-4 NC	APOE-4	P	APOE-4 NC Partial Correlation with Age	APOE-4 Partial Correlation with Age
Age (years)	63.8 +/- 8.3	60.8 +/- 9.7	0.22		
Age range	45-76	43-78			
Number (Males/Females)	30 (10/20)	25 (12/13)			
Education (years)	16.7 +/- 1.8	17.5 +/- 3.3	0.33		
Family History (yes/no)	21/9	16/9			
MMSE (score range 0-30)	29.4 +/- .9	28.6 +/- 1.2	0.01*	r=-.41, p=.07	r=-.14, p=.55
WMS LM Delay (0-50)	29.1 +/- 7.1	27.1 +/- 9.2	0.45	r=-.09, p=.66	r=-.45, p=.038*
Buschke CLTR (0-144)	56.7 +/- 39.7	57.8 +/- 34.2	0.92	r=-.16, p=..44	r=-.36, p=.1
Rey-O Delay (0-36)	12.9 +/- 7.2	13.8 +/- 7.1	0.68	r=-.03, p=.87	r=-.57, p=.005*
WMS VP (0-32)	22.3 +/- 7.4	20.6 +/- 8.2	0.49	r=-.17, p=.38	r=.05, p=.8
WAIS Digit Span	17.7 +/- 3.6	18.1 +/- 3.1	0.65	r=.21, p=.29	r=.1, p=.65

Table 1: Subject characteristics. Partial correlations with age were controlled for gender, years of education, and family history of dementia. MMSE – Mini-Mental State Examination; WMS LM Delay – Wechsler memory scale, logical memory delayed recall portion; Buschke CLTR – Buschke-Fuld selective reminding test, consistent long-term retrieval section; Rey-O Delay – Rey Osterrith Complex Figure, delayed recall; WMS VP – Wechsler memory scale, verbal paired associations II; WAIS Digit Span – Wechsler Adult Intelligence Scale 3, digit span

Age Effects on Global Network Connectivity

Structural connectivity matrices were analyzed for each subject in order to determine global structural network measures of global integration (characteristic path length), local interconnectivity (mean clustering coefficient), the balance of integration and interconnectivity (small worldness), and the total amount of fiber constituting the network (total network cost). These metrics were then assessed for genotype specific age-related changes. The partial correlation was calculated between all structural network metrics and age, controlling for gender, scanner, and total network cost. This ensured that differences in clustering coefficient between APOE-4 and APOE-4 non-carriers were not driven by differences in the total amount of

axonal fibers between groups. The partial correlation of clustering coefficient and age was non-significant for APOE-4 non-carriers (r=-.33 p=.09) and strongly negative for APOE-4 carriers (r=-.63, p=.002) (**Figure 1A**). The stepwise regression model found that the APOE x age interaction was significant (p=.0005).

The partial correlation between characteristic path length and age trended towards significance for APOE-4 non-carriers (r=.36, p=.08) but was non-significant for APOE-4 carriers (r=.21, p=.37). The stepwise regression found no significant APOE x age interaction for characteristic path length.

To look at the combined effect of clustering coefficient and characteristic path length, small worldness (s) was assessed separately for the two groups. APOE-4 non-carriers showed a trend for a negative relationship between age and small worldness (r=-.26, p=.2) while APOE-4 carriers showed a strong negative correlation (r=-.52, p=.012). However, stepwise regression did not find a significant APOE x age interaction for small worldness.

Finally, measurements of total network cost were compared to age. The partial correlation of age and total cost was significantly negative for APOE-4 non-carriers (r=-.44, p=.02) but not for APOE-4 non-carriers (r=-.-.31, p=.18). However, stepwise regression did not find a significant APOE x age interaction.

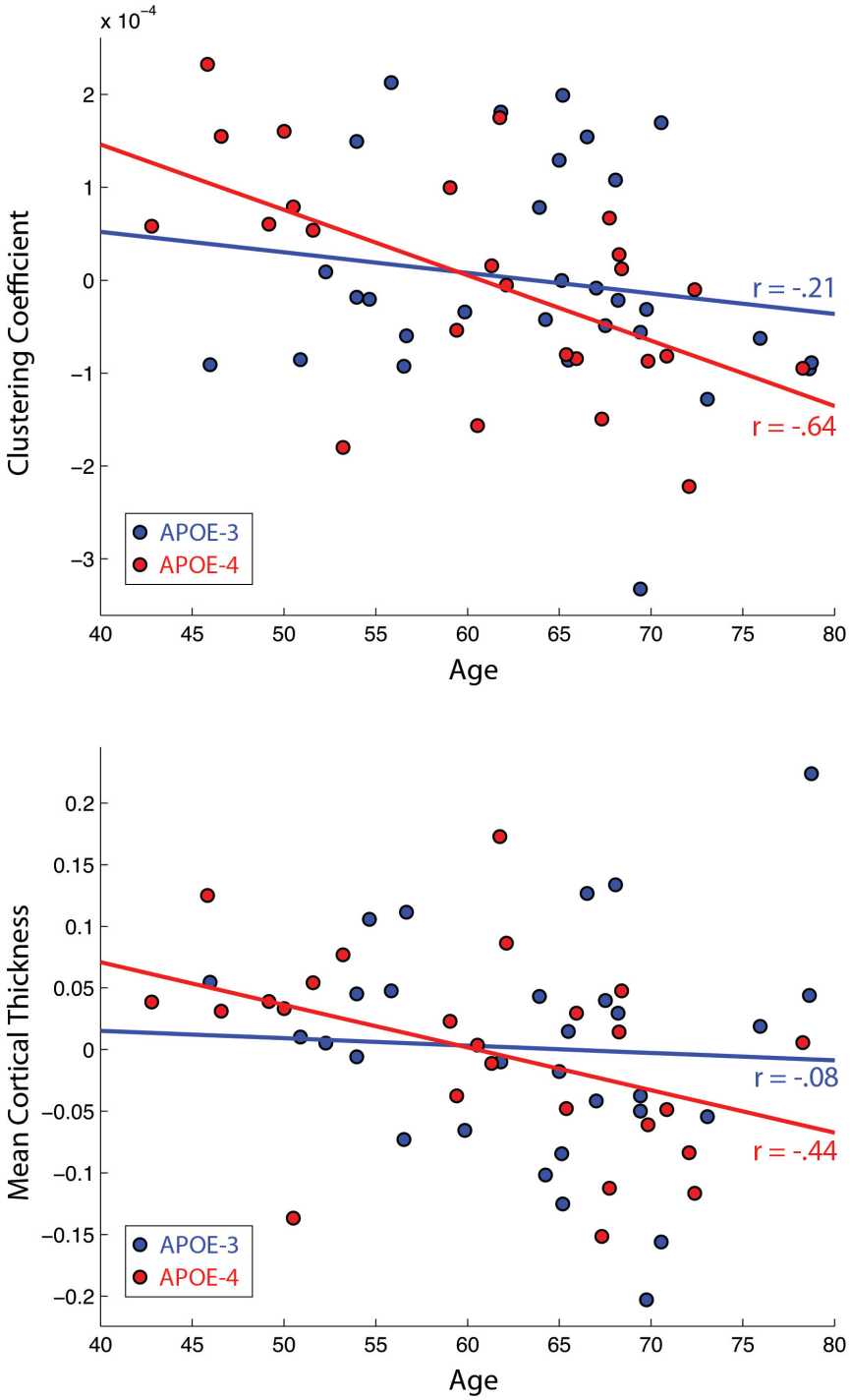

Figure 1: Mean clustering coefficient (MCC) and mean cortical thickness (MCT) residuals based on partial correlations with age plotted for APOE-4 noncarriers (APOE-3; blue) and APOE-4 carriers (red). Partial correlations controlled for gender, scanner, and in the MCC case only, total network cost. Both MCC and MCT had a significant interaction between APOE genotype ($p < .05$).

Age Effects on Regional Network Connectivity

We next examined whether the relationship between age and network characteristics varied by region for APOE-4 carriers and non-carriers. The analysis was focused on regional clustering coefficients because mean clustering coefficient showed a global APOE x age interaction effect. For the model to predict regional clustering coefficient, the set of terms which stepwise regression found to best fit the mean clustering coefficient were used. This model included APOE, gender, APOE x age interaction, total cost, and scanner. At a FDR-corrected alpha of p=.05, several regions showed a significant interaction where APOE-4 carriers decreased more sharply than non-carriers: the right precuneus (p=.00006), right cuneus (p=.00007), left orbitofrontal cortex (p=.004), left supramarginal gyrus (p=.002), and right inferior temporal gyrus anteriorly (p=.0009) and posteriorly (p=.002) **(Figure 2)**. At an exploratory threshold of p < .005 (uncorrected), additional regions displaying a potential APOE x age interaction included right subcallosal cortex (part of the ventromedial prefrontal cortex, p=.009), the, right middle temporal gyrus (p=.009), and right precentral gyrus (p=.009) **(Figure 2)**.

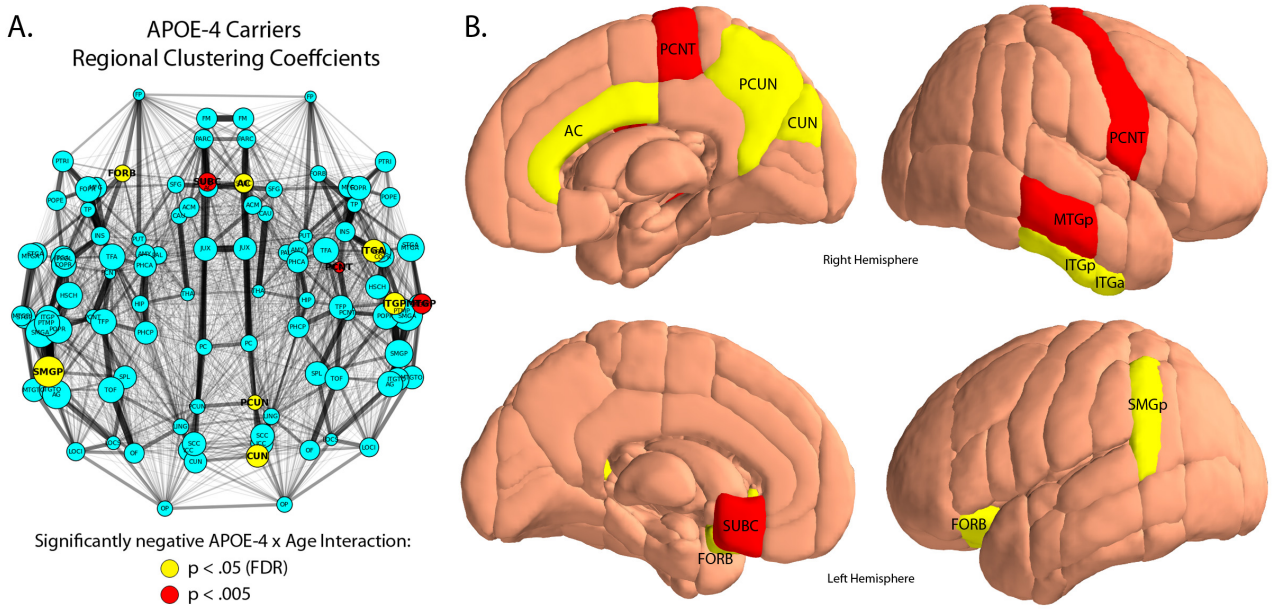

Figure 2
A) DTI average weighted network with node radius corresponding to value of negative correlation of age with clustering coefficient for APOE-4 carriers. The width of each edge in the graph corresponds to the average fiber density between those regions. Nodes colored in yellow have significant negative APOE-4 x Age interactions for clustering coefficient ($p < .05$, FDR-corrected), nodes colored in red indicate the same measure at an exploratory threshold ($p < .005$, uncorrected). **B)** The same nodes from A) displayed on an anatomical brain model. Node abbreviations: AC: anterior cingulate, PCNT: precentral gyrus, PCUN: precuneus, CUN: cuneus, ITGa: inferior temporal gyrus (anterior), ITGp: inferior temporal gyrus (posterior), MTGp: middle temporal gyrus (posterior), FORB: frontal orbital cortex, SUBC: subcallosal cortex (part of the ventromedial prefrontal cortex), SMGp: supramarginal gyrus (posterior).

Cortical Thickness

The mean cortical thickness values were also examined in relationship to age for APOE-4 carriers and non-carriers. APOE-4 carriers demonstrated a significant negative partial correlation between cortical thickness with age ($r=-.44$, $p=.02$) while non-carriers displayed no relationship ($r=-.08$, $p=.64$). Stepwise regression found a significant APOE x age interaction for cortical thickness ($p=.03$) (**Figure 1B**).

Finally, the relationships between APOE genotype, cortical thickness, and structural network metrics were assessed. We ran the same stepwise regression model used in our previous analyses but added terms for a main effect of cortical thickness and an APOE x cortical thickness interaction. For clustering coefficient, the APOE x cortical thickness term was significant ($p=.0001$). This interaction was not significant for characteristic path length or small worldness (both $p>.05$).

Discussion

This study of axonal fiber networks found that aging APOE-4 carriers showed a significantly more negative relationship between local interconnectivity and age while than non-carriers. APOE-4 carriers also exhibited a significant decrease in small worldness with age, though no significant interaction between APOE and age was detected. Neither APOE-4

carriers and non-carriers showed significant relationships between charateristic path length and age, indicating no major loss of global structural integration. Small worldness represents the balance of clustering coefficient (local interconnectivity) and characteristic path length (global integration) in a real network with respect to a random network. Here it appears that the APOE-4 carrier age-related decline in small worldness observed here was driven primarily by the loss of local interconnectivity while global integration was relatively spared.

APOE-4 carriers also showed significant cortical thinning with age. This decline paralleled the decrease in structural network local interconnectivity, suggesting a relationship between cortical thickness and the degree of local structural connectivity. Interestingly, there was a significant effect of APOE genotype x cortical thickness interaction on local interconnectivity: only APOE-4 carriers showed a significant relationship between cortical thickness and local interconnectivity. It is possible that the relationship between these two measures grows stronger as they decrease, which would help explain why only APOE-4 carriers showed this statistical association. Alternatively, the APOE-4 allele may contribute to a tighter relationship between these brain structural properties. The finding of cortical thinning with age in APOE-4 carriers is not without precedence, as a previous report (Espeseth et al., 2008) found that aging APOE-4 carriers have 1) higher cortical thickness when controlling for age and 2) a stronger age-related decrease in cortical thickness than non-carriers. However, it should be noted that in the current study the relationship of local interconnectivity and age was somewhat stronger than the decrease in cortical thickness, indicating some independence of these measures and the utility of both in detecting age-related changes that may precede the conversion to AD.

The age-related decline in local interconnectivity amongst APOE-4 carriers in this study appeared to be especially driven by the younger subjects, who had the highest measurements of clustering coefficient. The relationship between high structural local connectivity and brain health in general is not entirely clear. The first study of DTI structural network properties and

intelligence found a positive relationship between IQ and clustering coefficient (Li et al., 2009). The APOE-4 carriers in the present study had significant negative relationships of performance and age on two different episodic memory tasks, supporting the notion that decreasing interconnectivity has negative behavioral consequences. Importantly, previous evidence does suggest higher connectivity in young APOE-4 carriers. A study of resting state fMRI patterns found healthy APOE-4 carriers in young adulthood exhibited greater DMN connectivity than non-carriers (Filippini et al., 2009). Similar studies in older APOE-4 carriers have shown a complex pattern of increased and decreased functional connectivity with respect to non-carriers (Fleisher et al., 2009) (Sheline et al., 2010b). Thus, there appears to be a unique age-related trajectory of connectivity change over development for APOE-4 carriers. Specifically, there is an apparent higher degree of connectivity early in life that declines more steeply across the age span. Interestingly, a similar pattern appears to hold for cognitive abilities associated with APOE-4. Several cognitive studies in healthy APOE-4 carriers and non-carriers have found better cognitive performance for young APOE-4 carriers (Mondadori et al., 2007) (Han et al., 2007), a trend that reverses for APOE-4 carriers in their 50's with declines in memory occurring the earliest (Caselli et al., 2009). This developmental trajectory has hypothesized as a case of antagonistic pleiotropy, in which the APOE-4 allele offers benefits during development and early adulthood at the expense of more rapid decline with aging (Tuminello and Han, 2011). Alternatively, local connectivity has been shown to reduce during development in the years when pruning is the dominant structural process (Hagmann et al., 2010) (Luo and O'Leary, 2005), which may indicate that APOE-4 carriers undergo less pruning. Regardless of the potential benefit that higher local interconnectivity may provide, it is tempting to speculate that APOE-4 carrier-specific increases in metabolic activity within the default mode network may reflect higher structural local connectivity. This could conceivably contribute to increased amyloid production and aggregation over time (Buckner et al., 2009) (Bero et al., 2011). Though the underlying causes of these different developmental trajectories are currently unknown, it is

clear that the APOE-4 allele does not simply cause reduced anatomical connectivity and cognitive performance across the lifespan (Han and Bondi, 2008). Future structural network studies in developing and young individuals should shed light on the possibility of increased local interconnectivity in APOE-4 carriers.

Many regions that are part of the default mode network showed a negative correlation between age local interconnectivity for APOE-4 carriers in this study; specifically, the right precuneus, left inferior parietal lobule (supramarginal gyrus), ventromedial and orbital prefrontal cortex, and anterior cingulate gyrus have all been cited as components of the DMN (Greicius et al., 2003) (Andrews-Hanna et al., 2010), though there is some heterogeneity in the precise definition of the DMN. Other regions with decreasing local connectivity over time such as the cuneus are not considered part of the DMN but are part of the brain's structural core, anatomically connecting the medial anterior and posterior regions of the brain (Hagmann et al., 2008). The majority of the regions that exhibited significant age-related declines in clustering are connected to one another. Because clustering coefficient is a measure of connectivity amongst a region's first-degree neighbors, the implication is that there is less total connectivity within this network of regions with aging in APOE-4 carriers. These findings are consistent with prior studies showing decreased resting fMRI correlation between the medial prefrontal cortex, lateral parietal cortex, and posterior cingulate in older individuals harboring high amyloid burden (Hedden et al., 2009). In older individuals with subjective memory complaints, amyloid levels have also been associated with cortical thinning of the medial orbital frontal cortex, anterior cingulate, and precuneus (Chételat et al., 2010). Here we found that the combined impact of aging and genetic risk contributes to lower connectivity and cortical thickness within the DMN and other structural hubs as age increases. Furthermore, this decreased interconnectivity appears to have behavioral consequences, as APOE-4 carriers exhibited significant age-related reduction in episodic memory performance. This is consistent with the putative role of the DMN

in episodic memory retrieval (Kim et al., 2010) and suggests a potential link between anatomical and behavioral phenotypes.

A negative correlation between local interconnectivity and age was also observed for APOE-4 carriers in the inferior temporal (IT) lobe. This region is known to be affected early in the progression of AD, with MCI subjects demonstrating decreased synaptic density (Scheff et al., 2011), decreased cortical thickness (Wang et al., 2009), and decreased cortical volume in APOE-4 carriers with MCI (Tosun et al., 2010). There is also evidence of a APOE x age interaction on cortical thickness in healthy older APOE-4 carriers (Espeseth et al., 2008).

The use of DTI to construct a whole brain fiber network has known limitations. DTI is not ideal for detecting crossing fibers. Nonetheless, the DTI scan used in this study collected data in 30 diffusion weighted directions, affording greater angular resolution than previous DTI tractography-based network analyses that have nonetheless produced anatomically accurate networks. Furthermore, we employed a hybrid probabilistic deterministic tractography method in order to improve sensitivity to the detection of crossing fibers. Finally, because four of the APOE-4 carriers were 4/4 homozygotes, local interconnectivity, cortical thickness, and two episodic memory test showing decline (Delay Total LM and Delay ROF) were tested in the same stepwise regression model after excluding the four homozygotes. All properites remained significantly negatively related to age, though the p value for cortical thickness was marginal (p=.05). This result indicates no significant additive effect of an additional e4 allele.

Here we examined axonal fiber networks in healthy aging APOE-4 carriers and non-carriers and found APOE-4 carriers exhibited an accelerated negative correlation of local structural connections with age that paralleled reduced cortical thickness. Additionally, they demonstrated accelerated decrease of small worldness with age, suggesting a more rapid loss in the balance between global integration and local modularity of information processing. At the regional level, APOE-4 carriers were found to have age-related loss of interconnectivity among regions comprising the default mode network. APOE-4 carriers also demonstrated significant

decreases in performance with age on two different episodic memory tasks that are known to engage the affected regions. Genetic variations in the structure and function of these networks may contribute to differential rates of amyloid production with age and eventual impairment of brain communication efficiency.

Methods

Subject Inclusion and Imaging

55 subjects were recruited from the UCLA Memory Clinic at the Semel Institute for Neuroscience and Human Behavior to participate in an ongoing, comprehensive study of aging and dementia. Subjects performed a diagnostic evaluation that consisted of physical and neurological examinations, a medical history assessment, genotyping for APOE, and neuropsychological testing. We excluded subjects on the basis of left-handedness, a history of neurological or psychiatric disorders, medication affecting cognition, alcohol or substance abuse, head trauma, epilepsy, arterial hypertension, or cardiovascular disease. Blood was drawn from each subject and genotyped for APOE (Foundas et al., 1997). Any subject who possessed at least one APOE-4 allele was categorized as an “APOE-4 carrier”; subjects homozygous for the APOE-3 allele were designated as “non-carriers” or equivalently, “APOE-4 non-carriers”. All e2 carriers were excluded. The study included 30 APOE-4 non-carriers (average age: 63.8 +/- 8.3 years, range: 45-76; 20 female; education: 16.7 +/- 1.8 years; 21 with family history of dementia) and 25 APOE-4 carriers (average age: 60.8 +/- 9.7 years, range 43-78; 12 female; 21 3/4s, 4 4/4s; education 17.5 +/- 3.3 years; 16 with family history of dementia). All subjects in these groups were without dementia, based on 1) MMSE score and 2) a composite neuropsychological test score. Subjects scored 27 or above on the MMSE with the exception of one subject who scored 26 but fell within the normal range on the remaining neuropsychological tests; analyses which excluded that subject found equivalent results. The neuropsychological battery included: 1) Wechsler memory scale, logical memory delayed recall

portion (WMS LM Delay), 2) Buschke-Fuld selective reminding test (Consistent Long Term Retrieval section; Buschke CLTR), 3) Rey Osterrith Complex Figure, delayed recall (Rey-O Delay), 4) Wechsler memory scale, verbal paired associations II (WMS VP), and 5) Wechsler Adult Intelligence Scale III digit span (WAIS Digit Span) (Table 1). All subjects collectively scored within one standard deviation of the age-adjusted average. All subjects received T1 structural and 30-direction DTI scans.

40 subjects were scanned on a 3T Siemens Allegra and 25 subjects were scanned on a Siemens 3T Trio. DTI was run with single shot echo-planar sequences with the following parameters (Trio differences in parentheses): 30 diffusion weighted volumes with gradient vectors taken from the ICBM protocol (Jones et al., 1999), 5 B0 volumes (1), b=800s/mm^2 (1000), axial slicing, TR=7300ms (7000ms), TE=95ms (86ms), k-space matrix=96x96, slice thickness=2.5mm, 55 slices with no gap, field of view=240mm^2, voxel size=2.5mm^3. Subjects also received T1-weighted Magnetization-prepared Rapid Gradient Echo (MP-RAGE) scans with the following parameters: sagittal slicing, TR=2300ms (1900ms), TE=2.93ms (2.26), matrix=192x192 (256x224), slice thickness=1mm, 160 slices with no gap (176), field of view=256mm^2 (218x250), flip angle=8° (9°), voxel size=1mm^3. In order to control for scanner specific differences, scanner was included as a dummy covariate in all subsequent statistical analyses.

DTI Processing and Tractography

Scans were processed using programs from the FMRIB Software Library (FSL; www.fmrib.ox.ac.uk/fsl/*).* Raw DTI images were first corrected for eddy current distortions using a 12 degree-of-freedom affine registration to the first B0 volume. Diffusion tensors were then estimated at each voxel and fractional anisotropy (FA) images were created. The probability distribution of fiber direction(s) in each voxel was estimated using BEDPOSTX, configured to allow for up to two crossing fibers within each voxel (Behrens et al., 2007). The dyads for the

first and second vectors of diffusion direction within each voxel were used for tractography. Typically these dyads are used as the input to a probabilistic tractography program. However, probabilistic estimates of structural connectivity can be difficult to interpret when building a connectivity matrix. For this reason, we used these dyad vectors as the input for deterministic tractography using the fiber assignment by continuous tracking (FACT) algorithm in Diffusion Toolkit (Mori and Van Zijl, 2002) (Wang et al., 2007). Whole brain tractography was carried out propagating fibers from each voxel with a maximum turn angle of 50°. Fibers were smoothed using a spline filter and all fibers shorter than 5mm were excluded. In order to obtain each subject's connectivity matrix, the brain was partitioned into 110 regions using the Harvard-Oxford subcortical and cortical probabilistic atlases. Regions included 16 subcortical structures (excluding the midbrain) and 47 cortical regions from each hemisphere (Supplementary Table 1). All masks were then transformed to subject diffusion space (SI for details). Each regional mask was thresholded below the 10% probability level, which allowed the inclusion of the gray/white matter interface. Next, the set of fibers connecting each region were counted. A fiber was defined as connecting two regions if one fiber endpoint lay within one region and the other endpoint lay within the other region. This process was repeated using all 110 regions as seeds in order to derive a whole brain connectivity matrix, using custom software written for this purpose (UCLA Multimodal Connectivity Package; http://github.com/jbrown81/umcp). To control for false positives, any region-region pair with less than 3 connecting fibers had its connection strength set to 0.

Network Construction

Network metrics for each subject were quantified using the Brain Connectivity Toolbox (http://sites.google.com/a/brain-connectivity-toolbox.net/bct/metrics). All analyses used weighted networks in order to calculate the node strengths, clustering coefficients, characteristic path lengths, betweenness centrality, and small worldness. Deterministic tractography resulted in a

discrete number of fibers connecting any two brain regions. Because the regions from the Harvard Oxford Atlas varied in volume ($450mm^3$ - $46800mm^3$), the fiber counts had to be adjusted for the unequal number of seed voxels in each region. The fiber connectivity metric between two regions was therefore scaled by the mean of the two regions' volumes. This step had the additional benefit of correcting for individual variations in brain size with finer accuracy than can be achieved with a global correction for brain volume. Connectivity matrices resulted and ranged between 16.1% and 23.7% of regions connected. These individual variations in connection "density" had no significant relationship to any neuropsychological measure and declined with age at nearly equal rates in the APOE-4 carriers and non-carriers. We sought to compare subject networks at their intrinsic densities, rather than artificially removing connections to force equivalent density (Zalesky et al., 2010), and therefore did not perform thresholding. To control for individual differences in density, total network cost was included as a covariate in all statistical analyses. In order to account for the white matter "fidelity", each connection weight was scaled by the averaged fractional anisotropy (FA) for all fibers comprising that connection.

Network Metrics

All analyses were performed on weighted fiber networks. The formulas used to quantify all metrics are described in detail elsewhere (Rubinov and Sporns, 2010) and implementations of these from the Brain Connectivity Toolbox were used. For details on metrics calculated in this study, see the Supplementary Material.

Cortical Thickness

Cortical thickness values were obtained based on the analysis of the MP-RAGE scans using the Freesurfer package (http://surfer.nmr.mgh.harvard.edu) (Fischl and Dale, 2000). Specifically, the recon-all program was used to normalize image intensities, skull strip, and

automatically delineate the white matter and pial (gray matter) surfaces based on the use of intensity gradients to optimally place the borders between tissue types. The distance between the surfaces was measured for ~220000 vertex pairs per subject. The average of these thickness measures was used as the measurement of mean cortical thickness for each subject.

Statistical Analysis

All age-related analyses calculated Pearson's partial correlation coefficient (and the associated p value) between age and the global/regional network metric of interest, separately for APOE-4 carriers and non-carriers, after controlling for the effects of gender, scanner, and total network cost for structural network metrics. To assess between group differences, we used a stepwise regression model that began with terms for APOE genotype (carrier/non-carrier), gender, age, APOE x age interaction, years of education, family history of dementia (yes/no). For all scanning-related metrics, we included a dummy variable for scanner (Allegra/Trio). For structural network metrics, we included a total network cost term to account for the individual differences in fiber volume. The stepwise regression procedure returns the subset of terms that produce the most accurate linear regression model, along with their associated p-values. For behavioral measures and global network measures, a p-value of .05 was used to determine significant correlation. For regional network measures, the p-values for a given measure were adjusted to correct for multiple comparisons using a false discovery rate (FDR) procedure with a q value of .05. Regional network measures were predicted with a robust regression model that downweighted outlying observations. Because education and family history were not significant in any of the regression models tested, they were excluded from the partial correlation tests.

Supplementary Material

Subcortical
'left thalamus'
'left caudate'
'left putamen'

'left pallidum'
'left hippocampus'
'left amygdala'
'left accumbens'
'right thalamus'
'right caudate'
'right putamen'
'right pallidum'
'right hippocampus'
'right amygdala'
'right accumbens'
Cortical
'left frontal pole'
'right frontal pole'
'left insular cortex'
'right insular cortex'
'left superior frontal gyrus'
'right superior frontal gyrus'
'left middle frontal gyrus'
'right middle frontal gyrus'
'left inferior frontal gyrus, pars triangularis'
'right inferior frontal gyrus, pars triangularis'
'left inferior frontal gyrus, pars opercularis'
'right inferior frontal gyrus, pars opercularis'
'left precentral gyrus'
'right precentral gyrus'
'left temporal pole'
'right temporal pole'
'left superior temporal gyrus, anterior division'
'right superior temporal gyrus, anterior division'
'left superior temporal gyrus, posterior division'
'right superior temporal gyrus, posterior division'
'left middle temporal gyrus, anterior division'
'right middle temporal gyrus, anterior division'
'left middle temporal gyrus, posterior division'
'right middle temporal gyrus, posterior division'
'left middle temporal gyrus, temporooccipital part'
'right middle temporal gyrus, temporooccipital part'
'left inferior temporal gyrus, anterior division'
'right inferior temporal gyrus, anterior division'
'left inferior temporal gyrus, posterior division'
'right inferior temporal gyrus, posterior division'
'left inferior temporal gyrus, temporooccipital part'
'right inferior temporal gyrus, temporooccipital part'
'left postcentral gyrus'
'right postcentral gyrus'
'left superior parietal lobule'
'right superior parietal lobule'
'left supramarginal gyrus, anterior division'

'right supramarginal gyrus, anterior division'
'left supramarginal gyrus, posterior division'
'right supramarginal gyrus, posterior division'
'left angular gyrus'
'right angular gyrus'
'left lateral occipital cortex, superior division'
'right lateral occipital cortex, superior division'
'left lateral occipital cortex, inferior division'
'right lateral occipital cortex, inferior division'
'left intracalcarine cortex'
'right intracalcarine cortex'
'left frontal medial cortex'
'right frontal medial cortex'
'left juxtapositional lobule cortex'
'right juxtapositional lobule cortex'
'left subcallosal cortex'
'right subcallosal cortex'
'left paracingulate gyrus'
'right paracingulate gyrus'
'left cingulate gyrus, anterior division'
'right cingulate gyrus, anterior division'
'left cingulate gyrus, posterior division'
'right cingulate gyrus, posterior division'
'left precuneous cortex'
'right precuneous cortex'
'left cuneal cortex'
'right cuneal cortex'
'left frontal orbital cortex'
'right frontal orbital cortex'
'left parahippocampal gyrus, anterior division'
'right parahippocampal gyrus, anterior division'
'left parahippocampal gyrus, posterior division'
'right parahippocampal gyrus, posterior division'
'left lingual gyrus'
'right lingual gyrus'
'left temporal fusiform cortex, anterior division'
'right temporal fusiform cortex, anterior division'
'left temporal fusiform cortex, posterior division'
'right temporal fusiform cortex, posterior division'
'left temporal occipital fusiform cortex'
'right temporal occipital fusiform cortex'
'left occipital fusiform cortex'
'right occipital fusiform cortex'
'left frontal opercular cortex'
'right frontal opercular cortex'
'left central opercular cortex'
'right central opercular cortex'
'left parietal opercular cortex'
'right parietal opercular cortex'

'left planum polare'
'right planum polare'
'left heschl's gyrus'
'right heschl's gyrus'
'left planum temporale'
'right planum temporale'
'left supracalcarine cortex'
'right supracalcarine cortex'
'left occipital pole'
'right occipital pole'

Table S1
List of the 110 regions from the Harvard-Oxford Subcortical and Cortical Atlases.

APOE-4 NC	APOE-4
Left Angular Gyrus	Left Insular Cortex
Left Precuneus	Right Insular Cortex
Left Superior Temporal Gyrus (Posterior)	Left Posterior Cingulate
Left Intracalcarine Cortex	Right Cuneal Cortex
Right Supramarginal Gyrus (Posterior)	Left Temporal Pole
Left Posterior Cingulate	Right Temporal Pole
Left Insular Cortex	Right Intracalcarine Cortex
Left Supramarginal Gyrus (Posterior)	Right Posterior Cingulate
Right Insular Cortex	Right Precuneus
Left Lateral Occipital Cortex (Superior)	Left Supramarginal Gyrus (Posterior)
Right Intracalcarine Cortex	Right Frontal Orbital Cortex
Left Middle Temporal Gyrus (Temporooccipital)	Right Lingual Gyrus

Table S2
Top 12 regions with highest combined rank for strength, betweenness centrality, and regional short path length for APOE-4 non-carriers (APOE-4 NC) and APOE-4 carriers.

Lobe	Regions	APOE-4 NC Age Correlation	APOE-4 Age Correlation
Parietal	inferior parietal, precuneus, superior parietal, supramarginal	r=-.41, p=.07	r=-.58, p=.007
Temporal	bank of superior temporal sulcus, entorhinal, inferior temporal, middle temporal, parahippocampal, superior temporal, temporal pole, transverse temporal, fusiform	r=.04, p=.85	r=.18, p=.44
Frontal	caudal middle frontal, lateral orbitofrontal, medial orbitofrontal, pars	r=-.39, p=.09	r=-.62, p=.003

	opercularis, pars orbitalis, pars triangularis, rostral middle frontal, superior frontal, frontal pole		
Occipital	cuneus, lateral occipital, pericalcarine, lingual	r=-.16, p=.5	r=-.43, p=.06
Limbic	posterior cingulate, isthmus of cingulate, anterior cingulate	r=.04, p=.85	r=-.33, p=.15

Table S3
Regions from Freesurfer cortical thickness analysis included in each lobe, along with the correlation of lobe thickness with age separately for APOE-4 non-carriers (APOE-4 NC) and APOE-4 carriers.

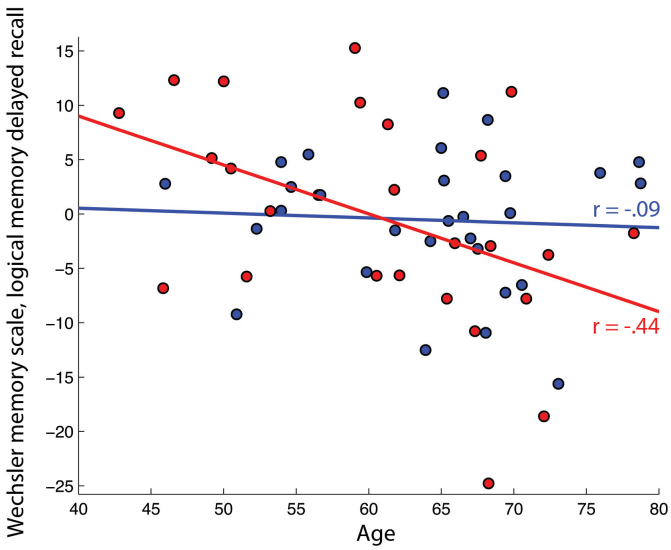
Wechsler memory scale, logical memory delayed recall
15
10
5
0
−5
−10
−15
−20
−25
40
45
50
55
60
65
70
75
80
Age
r = -.09
r = -.44

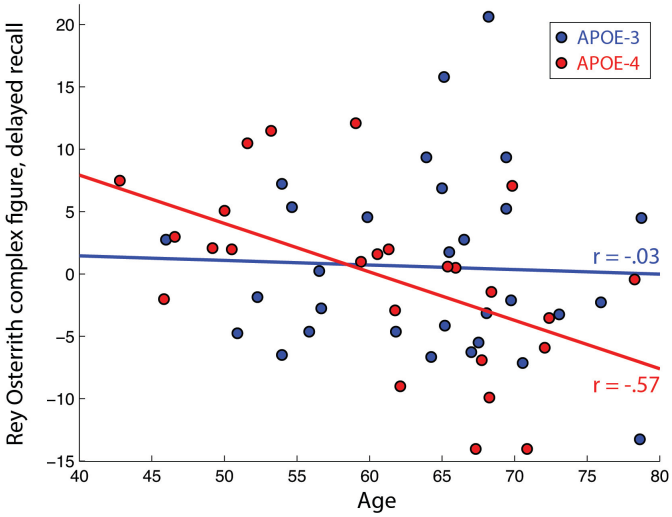
Rey Osterrith complex figure, delayed recall
20
15
10
5
0
−5
−10
−15
40
45
50
55
60
65
70
75
80
Age
APOE-3
APOE-4
r = -.03
r = -.57

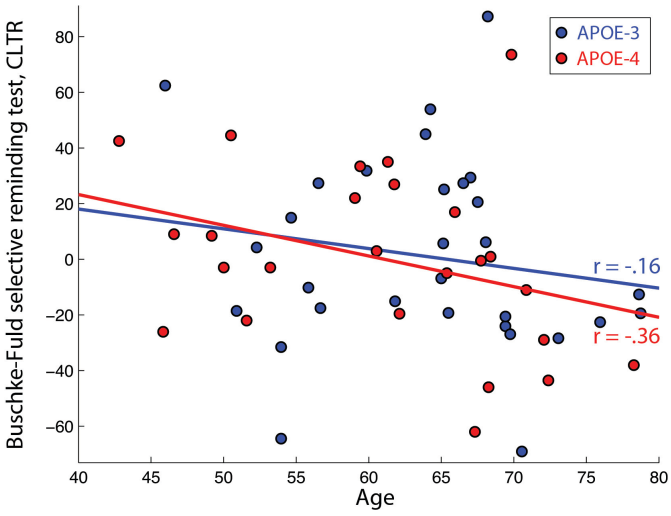
Buschke-Fuld selective reminding test, CLTR
80
60
40
20
0
−20
−40
−60
40
45
50
55
60
65
70
75
80
Age
APOE-3
APOE-4
r = -.16
r = -.36

Figure S1
Wechsler memory scale (logical memory delayed recall portion; WMS LM Delay), Rey Osterrith Complex Figure (delayed recall; Rey-O Delay), and Buschke-Fuld selective reminding test (consistent long-term retrieval section; Buschke CLTR) residuals based on partial correlations with age plotted for APOE-4 noncarriers (APOE-3; blue) and APOE-4 carriers (red). Partial correlations controlled for gender. Both WMS LM Delay and Rey-O delay had a significant interaction between APOE genotype ($p < .05$).

Supplemental Text

DTI Registration

Regional masks were transformed to each subject's diffusion space using a multistage registration process. First, the high-resolution structural image (MPRAGE) was skull stripped using BET. Next, the FA image was affine registered to the MPRAGE using 12 DOF and a mutual information cost function using FSL's Linear Image Registration Tool (FLIRT). The MPRAGE was then affine registered to the MNI152 brain using 12 DOF and a correlation ratio cost function. These two transformation matrices were multiplied and inverted in order to obtain the standard space-to-diffusion space transformation matrix.

Network Metric Details

Given a weighted connectivity matrix, strength was calculated as the total weight of connections to a given node. To calculate cost, for each region-region connection the product of fiber count (i.e. connection weight, w_{ij}), average fiber length (l_{ij}), and average fiber FA (fa_{ij}) and was taken. The sum of all region-region costs was computed to derive the total network cost:

$$\sum w_{ij} \bar{l}_{ij} fa_{ij}$$

For each node, the subgraph was defined as the subset of connections between the node and its first-degree neighbors. The clustering coefficient for a node was calculated as the ratio of the number of actual connections among the neighbors in the subgraph to the number of possible connections, scaled by the edge weights.

In order to calculate path lengths within the networks, the distance matrix was first

defined. Distance was defined in two parts: first, the inverse of fiber density between two regions was calculated, with the rationale that a denser connection enables more communication and is equivalent to a shorter distance. Second, this distance was scaled by the actual average length of fibers connecting the regions. This allowed the quantification of network path lengths in terms of true physical distance. Shortest paths were determined between all pairs of nodes (e.g. node A and node B) in the network by finding the shortest distance between node A and B. This was done using Djikstra's algorithm, which finds all possible paths between A and B that travel through a unique, non-looping set of other nodes. These paths are then sorted by distance, where distance is the product of the connection weight for each jump between nodes along the path and the anatomical distance between those nodes. Characteristic path length measured the average shortest path length in the network.

Small worldness for a network was calculated with respect to a set of equivalent "null" random networks that have the same sum of weights as the real network but have been randomly rewired. For each subject's structural network, we calculated 1000 random networks for comparison. Normalized clustering coefficient was calculated as the ratio of the clustering coefficient from the real network to the average clustering coefficient of the 1000 random networks. Normalized characteristic path length was calculated in the same fashion. Small worldness was quantified as the ratio of normalized clustering coefficient and normalized characteristic path length.

Network measures were calculated with the Brain Connectivity Toolbox which is based on formulas described elsewhere (Rubinov and Sporns, 2010). Briefly, strength was calculated as:

$k_i = \sum w_{ij}$ where w_{ij} is the weight between nodes i and j.

Clustering coefficient was calculated as:

$$C = \frac{1}{n}\sum \frac{\sum (w_{ij} w_{ih} w_{jh})^{1/3}}{k_i (k_i - 1)}$$ where all w are weights and k is the number of nodes in the local, first-degree neighborhood.

Characteristic path length was calculated as:

$$L = \frac{1}{n}\sum \frac{\sum d_{ij}}{n-1}$$ where d_{ij} is the path weight between any nodes i and j in the network that pass through the specified node. The average of these path weights is the average path weight for the node. The average of the average path weights for each node is the characteristic path length.

Normalized clustering coefficient (l) was calculated as:

$$\lambda = \frac{CC_{real}}{CC_{random}}$$

where CC_{random} is the mean CC from the 1000 random networks.

Normalized characteristic path length (g) was then:

$$\gamma = \frac{CPL_{real}}{CPL_{random}}$$ where again CPL_{random} is the mean from 1000 random networks

Finally, small worldness (s) was the ratio:

$$\sigma = \frac{\lambda}{\gamma}$$

A small world network has no isolated nodes, $\lambda >> 1$, $\gamma \sim = 1$, and $\sigma > 1.2$.

Graph Visualization

Network graphs were rendered using matplotlib (http://matplotlib.sourceforge.net), and networkX (http://networkx.lanl.gov).

Acknowledgements and Disclosures

Special thanks to Mike Jones and Brian Renner for data collection. Jeff Rudie provided valuable review of the manuscript. The work was supported by an NIH NRSA 1F31AG035438-01 to JAB and by NIH grants P01-AG025831, AG13308, P50 AG 16570, MH/AG58156, MH52453; AG10123; M01-RR00865, the Department of Energy (DOE contract DE-FC03-87-ER60615); General Clinical Research Centers Program; the Fran and Ray Stark Foundation Fund for Alzheimer's Disease Research; the Ahmanson Foundation. Dr. Small reports having served as a consultant and/or having received lecture fees from Dakim, Eisai, Forest, Medivation, Novartis, and Pfizer. Dr. Small also reports having received stock options from Dakim.

Chapter 2 References

Achard, S., Bullmore, E., 2007. Efficiency and Cost of Economical Brain Functional Networks. PLoS Comput Biol 3, e17.

Andrews-Hanna, J.R., Reidler, J.S., Sepulcre, J., Poulin, R., Buckner, R.L., 2010. Functional-anatomic fractionation of the brain's default network. Neuron 65, 550–562.

Bartzokis, G., Lu, P.H., Geschwind, D.H., Edwards, N., Mintz, J., Cummings, J.L., 2006. Apolipoprotein E genotype and age-related myelin breakdown in healthy individuals: implications for cognitive decline and dementia. Arch Gen Psychiatry 63, 63–72.

Bartzokis, G., Lu, P.H., Mintz, J., 2007. Human brain myelination and amyloid beta deposition in Alzheimer's disease. Alzheimers Dement 3, 122–125.

Bassett, D.S., Bullmore, E.T., Meyer-Lindenberg, A., Apud, J.A., Weinberger, D.R., Coppola, R., 2009. Cognitive fitness of cost-efficient brain functional networks. Proceedings of the National Academy of Sciences 106, 11747–11752.

Behrens, T.E.J., Berg, H.J., Jbabdi, S., Rushworth, M.F.S., Woolrich, M.W., 2007. Probabilistic diffusion tractography with multiple fibre orientations: What can we gain? NeuroImage 34, 144–155.

Bero, A.W., Yan, P., Roh, J.H., Cirrito, J.R., Stewart, F.R., Raichle, M.E., Lee, J.-M., Holtzman, D.M., 2011. Neuronal activity regulates the regional vulnerability to amyloid-[beta] deposition. Nat Neurosci 14, 750–756.

Bookheimer, S., Burggren, A., 2009. APOE-4 Genotype and Neurophysiological Vulnerability to Alzheimer's and Cognitive Aging. Annu. Rev. Clin. Psychol. 5, 343–362.

Bookheimer, S.Y., Strojwas, M.H., Cohen, M.S., Saunders, A.M., Pericak-Vance, M.A., Mazziotta, J.C., Small, G.W., 2000. Patterns of Brain Activation in People at Risk for Alzheimer's Disease. N Engl J Med 343, 450–456.

Buckner, R.L., Sepulcre, J., Talukdar, T., Krienen, F.M., Liu, H., Hedden, T., Andrews-Hanna, J.R., Sperling, R.A., Johnson, K.A., 2009. Cortical Hubs Revealed by Intrinsic Functional Connectivity: Mapping, Assessment of Stability, and Relation to Alzheimer's Disease. J. Neurosci. 29, 1860–1873.

Bullmore, E., Sporns, O., 2009. Complex brain networks: graph theoretical analysis of structural and functional systems. Nat Rev Neurosci 10, 186–98.

Caselli, R.J., Dueck, A.C., Osborne, D., Sabbagh, M.N., Connor, D.J., Ahern, G.L., Baxter, L.C., Rapcsak, S.Z., Shi, J., Woodruff, B.K., Locke, D.E.C., Snyder, C.H., Alexander, G.E., Rademakers, R., Reiman, E.M., 2009. Longitudinal modeling of age-related memory decline and the APOE epsilon4 effect. N. Engl. J. Med 361, 255–263.

Caselli, R.J., Reiman, E.M., Osborne, D., Hentz, J.G., Baxter, L.C., Hernandez, J.L., Alexander, G.G., 2004. Longitudinal changes in cognition and behavior in asymptomatic carriers of the APOE e4 allele. Neurology 62, 1990–1995.

Chételat, G., Villemagne, V.L., Bourgeat, P., Pike, K.E., Jones, G., Ames, D., Ellis, K.A., Szoeke, C., Martins, R.N., O'Keefe, G.J., Salvado, O., Masters, C.L., Rowe, C.C., 2010. Relationship between atrophy and beta-amyloid deposition in Alzheimer disease. Ann. Neurol 67, 317–324.

Corder, E.H., Saunders, A.M., Strittmatter, W.J., Schmechel, D.E., Gaskell, P.C., Small, G.W., Roses, A.D., Haines, J.L., Pericak-Vance, M.A., 1993. Gene dose of apolipoprotein E type 4 allele and the risk of Alzheimer's disease in late onset families. Science 261, 921–3.

Delbeuck, X., Van der Linden, M., Collette, F., 2003. Alzheimer's disease as a disconnection syndrome? Neuropsychol Rev 13, 79–92.

Espeseth, T., Westlye, L.T., Fjell, A.M., Walhovd, K.B., Rootwelt, H., Reinvang, I., 2008. Accelerated age-related cortical thinning in healthy carriers of apolipoprotein E epsilon 4. Neurobiol. Aging 29, 329–340.

Filippini, N., MacIntosh, B.J., Hough, M.G., Goodwin, G.M., Frisoni, G.B., Smith, S.M., Matthews, P.M., Beckmann, C.F., Mackay, C.E., 2009. Distinct patterns of brain activity in young carriers of the APOE-ε4 allele. Proceedings of the National Academy of Sciences 106, 7209 –7214.

Fischl, B., Dale, A.M., 2000. Measuring the thickness of the human cerebral cortex from magnetic resonance images. Proc. Natl. Acad. Sci. U.S.A 97, 11050–11055.

Fleisher, A.S., Sherzai, A., Taylor, C., Langbaum, J.B.S., Chen, K., Buxton, R.B., 2009. Resting-state BOLD networks versus task-associated functional MRI for distinguishing Alzheimer's disease risk groups. NeuroImage 47, 1678–1690.

Foundas, A.L., Leonard, C.M., Mahoney, S.M., Agee, O.F., Heilman, K.M., 1997. Atrophy of the hippocampus, parietal cortex, and insula in Alzheimer's disease: a volumetric magnetic resonance imaging study. Neuropsychiatry Neuropsychol Behav Neurol 10, 81–89.

Greicius, M.D., Krasnow, B., Reiss, A.L., Menon, V., 2003. Functional connectivity in the resting brain: A network analysis of the default mode hypothesis. Proceedings of the National Academy of Sciences of the United States of America 100, 253 –258.

Greicius, M.D., Srivastava, G., Reiss, A.L., Menon, V., 2004. Default-mode network activity distinguishes Alzheimer's disease from healthy aging: Evidence from functional MRI. Proceedings of the National Academy of Sciences of the United States of America 101, 4637–4642.

Hagmann, P., Cammoun, L., Gigandet, X., Meuli, R., Honey, C.J., Wedeen, V.J., Sporns, O., 2008. Mapping the Structural Core of Human Cerebral Cortex. PLoS Biology 6, e159 EP –.

Hagmann, P., Sporns, O., Madan, N., Cammoun, L., Pienaar, R., Wedeen, V.J., Meuli, R., Thiran, J.-P., Grant, P.E., 2010. White matter maturation reshapes structural connectivity in the late developing human brain. Proceedings of the National Academy of Sciences 107, 19067 –19072.

Han, S.D., Bondi, M.W., 2008. Revision of the apolipoprotein E compensatory mechanism recruitment hypothesis. Alzheimer's and Dementia 4, 251–254.

Han, S.D., Drake, A.I., Cessante, L.M., Jak, A.J., Houston, W.S., Delis, D.C., Filoteo, J.V., Bondi, M.W., 2007. Apolipoprotein E and traumatic brain injury in a military population: evidence of a neuropsychological compensatory mechanism? Journal of Neurology, Neurosurgery & Psychiatry 78, 1103 –1108.

Hedden, T., Van Dijk, K.R.A., Becker, J.A., Mehta, A., Sperling, R.A., Johnson, K.A., Buckner, R.L., 2009. Disruption of Functional Connectivity in Clinically Normal Older Adults Harboring Amyloid Burden. The Journal of Neuroscience 29, 12686 –12694.

Honea, R.A., Vidoni, E., Harsha, A., Burns, J.M., 2009. Impact of APOE on the healthy aging brain: a voxel-based MRI and DTI study. J. Alzheimers Dis 18, 553–564.

Iturria-Medina, Y., Sotero, R.C., Canales-Rodríguez, E.J., Alemán-Gómez, Y., Melie-García, L., 2008. Studying the human brain anatomical network via diffusion-weighted MRI and Graph Theory. NeuroImage 40, 1064–1076.

Jones, D.K., Horsfield, M.A., Simmons, A., 1999. Optimal strategies for measuring diffusion in anisotropic systems by magnetic resonance imaging. Magnetic Resonance in Medicine 42, 515–525.

Kim, H., Daselaar, S.M., Cabeza, R., 2010. Overlapping brain activity between episodic memory encoding and retrieval: Roles of the task-positive and task-negative networks. NeuroImage 49, 1045–1054.

Li, Y., Liu, Y., Li, J., Qin, W., Li, K., Yu, C., Jiang, T., 2009. Brain Anatomical Network and Intelligence. PLoS Comput Biol 5, e1000395.

Lo, C.-Y., Wang, P.-N., Chou, K.-H., Wang, J., He, Y., Lin, C.-P., 2010. Diffusion Tensor Tractography Reveals Abnormal Topological Organization in Structural Cortical Networks in Alzheimer's Disease. J. Neurosci. 30, 16876–16885.

Luo, L., O'Leary, D.D.M., 2005. Axon retraction and degeneration in development and disease. Annu. Rev. Neurosci 28, 127–156.
Mahley, R., 1988. Apolipoprotein E: cholesterol transport protein with expanding role in cell biology. Science 240, 622 –630.
Margulies, D.S., Vincent, J.L., Kelly, C., Lohmann, G., Uddin, L.Q., Biswal, B.B., Villringer, A., Castellanos, F.X., Milham, M.P., Petrides, M., 2009. Precuneus shares intrinsic functional architecture in humans and monkeys. Proceedings of the National Academy of Sciences 106, 20069 –20074.
Mevel, K., Chételat, G., Eustache, F., Desgranges, B., 2011. The Default Mode Network in Healthy Aging and Alzheimer's Disease. International Journal of Alzheimer's Disease 2011, 1–9.
Mondadori, C.R.A., De Quervain, D.J.-F., Buchmann, A., Mustovic, H., Wollmer, M.A., Schmidt, C.F., Boesiger, P., Hock, C., Nitsch, R.M., Papassotiropoulos, A., Henke, K., 2007. Better Memory and Neural Efficiency in Young Apolipoprotein E ε4 Carriers. Cerebral Cortex 17, 1934 –1947.
Mori, S., Van Zijl, P.C.M., 2002. Fiber tracking: principles and strategies - a technical review. NMR Biomed 15, 468–480.
Naj, A.C., Jun, G., Beecham, G.W., Wang, L.-S., Vardarajan, B.N., et al., 2011. Common variants at MS4A4/MS4A6E, CD2AP, CD33 and EPHA1 are associated with late-onset Alzheimer's disease. Nat Genet 43, 436–441.
Persson, J., Lind, J., Larsson, A., Ingvar, M., Cruts, M., Van Broeckhoven, C., Adolfsson, R., Nilsson, L.-G., Nyberg, L., 2006. Altered brain white matter integrity in healthy carriers of the APOE {varepsilon}4 allele: A risk for AD? Neurology 66, 1029–1033.
Raichle, M.E., MacLeod, A.M., Snyder, A.Z., Powers, W.J., Gusnard, D.A., Shulman, G.L., 2001. A default mode of brain function. Proceedings of the National Academy of Sciences 98, 676 –682.
Reiman, E.M., Chen, K., Alexander, G.E., Caselli, R.J., Bandy, D., Osborne, D., Saunders, A.M., Hardy, J., 2005. Correlations between apolipoprotein E ε4 gene dose and brain-imaging measurements of regional hypometabolism. Proceedings of the National Academy of Sciences of the United States of America 102, 8299 –8302.
Rubinov, M., Sporns, O., 2010. Complex network measures of brain connectivity: uses and interpretations. Neuroimage 52, 1059–1069.
Ryan, L., Walther, K., Bendlin, B.B., Lue, L.-F., Walker, D.G., Glisky, E.L., 2011. Age-related differences in white matter integrity and cognitive function are related to APOE status. Neuroimage 54, 1565–1577.
Salat, D.H., Tuch, D.S., Van der Kouwe, A.J.W., Greve, D.N., Pappu, V., Lee, S.Y., Hevelone, N.D., Zaleta, A.K., Growdon, J.H., Corkin, S., Fischl, B., Rosas, H.D., 2010. White matter pathology isolates the hippocampal formation in Alzheimer's disease. Neurobiol. Aging 31, 244–256.
Scheff, S.W., Price, D.A., Schmitt, F.A., Scheff, M.A., Mufson, E.J., 2011. Synaptic Loss in the Inferior Temporal Gyrus in Mild Cognitive Impairment and Alzheimer Disease. J Alzheimers Dis 24, 547–557.
Sheline, Y.I., Morris, J.C., Snyder, A.Z., Price, J.L., Yan, Z., D'Angelo, G., Liu, C., Dixit, S., Benzinger, T., Fagan, A., Goate, A., Mintun, M.A., 2010. APOE4 Allele Disrupts Resting State fMRI Connectivity in the Absence of Amyloid Plaques or Decreased CSF A{beta}42. J. Neurosci. 30, 17035–17040.
Small, G.W., Ercoli, L.M., Silverman, D.H., Huang, S.C., Komo, S., Bookheimer, S.Y., Lavretsky, H., Miller, K., Siddarth, P., Rasgon, N.L., Mazziotta, J.C., Saxena, S., Wu, H.M., Mega, M.S., Cummings, J.L., Saunders, A.M., Pericak-Vance, M.A., Roses, A.D., Barrio, J.R., Phelps, M.E., 2000. Cerebral metabolic and cognitive decline in persons at genetic risk for Alzheimer's disease. Proc Natl Acad Sci U S A 97, 6037–42.

Small, G.W., Siddarth, P., Burggren, A.C., Kepe, V., Ercoli, L.M., Miller, K.J., Lavretsky, H., Thompson, P.M., Cole, G.M., Huang, S.C., Phelps, M.E., Bookheimer, S.Y., Barrio, J.R., 2009. Influence of cognitive status, age, and APOE-4 genetic risk on brain FDDNP positron-emission tomography imaging in persons without dementia. Arch. Gen. Psychiatry 66, 81–87.

Sporns, O., 2010. Networks of the Brain, 1st ed. The MIT Press.

Stam, C., Jones, B., Nolte, G., Breakspear, M., Scheltens, P., 2007. Small-World Networks and Functional Connectivity in Alzheimer's Disease. Cereb. Cortex 17, 92–99.

Stricker, N.H., Schweinsburg, B.C., Delano-Wood, L., Wierenga, C.E., Bangen, K.J., Haaland, K.Y., Frank, L.R., Salmon, D.P., Bondi, M.W., 2009. Decreased white matter integrity in late-myelinating fiber pathways in Alzheimer's disease supports retrogenesis. Neuroimage 45, 10–16.

Supekar, K., Menon, V., Rubin, D., Musen, M., Greicius, M.D., 2008. Network analysis of intrinsic functional brain connectivity in Alzheimer's disease. PLoS Comput. Biol 4, e1000100.

Thompson, P.M., Hayashi, K.M., De Zubicaray, G., Janke, A.L., Rose, S.E., Semple, J., Herman, D., Hong, M.S., Dittmer, S.S., Doddrell, D.M., Toga, A.W., 2003. Dynamics of gray matter loss in Alzheimer's disease. J. Neurosci 23, 994–1005.

Tosun, D., Schuff, N., Truran-Sacrey, D., Shaw, L.M., Trojanowski, J.Q., Aisen, P., Peterson, R., Weiner, M.W., 2010. Relations between brain tissue loss, CSF biomarkers and the ApoE genetic profile: A longitudinal MRI study. Neurobiol Aging 31, 1340–1354.

Tuminello, E.R., Han, S.D., 2011. The apolipoprotein e antagonistic pleiotropy hypothesis: review and recommendations. Int J Alzheimers Dis 2011, 726197.

Wang, L., Goldstein, F.C., Veledar, E., Levey, A.I., Lah, J.J., Meltzer, C.C., Holder, C.A., Mao, H., 2009. Alterations in Cortical Thickness and White Matter Integrity in Mild Cognitive Impairment Measured by Whole-Brain Cortical Thickness Mapping and Diffusion Tensor Imaging. AJNR Am J Neuroradiol 30, 893–899.

Wang, R., Benner, T., Sorensen, A.G., Wedeen, V., 2007. Diffusion Toolkit: A Software Package for Diffusion Imaging Data Processing and Tractography. Proc Intl Soc Mag Reson Med 15, 3720.

Zalesky, A., Fornito, A., Harding, I.H., Cocchi, L., Yücel, M., Pantelis, C., Bullmore, E.T., 2010. Whole-brain anatomical networks: does the choice of nodes matter? Neuroimage 50, 970–983.

Zhou, Y., Dougherty Jr, J.H., Hubner, K.F., Bai, B., Cannon, R.L., Hutson, R.K., 2008. Abnormal connectivity in the posterior cingulate and hippocampus in early Alzheimer's disease and mild cognitive impairment. Alzheimer's and Dementia 4, 265–270.

Chapter 3

Adaptive Modularity of Memory Encoding Networks Predicts APOE-4 Dependent Hippocampal Activity Reduction

Introduction

Among the risk factors for developing late-onset Alzheimer's Disease (AD), two stand out above the rest: old age and possession of at least one copy of the APOE e4 (APOE-4) allelic variant (Corder et al., 1993). The study of aging APOE-4 carriers with respect to non-carriers is critical for unraveling the interactive effect of aging and genetics on AD biomarkers. The most well-established MRI-based biomarker is structural atrophy in the medial temporal lobe (MTL) (DeCarli et al., 2007) (Desikan et al., 2009), including the hippocampus and entorhinal cortex. Reduced hippocampal volume and ERC thicknesses in individuals with mild cognitive impairment (MCI) are predictive of cognitive decline and eventual conversion to AD (Devanand et al., 2007). Aging APOE-4 carriers also exhibit cortical thinning in the ERC and neighboring structures that relate to declines in AD-compromised cognitive domains such as episodic memory encoding (Burggren et al., 2008) (Burggren et al., 2011).

At a cellular level, the entorhinal cortex (ERC) is one of the first brain regions to exhibit pathological changes in Alzheimer's Disease (AD) (Braak and Braak, 1991) (Gómez-Isla et al., 1996). This periallocortical region serves as the primary source of input to the hippocampus, aggregating cortical input from the neighboring perirhinal and parahippocampal cortices, which themselves receive a wide swath of inputs from unimodal and polymodal regions in the frontal/temporal/parietal lobes and retrosplenial cortex (Squire et al., 2004). Recent rodent studies demonstrated that exogenous human tau protein genetically expressed in the entorhinal cortex layer II eventually appeared in the hippocampus and cingulate cortex and resulted in synaptic loss (De Calignon et al., 2012), supporting the ERCs central role in disease propagation.

In healthy humans, resting state fMRI (rsfMRI) functional connectivity (FC) has shown that the hippocampal formation couples with the default mode network (DMN) in its ventral/anterior aspect (Andrews-Hanna et al., 2010). The DMN is of primary interest in AD because of its reduced functional coherence with disease progression (Greicius et al., 2004) (Damoiseaux et al., 2012a), its correspondence with the pattern of amyloid-beta deposition in AD (Buckner et al., 2009), and its involvement in episodic memory encoding and retrieval (Kim et al., 2010) (Sestieri et al., 2011).

APOE-4 carriers have demonstrated complex alterations in FC. The most well established finding is altered functional connectivity in the DMN (Sheline et al., 2010b) (Machulda MM, 2011) (Damoiseaux et al., 2012b) (Filippini et al., 2009), although the detected directions of that change (increase or decrease) have been variable. These factors are likely driven by age, gender, and other demographic variations. Meanwhile, task-based differences in APOE-4 carriers have been equally variable in their findings. During memory encoding, both increases and decreases in activity in the medial temporal lobe have been reported (Bookheimer et al., 2000) (Dickerson et al., 2005) (Suthana et al., 2010) (Filippini et al., 2011) (Adamson et al., 2011).

While rsfMRI has been a valuable tool for mapping altered functional networks in individuals with AD or AD risk, functional connectivity is an ongoing, dynamic process that is constantly reconfiguring in the service of specific cognitive functions (Bassett et al., 2011b; Ekman et al., 2012) (Fornito et al., 2012). Given the domain-specific impairments caused by AD, the measurement of functional activity and connectivity during relevant tasks may be more sensitive to perturbed dynamics caused by the disease in its preclinical stage.

Here we examined ERC fMRI activity and whole brain connectivity in aging APOE-4 carriers and non-carriers during an episodic memory encoding task and assessed the relationship between them.

Materials and Methods

Patient Enrollment

Aging adults were recruited to the UCLA Aging and Memory Center as part of an ongoing study on aging and dementia. All subjects included in the current study had no history of neurological or psychiatric disorder. Subjects were also excluded on the basis of left-handedness, significant brain trauma/abnormality, substantial substance abuse, epilepsy, arterial hypertension, or cardiovascular disease. Subjects completed a neuropsychological battery that included tests in the domains of working memory, long-term memory, and executive functioning. Based on the outcome of these tests, subjects were given a clinical diagnosis of age-normal performance, mild cognitive impairment, or probable Alzheimer's Disease. Only probable AD subjects were excluded from this study. Blood was drawn from each subject and assessed for APOE genotype using the procedure described in (Suthana et al., 2010). The study includes x 3/3 carriers, x 2/3, x 3/4, and x4/4. All statistical tests were performed with the exclusion of e2 carriers and found to remain statistically significant. Subject demographics and neuropsychological performance are listed in table 1.

Characteristic	**APOE-4 carriers (N=19/21)**	**APOE-4 non-carriers (N=19)**
Age	64.5 +/- 8.8 (64.5 +/-9.7)	59.6 +/- 7.7
Age range	47-79 (47-79)	46-78
Homozygotes	3 (3)	17**
Gender	10F/9M (11F/10M)	13F/6M
Family history of dementia	10 (12)	9
Years of education	17.1 +/- 2.6 (16.8 +/- 2.8)	15.7 +/-2.2
MMSE*	28.3 +/- .9 (28.4 +/- 1.5)	29.3 +/- .9
WMS LM delay	25.5 +/- 7.3 (25.8 +/- 7.3)	28.4 +/- 7.7
Buschke CLTR	63.1 +/- 40.6 (61.1 +/- 38.9)	74.3 +/- 35.5
Rey-O delay	13.7 +/- 4.7 (13.5 +/- 5.3)	15.8 +/- 6.8
Total VP	20.2 +/- 7.4 (20.2 +/- 7.2)	21.5 +/- 7.4

Table 1: Demographic characteristics. Measures show mean +/- standard deviation. Measures in parentheses are after inclusion of additional two subjects for high resolution only scans. Abbreviations: Rey-O delay, Rey–Osterrith Complex Figure, delayed recall; WMS LM delay, Wechsler memory scale, logical memory delayed recall portion; WMS VP, Wechsler memory scale, verbal paired associations II. *: $p < .05$. **: two non-carriers possessed one APOE-2 allele.

Imaging Procedure

Subjects underwent MRI scanning on a Siemens Allegra 3T scanner at the University of California, Los Angeles Ahmanson-Lovelace Brain Mapping Center that included the following sequences: 1) a Whole Brain (WB) T1-weighted structural scan (MP-RAGE; sagittal slicing, TR=2300 ms, TE =2.93 ms, matrix=192 × 192, 160 slices with no gap, field of view = 256 mm^2, flip angle = 8°, and voxel size = 1mm^3), 2) a whole-brain fMRI scan while performing an unrelated-words associative episodic memory encoding and retrieval task (described in *Experimental Design*), 3) a high resolution T2-weighted fast-spin echo structural scan of the bilateral medial temporal lobes with an oblique coronal prescription, oriented perpendicular to the long access of the hippocampus (Hippocampal High Resolution, HHR; TR = 5200 ms, TE = 105 ms, matrix size = 512 × 512, 19 slices with no gap, voxel size: 0.39 × 0.39 × 3 mm), 4) a high resolution fMRI echo-planar scan with the same prescription as in 2) (TR = 3000 ms, TE = 39 ms, 19 slices with no gap, voxel size = 1.6 × 1.6 × 3 mm) while performing the same task as in 2), and 5) a HHR scan with the bandwidth matched to the HHR fMRI (TR = 5000 ms, TE = 66 ms, 19 slices with no gap, voxel size = 1.6 × 1.6 × 3 mm). The order of 2 and 4 was randomized across subjects. After assessing data quality and ensuring proper compliance with the task, a total of 43 subjects with HHR fMRI data were included in the analysis, 41 of whom also had WB data.

Experimental Design

The fMRI task instructed subjects to learn the association of unrelated pairs of words displayed simultaneously (e.g. “jazz” and “beast” or “clock” and “green”). During each encoding block of the task, subjects were shown seven pairs. This was followed by a 30 second baseline block during which the subject was shown a symbol (“+” or “o”) in the center of the screen and instructed to press a button every time the symbol changed. This was followed by a retrieval block where the subject was shown a single word and asked to silently recall the second word. They were instructed to press a button if they did recall the unseen word in the pair. Six blocks of encoding and retrieval were completed. Subjects were tested on these word pairs immediately after the scan in order to check accurate recall. Prior to the scan, subjects were trained on the identical task with different word pairs in order to familiarize them with the task and to assess memory performance.

Image Analysis – Structural

In order to define precise, subject-specific MTL subregions, we used a manual segmenting technique that has been previously described in detail (Suthana et al., 2010; Zeineh et al., 2000). Briefly, HHR structural scans were traced for gray matter, white matter, and CSF. Landmarks at boundaries were used to demarcate regions of interest (ROIs) for CA1, CA2/3/Dentate Gyrus (CA2/3/DG, which could not be resolved further), entorhinal cortex (ERC), perirhinal cortex (PRC), parahippocampal cortex (PHC), and subiculum (SUB). Example ROIs for one subject are shown in **Figure 1**. The CA1, CA2/3/DG, and SUB were further divided into anterior and posterior portions corresponding to the head and body/tail of the hippocampus, respectively. Because these regions were defined in the same field of view as the HHR fMRI scan, ROIs were aligned to the functional image with a 6 degree-of-freedom transform and downsampled to HHR fMRI resolution using the FMRIB Software Library’s Linear Image Registration Tool (FLIRT; all FSL tools described and available at http://fsl.fmrib.ox.ac.uk/fsl/fslwiki/). Cortical thickness for each subregion was also determined

using a procedure described in (Burggren et al., 2008) that measured the maximal distance between boundary gray and non-gray matter pixels within each ROI and then averaged all such measurements within an ROI.

Registration between the HHR structural scan and the WB fMRI scan was the most critical to this experiment. We used a multi-stage registration: 1) HHR structural to WB structural (6 DOF, using a bounding box covering the majority of the brain in coronal sections in order to compensate for the limited field of view), 2) WB structural to WB matched bandwidth (Echo-planar imaging-optimized Boundary Based Registration in FSL), 3) WB matched bandwidth to WB functional (6 DOF). All scans were skull stripped using FSL BET. For parsimony, only linear registrations were applied.

Functional pre-processing

Whole brain fMRI data was analyzed for functional activation using FSL FEAT. Data was corrected for motion using MCFLIRT, smoothed using a Gaussian kernel (5mm FWHM), and skull stripped. In order to make the task fMRI results and the pseudo resting results maximally similar, additional preprocessing was applied. Data were bandpass filtered between .08 and .009 Hz in order to eliminate high and low frequency artifacts while preserving BOLD fluctuations at the timescales of interest, including task activations. Core white matter (WM) and CSF masks were defined on the MNI152 template brain, registered to WB structural spaced, and masked by subject-specific WM and CSF masks created using FSL FAST with a threshold of .9. These masks were registered to the WB fMRI and average timeseries were obtained for WM and CSF. These parameters, their temporal derivatives, and the motion parameters from MCFLIRT were all statistically regressed from the data.

High resolution data were skull stripped using BET, motion corrected using MCFLIRT, high pass filtered and spatially smoothed using a Gaussian kernel of 3mm FWHM. With the resultant images, the transform to the matched bandwidth scan was performed using FLIRT

with a 3 DOF transform. A combined transformation matrix between HHR functional, matched bandwidth, and structural space was then calculated and inverted in order to register all hand traced ROIs into subject functional space.

Functional activity

Single-subject analysis was performed in FEAT using a general linear model that included regressors for encoding and retrieval, both convolved with a double-gamma shaped hemodynamic response function. This model was then run for each subject without thresholding, which was reserved for the group level analysis. Group level analysis was also performed with FEAT, using the FLAME-1 modeling option with cluster thresholding using Z=2.0 and p=.05. A pre-thresholding mask was used that included cortical gray matter, subcortical nuclei, and the cerebellum was created using the FSL Harvard-Oxford cortical/subcortical atlas the the FSL MNI152 cerebellum atlas.

High resolution data were analyzed using custom code written in MATLAB and Python. Task waveforms were convolved with the canonical HRF using the SPM functions spm_get_bf and spm_Volterra (http://www.fil.ion.ucl.ac.uk/spm/). For each MTL ROI, the mean timeseries was extracted and regressed against a model with HRF-convolved variables for encoding and retrieval. Beta parameter estimates were stored for each (subject x ROI) and used for all subsequent analyses.

Functional connectivity

The next step was to obtain whole brain functional task-specific networks. This allowed the application of graph theory tools to assess the importance of various brain regions within the whole brain network. To do this, first a whole brain cortical and subcortical fMRI atlas derived from healthy adults (described in (Brown et al., 2012) was registered to each subject's WB fMRI

scan. This set of atlas ROIs (A-ROIs) were combined with the custom MTL ROIs and any A-ROIs that overlapped MTL-ROIs by more than 5% were excluded. This resulted in a set of 180 regions.

Task-specific functional networks have been assessed in a variety of ways. A simple method is to assess the correlation of different regions during blocks of interest. The shortcoming of this method is that it fails to account for other sources contributing to covariation, including independent coactivation or physiological driving inputs. For this reason, we performed an exhaustive PPI that used each of the 180 ROIs as the seed. A general psychophysiological interaction (gPPI) approach was used to test for task-specific modulations of connectivity. We used the standard method for PPI analysis (O'Reilly et al., 2012) but extended it to use the whole brain set of ROIs. In MATLAB, regressors were constructed for the HRF-convolved psychological task (e.g. encoding), the seed timeseries for each ROI (the physiological term), and the interaction of the convolved task (*psych*) and the ROI timeseries (*phys*). We extended this approach to a gPPI (McLaren et al., 2012) by including regressors for the other psychological task (retrieval) and its interaction with the seed. This method has been shown to improve specificity and sensitivity in PPI modeling. This model was then regressed against each of the remaining 179 ROI timeseries. The resultant t-statistics for the encoding and retrieval interactions were stored in 180x180 task PPI matrices. This is highly similar to the cPPI method described by Fornito and colleagues (Fornito et al., 2012). The residuals of each PPI model were stored and used in order to calculate the "pseudo resting state" correlations between each pair of regions after controlling for the effect of task (i.e. task controlled) (Fair et al., 2007).

The 180x180 PPI matrices were treated as graphs and analyzed with the Brain Connectivity Toolbox (BCT; https://sites.google.com/site/bctnet/). Networks were first assessed in the conventional fashion, thresholding to keep the top 10% strongest edges and then binarizing the edges to form an adjacency matrix. These networks were assessed for global efficiency (E_{glob}), which is calculated in two parts. First, the path length of the shortest path

between any two nodes in the network is stored in a distance matrix. E_{glob} is the grand mean of the inverse distance matrix, with longer distances indicating less efficiency. Mean clustering coefficient (MCC) was also calculated. For any given node, the clustering coefficient is the ratio of triangles to unconnected triples involving the node. The MCC is simply the mean across all nodes. Specific formulas for these measures are located elsewhere (Rubinov and Sporns, 2010). Next, unthresholded networks were assessed for modularity, regional strength, and regional participation. Specifically, modules were determined using unthresholded PPI connectivity matrices with positive and negative weights, using the formula and software described in (Rubinov and Sporns, 2011). This method respects the true character and full distribution of functional connectivity strengths and does not require the application of any artificial threshold or binarization. Each node was assigned to exactly one functional module using the Louvain method and function in the BCT (Blondel et al., 2008). Because this method is heuristic and may lead to slightly different partitions on different runs, we devised a strategy to obtain the most representative partition. For each network, 100 runs of the modularity assessment were performed. The similarity of each of these community assignments to every other was assessed using the normalized mutual information (Meilă, 2007), which assesses the joint probability of nodes occurring within the same module in different partitions. This similarity matrix was subjected to “meta-module” detection using the Louvain algorithm in order to find the different subsets of partitions. Each subset was ranked using the formula:

mean(*Q*)+size(subset) / std(*Q*)

The rationale was to select the subset that occurred most frequently, scaling that measure by the goodness of the partitions (the average *Q*) and the variability of that goodness (the standard deviation of *Q*). Once a subset had been selected, the partition with the maximum *Q* value within that subset was selected as optimal.

Group-level networks were determined using a modularity consistency method described by Fornito and colleagues (Fornito et al., 2012). Each pair of ROIs was assessed for

the frequency with which they appeared in the same module across subjects. The sum of these co-ocurrences for each pair of ROIs was stored in a 180x180 consistency matrix *G*. *G* was then analyzed for meta-module detection, using the same method described above. The modules in this meta-network describe the consistency with which ROIs are paired together in the functional network across subjects. It is a common way to obtain a group-level description of functional subnetworks and their interactions, either during rest or during a task (Van den Heuvel et al., 2008).

Results

Medial temporal lobe high resolution functional activity

Medial temporal lobe activity was first assessed during memory encoding. The encoding portion was emphasized because of our previous findings that hippocampal subregion activity varies in APOE-4 carriers (Suthana et al., 2010). Activity was measured for the encoding blocks vs. the baseline in the left and right CA1, CA2/3/DG, ERC, PHC, PRC, and SUB. When all subjects were combined, significant mean activity ($p < .01$) was observed in the bilateral anterior CA1, bilateral anterior CA2/3/DG, left ERC, bilateral PRC, and left anterior SUB. This indicated a significant engagement of the hippocampus in the service of encoding, primarily in its anterior subregions as has been shown to be a general trend for encoding (Kühn and Gallinat, 2013).

Next, a statistical model was constructed to test for the effect of APOE-4 status on MTL encoding activity. The 7 factor demographic model included continuous variables for age and years of education, categorical variables for APOE, gender, and family history of dementia, and interactions for APOE x age and APOE x gender. The only significant main effect of APOE was on activity in the left ERC ($t=-2.26$, $p=.03$) and right ERC ($t=-2.41$, $p=.02$), which also demonstrated a significant APOE x age interactions (left ERC $t=-2.24$, $p=.03$) (right ERC $t=2.43$, $p=.02$) The effect resulted from greater activity in APOE-4 non-carriers than carriers. The interaction was driven by a reduction of activity with age in carriers (left: $r=-.44$, right: $r=-.43$)

with respect to carriers (left: r=.16, right r=.13). This agreed with previous reports of memory-related decreases in hippocampal activation in non-carriers, a pattern not observed in carriers (Nichols et al., 2012).

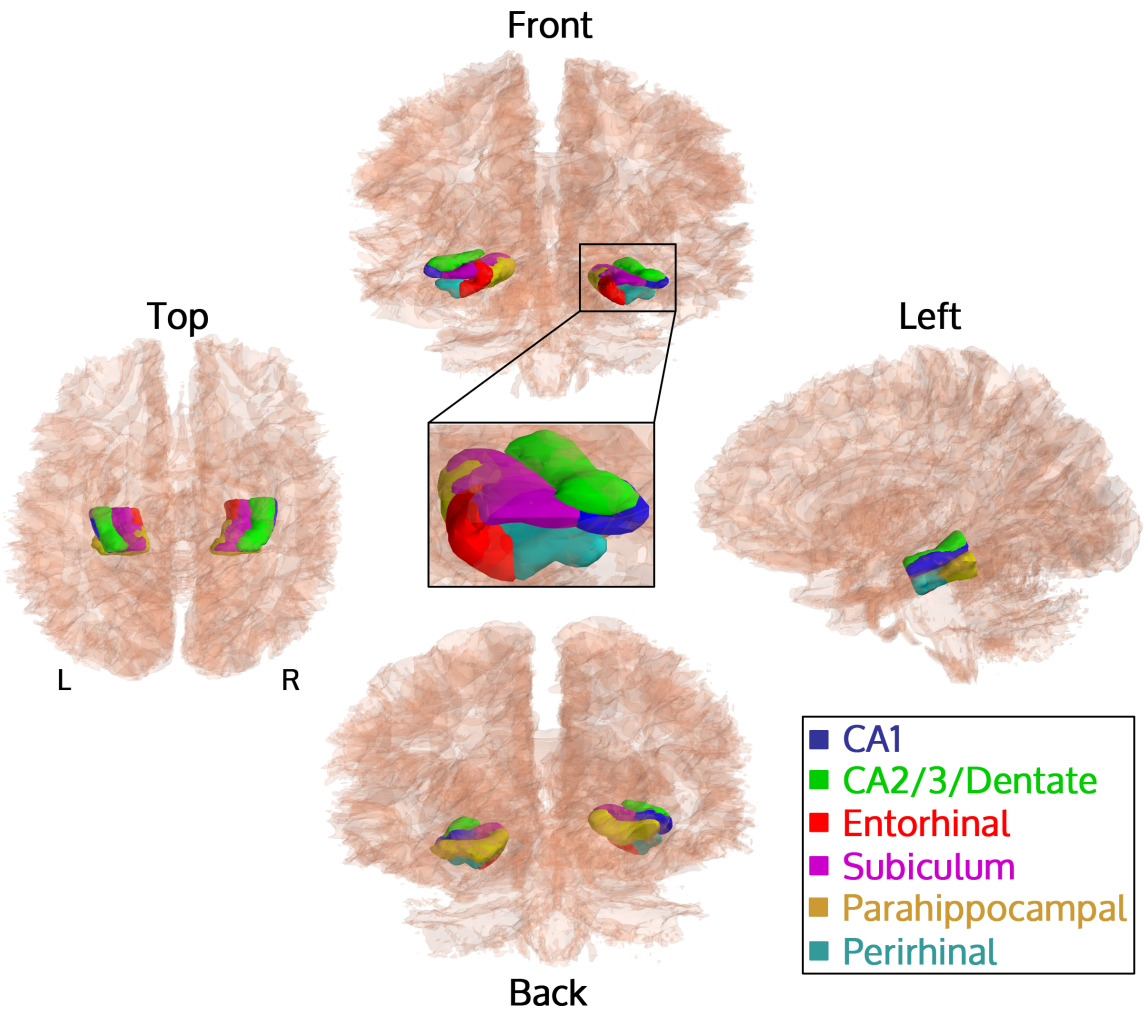

Figure 1: Medial temporal lobe regions of interest (ROIs) for one subject, registered to the whole brain structural scan. Left and right hemisphere hand-traced ROIs are shown simultaneously. Center box shows zoomed front view of left medial temporal lobe structures. Regional identities are color-coded and specified in the legend.

Whole brain functional activity

The same model was used to test for differences between APOE-4 carriers and non-carriers in whole brain activity during the encoding task. A significant activation cluster was found in the left MTL, with peak voxels at (-20, -30, -22) (Z=2.87) and (-24, -30, -14) (Z=2.97)

(**Figure 2**). According to the Juelich Histological Atlas included in FSL View, the maximum probability regions for these voxels were the left entorhinal cortex and left subiculum, respectively. For subsequent analyses of ERC encoding activity, the parameter estimates for the encoding vs. baseline contrast were extracted from the peak voxel in the ERC (-20, -30, -22).

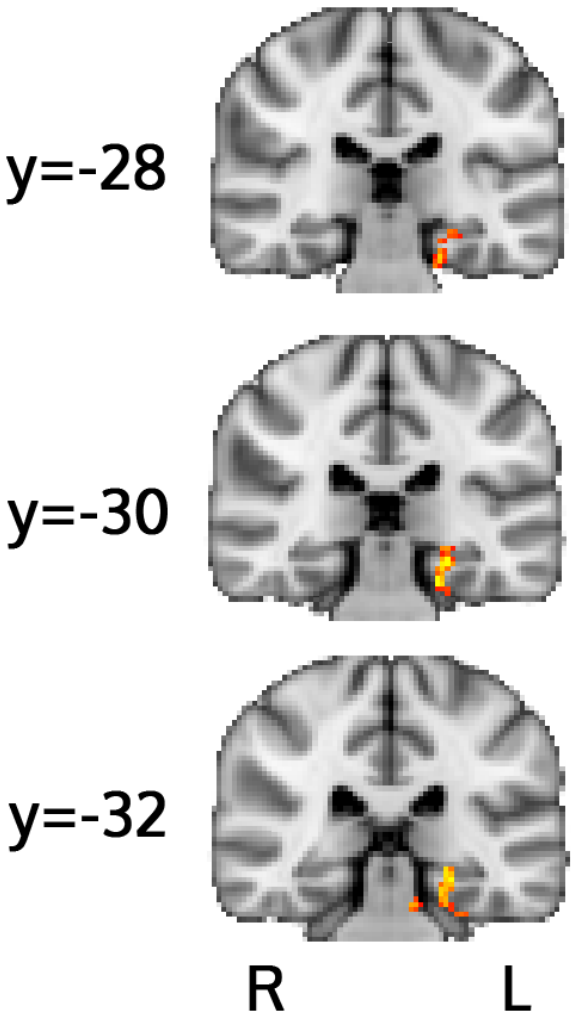

Figure 2: Whole brain functional activation during the encoding task. APOE-4 carriers demonstrated significantly lower activity in left MTL subregions including the entorhinal cortex and subiculum.

Whole brain functional network topology

We next investigated how whole brain networks reconfigured during the different phases of the episodic memory task. During encoding, the group-level consistency matrix contained three different modules (**Figure 3A**). The first encoding module (module 1) was a sensory motor network incorporating the pre/post-central gyrus and dorsal anterior cingulate. Module 2 included regions from the fronto-parietal external attention system and the posterior/ventral DMN.

Module 3 contained regions from the medial and lateral temporal lobe, occipital cortex, posterior cingulate, and ventral/medial prefrontal cortex. With respect to canonical intrinsic connectivity networks, the most novel aspect of this configuration was the coupling of visual areas with the MTL/posterior cingulate.

The task-controlled group network also contained four modules, largely consistent in both membership and topological organization with known functional networks detected during rsfMRI (Power et al., 2011). They included module 1, the sensory-motor network; module 2, a default mode/external awareness network; module 3, a primary/higher order visual network; and module 4, containing inferior, anterior, and medial temporal lobe, and ventral/medial prefrontal areas (the "anterior" DMN) (**Figure 3B)**. The main differences in module membership between the encoding and rest networks involved switching of the medial temporal lobe and subcomponents of the default mode network. The encoding network had lower mean clustering coefficient (.42 vs. .67), lower modularity (.38 vs. .62), greater global efficiency (.57 vs. .52), and longer average Euclidean distance between connected nodes (56.9mm vs. 52.7mm), all indicative of greater global integration.

Whole brain global network properties

Individual subject PPI networks were next compared for potential individual variability that may be determined by APOE status, age, or other demographic factors. Three global network properties were assessed from encoding and task-controlled networks: global efficiency

(E_{glob}), mean clustering coefficient (MCC), and the modularity (*Q*). E_{glob} and MCC were based on networks thresholded to keep the strongest 10% of edges, while the *Q* was calculated on unthresholded networks that included positive and negative weights. Thresholding was performed because E_{glob} and MCC are only meaningful in a network that is sparsely connected. Each subject's network was fully connected at 10% density. *Q* is calculated on a fully connected network. Each of these measures were tested against the 7 factor demographic model. For encoding networks, E_{glob} was significantly lower for APOE-4 carriers (p=.006), decreased with age (p=.003), and demonstrated an APOE x age interaction (p=.004). The interaction was a more negative correlation of age and E_{glob} for non-carriers, mirroring the trend observed in the HHR fMRI results. MCC was marginally lower in APOE-4 carriers (p=.049). *Q* did not demonstrate an APOE or age effect but was significantly lower for individuals with a family history of dementia (p=.01). For task-controlled networks, E_{glob} was significantly lower with age and was insignificant but trended to be lower in APOE-4 carriers (p=.052) and to have an APOE x age interaction (p=.06).

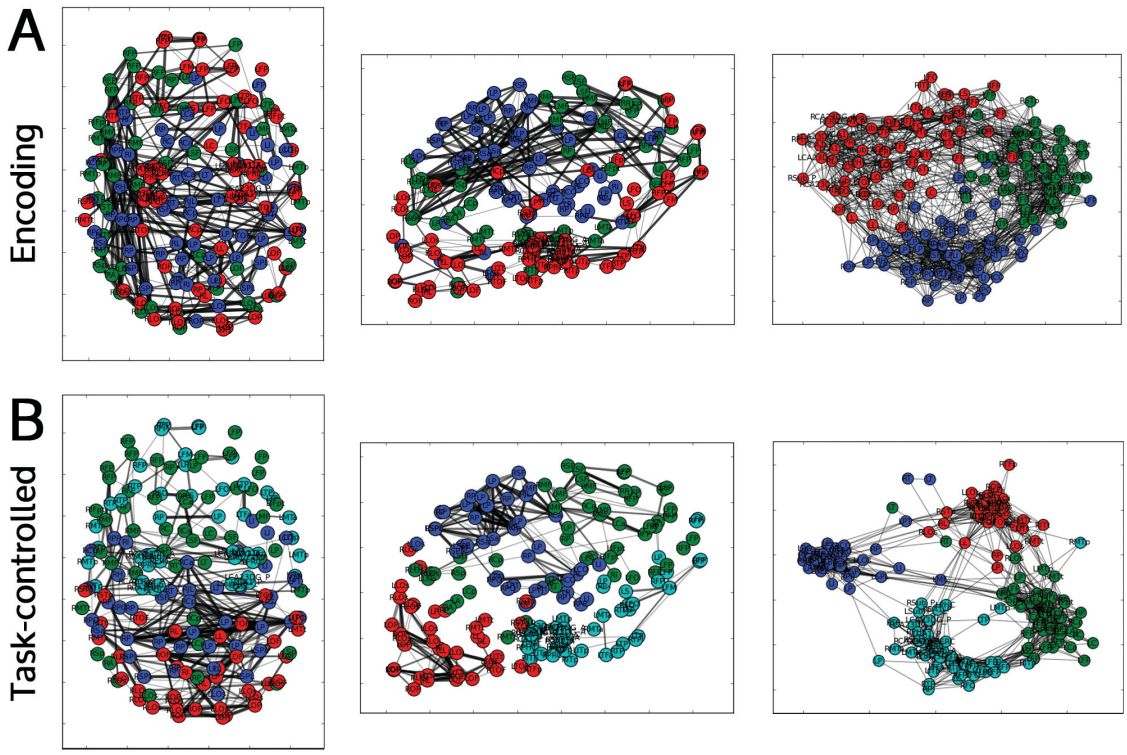

Figure 3: The functional modularity of the whole brain network during A) memory encoding (top row) and B) after statistically removing the effects of task (bottom row). The first column displays the top view with the back of the brain at the bottom. The second column shows a side view with the back of the brain on the left. The third column shows a spring-embedded plot displayed in 2D-space. Networks are at the group level and have been thresholded to display only strongest 2/12% of connections for top/side and spring-embedded, respecitvely. Regional abbreviations are defined by the Harvard Oxford cortical and subcortical atlases, except for the 18 MTL ROIs which are defined in the text.

Relationship of MTL activity and whole brain connectivity

We next sought to determine potential sources of differential activity in the left ERC. We hypothesized that task-specific whole brain network properties may best explain the variation of the MTL subregion activity across genotype and age. Specifically, we expected that modularity-based properties would be critical, given the highly distinct reconfigurations apparent at the group level. First, we tested the relationship of each global network measure to the left ERC encoding activity. *Q* had a significant negative relationship with ERC activity (r=-.48, p=.001; **Figure 4A**). When controlling for age, this affect remained (r=-.5). Neither of the other global

measures had any positive or negative relationship. As a test of the specificity of this finding, *Q* was correlated with a randomly selected voxel in the right postcentral gyrus. The activity of the voxel at (52, -14, 52) had a non-significant correlation with *Q* (r=-.15, p=.35). Thus, greater functional modularity during encoding occurred in tandem with lower entorhinal activity. In order to confirm that this relationship was specific to encoding, we tested the pseudo resting state (i.e. task-controlled) global network properties against ERC activity and did not find any significant relationships.

With the knowledge that modularity was the property that best predicted ERC activity, we probed nodal network measures that may specifically related to ERC activity. We focused on one basic property, connection strength, and two properties related to modularity, the participation coefficient and within/between module Z-scores. In all cases, we ran two separate tests, one for positive connections and one for negative connections. We limited the analysis to nodes within encoding module 1, containing the MTL and occipital cortex. For positive strength, the left lateral inferior occipital cortex was significantly predictive of ERC activity (r=.53; this and all subsequent results survived false discovery rate correction for multiple comparisons; **Figure 4B**). For negative strength, the left lateral inferior occipital cortex (r=-.55), left lateral superior occipital cortex (r=-.44), and left parahippocampal cortex (r=-.55) all had negative correlations with ERC activity. For positive between module Z-score, the right lateral inferior occipital cortex (r=.48) and right temporal pole (r=-.47) predicted ERC activity in opposite directions. For negative between module Z-score, the left putamen (r=.5), left orbitofrontal cortex (r=.52), left temporal pole (r=.5), and right temporal pole (r=.5) all positively related to ERC activity, while left lateral superior occipital cortex (r=-.37) and left lateral inferior occipital cortex (r=-.44) negatively correlated. The overall pattern that emerged was a positive relationship of the ERC to medial temporal and occipital regions (**Figure 5B**) and a reciprocal relationship with anterior temporal and ventral prefrontal areas (**Figure 5C**).

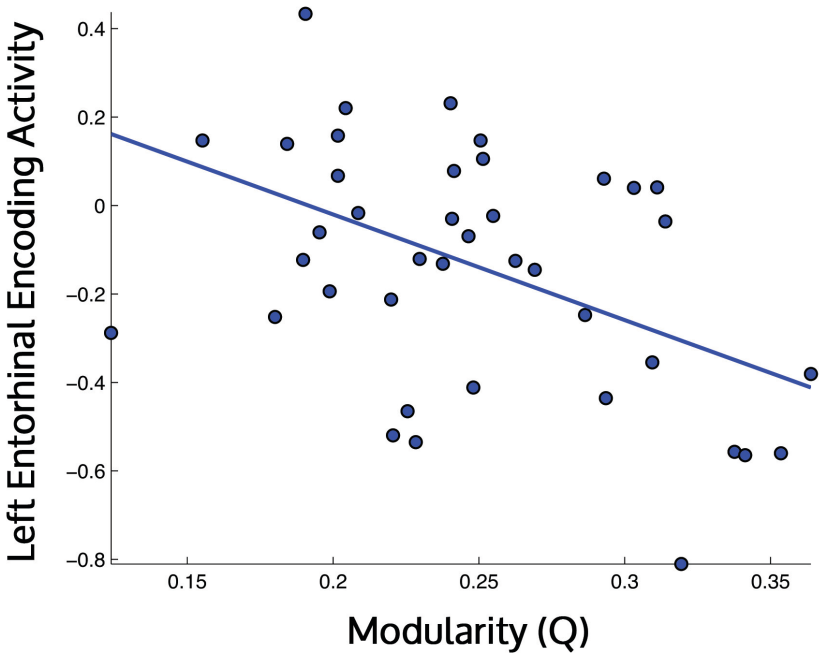

Figure 4: The correlation of modularity (*Q*) and left entorhinal cortex (ERC) activity in the whole brain fMRI scan during memory encoding (r=-.48, p=.001). *Q* is a measure of the separability of the network into subsets of nodes that are densely interconnected with one another and sparsely connected to the rest of the network, and ranges between 0 and 1. ERC activity is the parameter estimate from the associative memory encoding vs. baseline contrast (units are arbitrary).

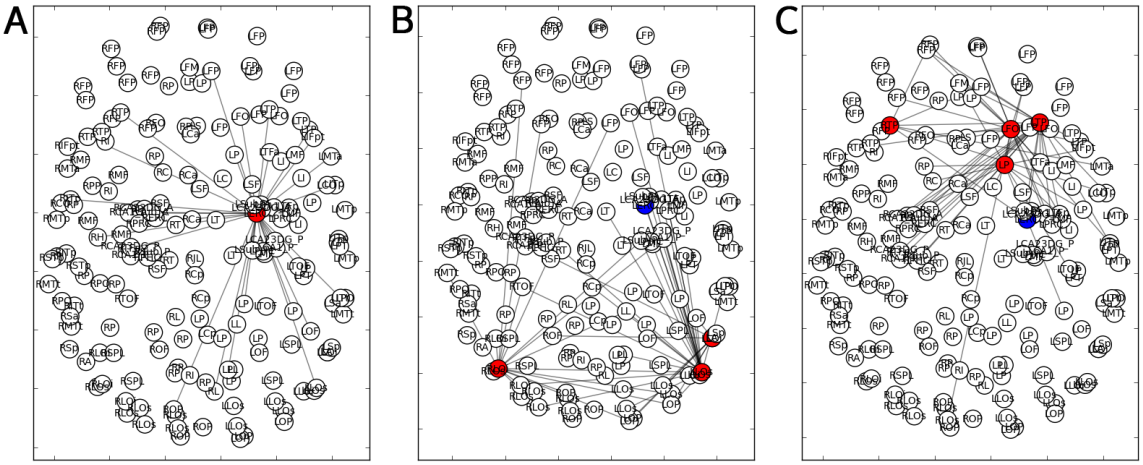

Figure 5: The functional connectivity patterns of specific regions of interest during memory encoding. The left side of each image corresponds to the right side of the brain. A) shows the top 15% of connections from the left entorhinal cortex. B) shows the top 10% of connections from the left lateral inferior/superior occipital cortices and right lateral inferior occipital cortex. C) shows the top 7% of connections from the left/right temporal poles, the left frontal orbital cortex, and the left putamen. All of the regions in B) and C) had specific network properties that were highly predictive of left ERC encoding activity.

Entorhinal cortex thickness

Left entorhinal cortex thickness measurements were also evaluated using the 7 factor demographic model. In this subject pool, no significant differences were apparent. The only trend was for a reduction in thickness with age (p=.07).

Discussion

The entorhinal cortex is a locus of early abnormality in the course Alzheimer's disease. Here we examined ERC activity in individuals at genetic risk for AD and detected consistent reductions in functional activity during memory encoding that were dependent on APOE-4 genotype and exacerbated by age. A task-based network analysis revealed that the ERC adaptively coupled with visual regions in the service of memory encoding. Within this "visual memory" module, reduced connectivity of specific higher-order visual regions occurred in tandem with lower ERC activity. In a module containing ventral and medial prefrontal and anterior temporal areas, greater extra-modular connectivity was highly related to lower ERC activity. At the global level, higher ERC activity occurred in the presence of less distinct functional modules.

Layer II of the ERC is one of the first brain regions where neurofibrillary changes appear in the earliest stages of Alzheimer's Disease (Braak and Braak, 1991) (Gómez-Isla et al., 1996). In aging individuals at genetic risk for AD, based on possession of at least one APOE-4 allele, ERC demonstrates reductions in cortical thickness that are predictive of subsequent decline in memory encoding (Burggren et al., 2011), indicating that structural alterations in this region have specific functional consequences. Previous studies of entorhinal and hippocampal functional activity during memory encoding in APOE-4 carriers have reported varied results (Bookheimer et al., 2000) (Dickerson et al., 2005) (Suthana et al., 2010) (Filippini et al., 2011) (Adamson et al., 2011). A multitude of factors have affected the variable findings in the

literature. The nature of the encoding task - whether it involves single items or associations, and whether these stimuli are verbal, pictorial, or spatial – will influence which hippocampal subregions are engaged, and which hemisphere is predominantly involved. Evidence that extrahippocampal MTL areas are engaged in the association of items (Kirwan and Stark, 2004) supports the use of the associative memory task in this study. The delineation of hippocampal subregions is also variable, based on either an anatomical atlas, an automated parcellation program on a whole brain structural scan, or hand drawing ROIs on whole brain or high resolution structural scans. The use of high resolution scans to create customized, subject specific ROIs assured high anatomical specificity in the current study. Furthermore, the confirmation of decreased entorhinal encoding activity in APOE-4 carriers in two independent runs of the same task, using whole brain and high-resolution MTL fMRI sequences with different parameters, supports the consistency of this finding. Finally, studies of APOE's affect on MTL memory encoding activity have been influenced by the varying composition of the subject pools. The choice to study only cognitively normal individuals, to expand that pool to non-demented individuals, and how to stratify individuals by APOE status (including hetero/homozygotes and possession of an APOE-2 allele; see (Trachtenberg et al., 2012)) and age (limiting the age range, looking at age correlations or APOE x age interactions (Brown et al., 2011)), will all naturally affect the outcome. We chose to use a large age range and a model that included terms for APOE, age, and APOE x age interaction. This enabled the detection of lower APOE-4 specific activity in ERC, and in addition, an interactive effect of APOE status and age in line with previous reports (Nichols et al., 2012). Such a design requires the inclusion of older subjects and is thus very difficult to only include cognitively normal individuals. Furthermore, it may be argued that cognitively normal individuals in there mid-70s are atypical in their cognitive resilience.

In order to understand how ERC activity differences related to broader brain states, it was critical to 1) have subjects perform a task that would engage the areas of earliest potential

compromise, 2) adapt a method that assesses functional connectivity in a task setting *over and above* task co-activity, 3) use whole-brain complex network analysis to detect downstream connectivity differences that track with alterations at the disease locus (Zhou et al., 2012). The use of the PPI method with a set of whole brain ROIs, including subject-specific MTL subregions, allowed us to evaluate a basic functional property of interest, ERC activity, in the context of task-specific network reconfigurations at the whole brain level.

We observed adaptive coupling of the MTL and occipital cortex into a coherent module during memory encoding in this study, in line with previous reports of task-driven modulations of visual functional connectivity (Chadick and Gazzaley, 2011). Effortful memory encoding also elicited a global reduction in modularity and an increase in global efficiency, indicative of a more globally integrated network. Similar affects have been observed in working memory tasks (Kitzbichler et al., 2011). However, this is to our knowledge the first direct linkage between global complex network properties during a task and the degree of activation. At a regional level, we focused on nodes within module 1 because of its inclusion of the MTL, our primary region of interest. The network-wide connectivity strengths of lateral occipital and parahippocampal areas were most positively related to ERC activity. It should be specified that our interpretation of positive vs. negative functional connections is that a positive correlation between positive functional connectivity and ERC activity is equivalent to a negative correlation of negative functional connectivity and ERC activity. While the interpretation of negative functional connectivity remains controversial, it does appear to have physiological origin and relevance (Chang and Glover, 2009) and to relate specifically to the degree of functional activity (Gee et al., 2013). Regions whose between-module functional connectivity negatively related to ERC activity included the bilateral temporal poles, left orbitofrontal cortex, and putamen. These areas bear correspondence to the salience network (Seeley et al., 2007), which has been shown to exhibit enhanced connectivity in the face of decreased default mode connectivity in APOE (Machulda MM, 2011) and AD (Zhou et al., 2010). One potential mechanism is that

increased intermodular connectivity of this network inhibits DMN connectivity and subsequently reduces ERC activity.

Here we report that non-demented aging APOE-4 carriers exhibit consistent reduced activity during associative episodic memory encoding in the left entorhinal cortex. Assessment of the whole brain task-specific encoding network revealed decreased modularity and increased global integration with respect to task-controlled pseudo resting state networks. Critically, greater reductions in modularity co-occurred in individuals with higher ERC activity. Posterior regions in the lateral occipital and medial temporal lobes had a positive influence on ERC activity, while anterior regions in the temporal lobe and ventral prefrontal cortex had a negative influence. This work helps contextualize MTL activity alterations, a promising potential biomarker for AD risk, and emphasizes the importance of exploring task-driven alterations of functional connectivity networks in relevant cognitive domains.

Chapter 3 References

Adamson, M.M., Hutchinson, J.B., Shelton, A., Wagner, A.D., Taylor, J.L., 2011. Reduced hippocampal activity during encoding in cognitively normal adults carrying the APOE ?4 allele. Neuropsychologia 49, 2448–2455.

Andrews-Hanna, J.R., Reidler, J.S., Sepulcre, J., Poulin, R., Buckner, R.L., 2010. Functional-anatomic fractionation of the brain's default network. Neuron 65, 550–562.

Bassett, D.S., Wymbs, N.F., Porter, M.A., Mucha, P.J., Carlson, J.M., Grafton, S.T., 2011. Dynamic reconfiguration of human brain networks during learning. Proc. Natl. Acad. Sci. U.S.A. 108, 7641–7646.

Blondel, V.D., Guillaume, J.-L., Lambiotte, R., Lefebvre, E., 2008. Fast unfolding of communities in large networks. Journal of Statistical Mechanics: Theory and Experiment 2008, P10008.

Bookheimer, S.Y., Strojwas, M.H., Cohen, M.S., Saunders, A.M., Pericak-Vance, M.A., Mazziotta, J.C., Small, G.W., 2000. Patterns of Brain Activation in People at Risk for Alzheimer's Disease. N Engl J Med 343, 450–456.

Braak, H., Braak, E., 1991. Neuropathological stageing of Alzheimer-related changes. Acta Neuropathol. 82, 239–259.

Brown, J.A., Rudie, J.D., Bandrowski, A., Horn, J.D.V., Bookheimer, S.Y., 2012. The UCLA multimodal connectivity database: a web-based platform for brain connectivity matrix sharing and analysis. Front. Neuroinform 6, 28.

Brown, J.A., Terashima, K.H., Burggren, A.C., Ercoli, L.M., Miller, K.J., Small, G.W., Bookheimer, S.Y., 2011. Brain network local interconnectivity loss in aging APOE-4 allele carriers. Proc. Natl. Acad. Sci. U.S.A. 108, 20760–20765.

Buckner, R.L., Sepulcre, J., Talukdar, T., Krienen, F.M., Liu, H., Hedden, T., Andrews-Hanna, J.R., Sperling, R.A., Johnson, K.A., 2009. Cortical Hubs Revealed by Intrinsic Functional Connectivity: Mapping, Assessment of Stability, and Relation to Alzheimer's Disease. J. Neurosci. 29, 1860–1873.

Burggren, A.C., Renner, B., Jones, M., Donix, M., Suthana, N.A., Martin-Harris, L., Ercoli, L.M., Miller, K.J., Siddarth, P., Small, G.W., Bookheimer, S.Y., 2011. Thickness in entorhinal and subicular cortex predicts episodic memory decline in mild cognitive impairment. Int J Alzheimers Dis 2011, 956053.

Burggren, A.C., Zeineh, M.M., Ekstrom, A.D., Braskie, M.N., Thompson, P.M., Small, G.W., Bookheimer, S.Y., 2008. Reduced cortical thickness in hippocampal subregions among cognitively normal apolipoprotein E e4 carriers. Neuroimage 41, 1177–83.

Chadick, J.Z., Gazzaley, A., 2011. Differential coupling of visual cortex with default or frontal-parietal network based on goals. Nat Neurosci 14, 830–832.

Chang, C., Glover, G.H., 2009. Effects of model-based physiological noise correction on default mode network anti-correlations and correlations. NeuroImage 47, 1448–1459.

Corder, E.H., Saunders, A.M., Strittmatter, W.J., Schmechel, D.E., Gaskell, P.C., Small, G.W., Roses, A.D., Haines, J.L., Pericak-Vance, M.A., 1993. Gene dose of apolipoprotein E type 4 allele and the risk of Alzheimer's disease in late onset families. Science 261, 921–3.

Damoiseaux, J.S., Prater, K.E., Miller, B.L., Greicius, M.D., 2012a. Functional connectivity tracks clinical deterioration in Alzheimer's disease. Neurobiology of Aging 33, 828.e19–828.e30.

Damoiseaux, J.S., Seeley, W.W., Zhou, J., Shirer, W.R., Coppola, G., Karydas, A., Rosen, H.J., Miller, B.L., Kramer, J.H., Greicius, M.D., 2012b. Gender Modulates the APOE ε4 Effect in Healthy Older Adults: Convergent Evidence from Functional Brain Connectivity and Spinal Fluid Tau Levels. J. Neurosci. 32, 8254–8262.

De Calignon, A., Polydoro, M., Suárez-Calvet, M., William, C., Adamowicz, D.H., Kopeikina, K.J., Pitstick, R., Sahara, N., Ashe, K.H., Carlson, G.A., Spires-Jones, T.L., Hyman, B.T., 2012. Propagation of Tau Pathology in a Model of Early Alzheimer's Disease. Neuron 73, 685–697.

DeCarli, C., Frisoni, G.B., Clark, C.M., Harvey, D., Grundman, M., Petersen, R.C., Thal, L.J., Jin, S., Jack, C.R., Jr, Scheltens, P., 2007. Qualitative estimates of medial temporal atrophy as a predictor of progression from mild cognitive impairment to dementia. Arch. Neurol. 64, 108–115.

Desikan, R.S., Cabral, H.J., Hess, C.P., Dillon, W.P., Glastonbury, C.M., Weiner, M.W., Schmansky, N.J., Greve, D.N., Salat, D.H., Buckner, R.L., Fischl, B., 2009. Automated MRI measures identify individuals with mild cognitive impairment and Alzheimer's disease. Brain 132, 2048–2057.

Devanand, D.P., Pradhaban, G., Liu, X., Khandji, A., De Santi, S., Segal, S., Rusinek, H., Pelton, G.H., Honig, L.S., Mayeux, R., Stern, Y., Tabert, M.H., De Leon, M.J., 2007. Hippocampal and entorhinal atrophy in mild cognitive impairment: prediction of Alzheimer disease. Neurology 68, 828–836.

Dickerson, B.C., Salat, D.H., Greve, D.N., Chua, E.F., Rand-Giovannetti, E., Rentz, D.M., Bertram, L., Mullin, K., Tanzi, R.E., Blacker, D., Albert, M.S., Sperling, R.A., 2005. Increased hippocampal activation in mild cognitive impairment compared to normal aging and AD. Neurology 65, 404–411.

Ekman, M., Derrfuss, J., Tittgemeyer, M., Fiebach, C.J., 2012. Predicting errors from reconfiguration patterns in human brain networks. PNAS 109, 16714–16719.

Fair, D.A., Schlaggar, B.L., Cohen, A.L., Miezin, F.M., Dosenbach, N.U.F., Wenger, K.K., Fox, M.D., Snyder, A.Z., Raichle, M.E., Petersen, S.E., 2007. A method for using blocked and event-related fMRI data to study "resting state" functional connectivity. NeuroImage 35, 396–405.

Filippini, N., Ebmeier, K.P., Macintosh, B.J., Trachtenberg, A.J., Frisoni, G.B., Wilcock, G.K., Beckmann, C.F., Smith, S.M., Matthews, P.M., Mackay, C.E., 2011. Differential effects of the APOE genotype on brain function across the lifespan. Neuroimage 54, 602–610.

Filippini, N., MacIntosh, B.J., Hough, M.G., Goodwin, G.M., Frisoni, G.B., Smith, S.M., Matthews, P.M., Beckmann, C.F., Mackay, C.E., 2009. Distinct patterns of brain activity in young carriers of the APOE-ε4 allele. Proceedings of the National Academy of Sciences 106, 7209 –7214.

Fornito, A., Harrison, B.J., Zalesky, A., Simons, J.S., 2012. Competitive and cooperative dynamics of large-scale brain functional networks supporting recollection. PNAS 109, 12788–12793.

Gee, D.G., Humphreys, K.L., Flannery, J., Goff, B., Telzer, E.H., Shapiro, M., Hare, T.A., Bookheimer, S.Y., Tottenham, N., 2013. A Developmental Shift from Positive to Negative Connectivity in Human Amygdala–Prefrontal Circuitry. J. Neurosci. 33, 4584–4593.

Gómez-Isla, T., Price, J.L., McKeel, D.W., Jr, Morris, J.C., Growdon, J.H., Hyman, B.T., 1996. Profound loss of layer II entorhinal cortex neurons occurs in very mild Alzheimer's disease. J. Neurosci. 16, 4491–4500.

Greicius, M.D., Srivastava, G., Reiss, A.L., Menon, V., 2004. Default-mode network activity distinguishes Alzheimer's disease from healthy aging: Evidence from functional MRI. Proceedings of the National Academy of Sciences of the United States of America 101, 4637–4642.

Kim, H., Daselaar, S.M., Cabeza, R., 2010. Overlapping brain activity between episodic memory encoding and retrieval: Roles of the task-positive and task-negative networks. NeuroImage 49, 1045–1054.

Kirwan, C.B., Stark, C.E., 2004. Medial temporal lobe activation during encoding and retrieval of novel face-name pairs. Hippocampus 14, 919–930.
Kitzbichler, M.G., Henson, R.N.A., Smith, M.L., Nathan, P.J., Bullmore, E.T., 2011. Cognitive Effort Drives Workspace Configuration of Human Brain Functional Networks. The Journal of Neuroscience 31, 8259 –8270.
Kühn, S., Gallinat, J., 2013. Segregating cognitive functions within hippocampal formation: A quantitative meta-analysis on spatial navigation and episodic memory. Human Brain Mapping n/a–n/a.
Machulda MM, J.D., 2011. EFfect of apoe ε4 status on intrinsic network connectivity in cognitively normal elderly subjects. Arch Neurol 68, 1131–1136.
McLaren, D.G., Ries, M.L., Xu, G., Johnson, S.C., 2012. A generalized form of context-dependent psychophysiological interactions (gPPI): A comparison to standard approaches. NeuroImage 61, 1277–1286.
Meilă, M., 2007. Comparing clusterings—an information based distance. Journal of Multivariate Analysis 98, 873–895.
Nichols, L.M., Masdeu, J.C., Mattay, V.S., Kohn, P., Emery, M., Sambataro, F., Kolachana, B., Elvevåg, B., Kippenhan, S., Weinberger, D.R., Berman, K.F., 2012. Interactive effect of apolipoprotein e genotype and age on hippocampal activation during memory processing in healthy adults. Arch. Gen. Psychiatry 69, 804–813.
O'Reilly, J.X., Woolrich, M.W., Behrens, T.E.J., Smith, S.M., Johansen-Berg, H., 2012. Tools of the trade: psychophysiological interactions and functional connectivity. Soc Cogn Affect Neurosci 7, 604–609.
Power, J.D., Cohen, A.L., Nelson, S.M., Wig, G.S., Barnes, K.A., Church, J.A., Vogel, A.C., Laumann, T.O., Miezin, F.M., Schlaggar, B.L., Petersen, S.E., 2011. Functional Network Organization of the Human Brain. Neuron 72, 665–678.
Rubinov, M., Sporns, O., 2010. Complex network measures of brain connectivity: uses and interpretations. Neuroimage 52, 1059–1069.
Rubinov, M., Sporns, O., 2011. Weight-conserving characterization of complex functional brain networks. Neuroimage.
Salat, D.H., Tuch, D.S., Van der Kouwe, A.J.W., Greve, D.N., Pappu, V., Lee, S.Y., Hevelone, N.D., Zaleta, A.K., Growdon, J.H., Corkin, S., Fischl, B., Rosas, H.D., 2010. White matter pathology isolates the hippocampal formation in Alzheimer's disease. Neurobiol. Aging 31, 244–256.
Seeley, W.W., Menon, V., Schatzberg, A.F., Keller, J., Glover, G.H., Kenna, H., Reiss, A.L., Greicius, M.D., 2007. Dissociable intrinsic connectivity networks for salience processing and executive control. J. Neurosci 27, 2349–2356.
Sestieri, C., Corbetta, M., Romani, G.L., Shulman, G.L., 2011. Episodic Memory Retrieval, Parietal Cortex, and the Default Mode Network: Functional and Topographic Analyses. The Journal of Neuroscience 31, 4407 –4420.
Sheline, Y.I., Morris, J.C., Snyder, A.Z., Price, J.L., Yan, Z., D'Angelo, G., Liu, C., Dixit, S., Benzinger, T., Fagan, A., Goate, A., Mintun, M.A., 2010. APOE4 Allele Disrupts Resting State fMRI Connectivity in the Absence of Amyloid Plaques or Decreased CSF A{beta}42. J. Neurosci. 30, 17035–17040.
Squire, L.R., Stark, C.E.L., Clark, R.E., 2004. The Medial Temporal Lobe*. Annual Review of Neuroscience 27, 279–306.
Suthana, N.A., Krupa, A., Donix, M., Burggren, A., Ekstrom, A.D., Jones, M., Ercoli, L.M., Miller, K.J., Siddarth, P., Small, G.W., Bookheimer, S.Y., 2010. Reduced hippocampal CA2, CA3, and dentate gyrus activity in asymptomatic people at genetic risk for Alzheimer's disease. Neuroimage 53, 1077–1084.

Trachtenberg, A.J., Filippini, N., Cheeseman, J., Duff, E.P., Neville, M.J., Ebmeier, K.P., Karpe, F., Mackay, C.E., 2012. The effects of APOE on brain activity do not simply reflect the risk of Alzheimer's disease. Neurobiology of Aging 33, 618.e1–618.e13.

Van den Heuvel, M., Mandl, R., Hulshoff Pol, H., 2008. Normalized Cut Group Clustering of Resting-State fMRI Data. PLoS ONE 3, e2001.

Zeineh, M.M., Engel, S.A., Bookheimer, S.Y., 2000. Application of Cortical Unfolding Techniques to Functional MRI of the Human Hippocampal Region. NeuroImage 11, 668–683.

Zhou, J., Gennatas, E.D., Kramer, J.H., Miller, B.L., Seeley, W.W., 2012. Predicting Regional Neurodegeneration from the Healthy Brain Functional Connectome. Neuron 73, 1216–1227.

Zhou, J., Greicius, M.D., Gennatas, E.D., Growdon, M.E., Jang, J.Y., Rabinovici, G.D., Kramer, J.H., Weiner, M., Miller, B.L., Seeley, W.W., 2010. Divergent network connectivity changes in behavioural variant frontotemporal dementia and Alzheimer's disease. Brain 133, 1352–1367.

Chapter 4

Hippocampal-centered network increases memory consolidation-dependent functional connectivity via parahippocampal axonal pathways

Introduction

Hippocampal interaction with the cortex is required for the consolidation of declarative episodic memory (Frankland and Bontempi, 2005). Declarative memory traces that are initially stored primarily in the hippocampus become more cortically mediated over the timescale of hours to days. This process of transfer involves a dialogue between the hippocampus and specific cortical areas, both during quiescent periods after learning (Logothetis et al., 2012) (Tambini et al., 2010) and during sleep (Ji and Wilson, 2007).

The identity of the engaged cortical regions during these consolidation phases is dependent on the class of stimuli, the nature of the task (e.g. single-item vs. association), and the degree of initial encoding. It is well established that modality-specific cortical areas do demonstrate elevated functional connectivity with the hippocampus in idle periods following task, including the parahippocampal gyrus for scenes, the fusiform face area for faces (Tambini et al., 2010), the sensory cortex for textures, and the olfactory cortex for scents. In addition to these modality-specific reactivations, the medial prefrontal cortex (mPFC) is vital for the consolidation of such memories. fMRI studies in humans have demonstrated that persistent mPFC-hippocampal connectivity after a task persists and is related to the degree of recall (Kesteren et al., 2010). Rodent studies have revealed post-task replay of memory sequences in the prefrontal cortex during sleep (Euston et al., 2007). Evidence suggests that with time, episodes become less hippocampally dependent as the burden is shifted to the mPFC to orchestrate subsequent recall (Takashima et al., 2006) (Frankland and Bontempi, 2006) (Takashima et al., 2009).

While the functional connectivity of the hippocampal and cortical areas involved in episodic memory consolidation are well characterized, less is known about the axonal circuitry

that enables such information transfer. Sensory-specific hierarchies are known to converge in the parahippocampal and entorhinal cortices (Felleman and Van Essen, 1991), serving as a gateway into the hippocampus where subsequent binding, pattern separation, and pattern completion can occur. The primary outputs from the medial temporal lobe are the fornix, the cingulum bundle, and the uncinate fasciculus. The structural integrity of the fornix in particular has been linked to episodic memory ability (Metzler-Baddeley et al., 2012). Simultaneously, it is known that the MTL is a node in the ventral/posterior aspect of the default mode network, coupling most closely with the retrosplenial cortex, inferior parietal lobule, and ventromedial prefrontal cortex (Andrews-Hanna et al., 2010). However, it is not clear which structural pathway is predominantly responsible for hippocampal-medial prefrontal communication in service of memory consolidation in humans. Furthermore, how individual variability in this circuitry constrain the degree of functional connectivity or memory performance is unknown.

To better understand the effects of new memory encoding on functional connectivity, we assessed associative episodic memory encoding during a face/place association fMRI task. We evaluated changes in resting state functional connectivity before and after the task. We examined early consolidation interactions between the hippocampus, medial prefrontal cortex, and modality-specific brain regions with regard to free recall memory performance 24 hours later. The structural network topology of these areas was used to triangulate the episodic memory consolidation network and test for individual differences in functional and structural connectivity that predicted performance.

Results

Task performance

Following a 24 hour delay, On the free recall task, subjects recalled 5.6 +/- 5.5 items (range 0-19). On the cued recollection task, subjects recalled 7 +/- 4.9 items (range 0-16). On the cued recognition task, subjects recalled 26.5 +/- 9.4 items (range 11-40). While a floor effect

was observed for the free recall and cued recollection tasks, cued recollection performance indicated significant successful encoding. Therefore, subsequent analyses focus on the cued recognition performance unless otherwise specified.

fMRI encoding activity

Based on our a priori anatomical hypotheses, BOLD activity was assessed in the bilateral hippocampal area, using a mask combined from all regions in our group functional atlas (see Methods) whose center of mass had a maximal probability of being in the hippocampus or parahippocampal gyrus, based on the Harvard/Oxford probabilistic atlas. We contrasted activity for different event types, focusing on two conditions: cued-recognitions hits vs. misses during 1) stimulus presentation of the face/place association and 2) post-stimulus fixation on a point. Our inclusion of the post-stimulus period allowed for elaborative encoding of the items and allowed us to examine immediate post-stimulus effects that may relate to consolidation (Ben-Yakov and Dudai, 2011). Within the bilateral hippocampal ROI, in the post-stimulus hits > misses contrast, a cluster of 14 contiguous voxels with all $Z > 2.0$ ($p < .05$) was detected in the right hippocampus (**Figure 1**). Smaller clusters (< 10 voxels) were found in the left hippocampus and right extra-hippocampal area.

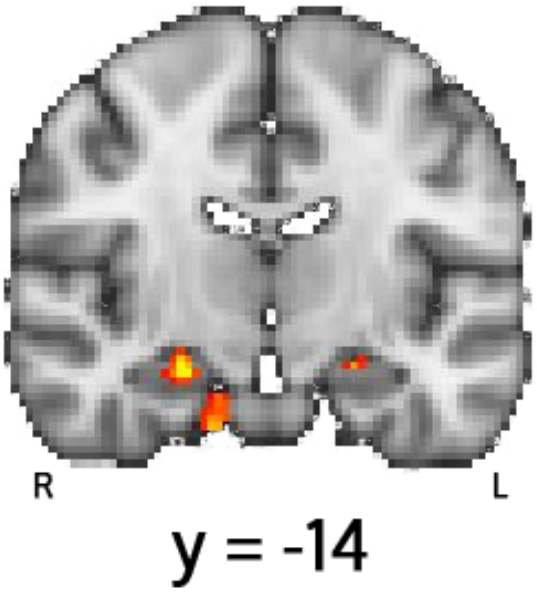

Figure 1: Functional activation map for cued recognition hits vs. misses. Whole brain data were masked with a bilateral hippocampal area masks. Unthresholded Z-statistic map is shown.

Hippocampal rsfMRI connectivity changes and memory performance

We next examined changes in idle functional connectivity between the pre-task and post-task rsfMRI scans. The *post – pre* correlations coefficient changes between the right hippocampus and the remaining 198 brain regions changed by an average of by an average of r=-.02 +/- .07 . When the connectivity change index was linearly correlated with cued recognition score, five regions displayed a correlation coefficient greater than r=.7 ($p < .005$): the left parietal operculum (r=.7, p=.004), left temporal occipital fusiform cortex (r=.69, p.004), right lingual gyrus (r=.74, p=.002), right superior temporal gyrus posteriorly (r=.71, p=.003), and the left frontal orbital cortex (r=.7, p=.004) (**Figure 2**)**.** Two of these regions were highly modality-specific, the left fusiform cortex and right lingual gyrus. This confirmed our hypothesis of post-task functional connectivity alterations being predictive of later performance. Additionally, the significant relationship between altered right hippocampal/orbitofrontal connectivity and

recognition score indicated a role for this connection in consolidation of the associations. This set of regions is henceforth identified as the recognition consolidation network (RCN).

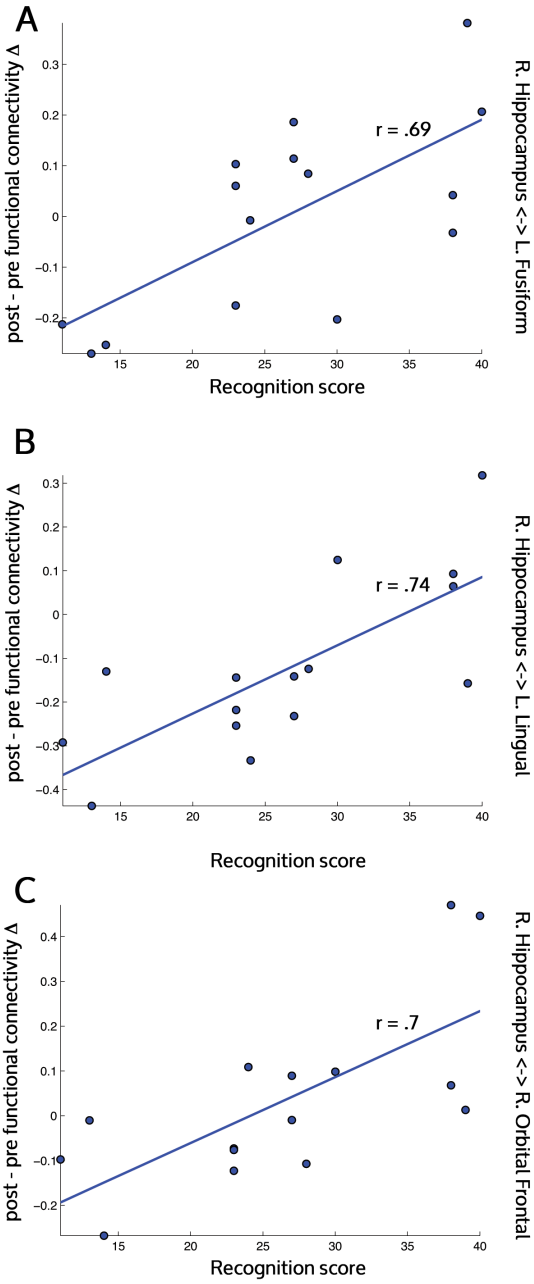

Figure 2: Functional connectivity change (FCΔ) between a post-task rsfMRI and pre-task rsfMRI. These measures were calculated for functional connections between the right hippocampus and other brain ROIs. The correlation of FCΔ and episodic memory cued recognition score on a test 24 hours later was calculated and was significantly positive for regions including the a) left fusiform gyrus, b) right lingual gyrus, and c) left orbital frontal cortex.

Structural connectivity of the recogniton consolidation network

The subset of regions with memory-specific functional connectivity alterations were next examined for their structural connectivity. The group-level structural connectivity matrix was used to determine the shortest path between the right hippocampus and each of the five RCN ROIs. This subnetwork (**Figure 3**) contained the right parahippocampal gyrus as a highly central hub.

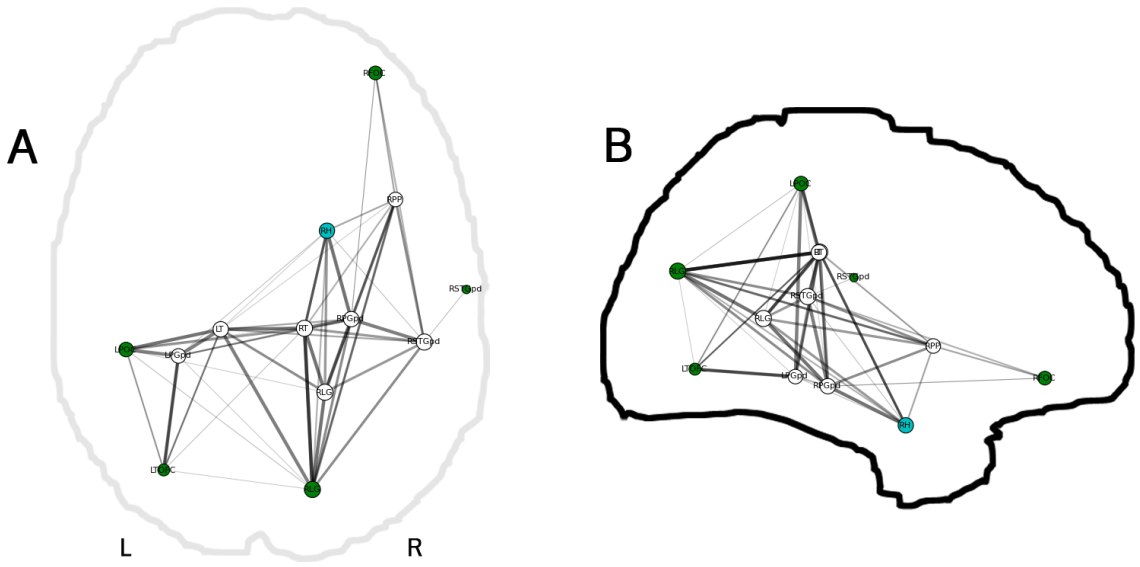

Figure 3: The structural subnetwork for the set of regions functionally involved in recognition consolidation. The hippocampus is shown in blue and the five remaining nodes in the network are shown in green. Also included are the intermediate nodes along structural shortest paths between the hippocampus and each of the other five nodes in the recognition consolidation network. Abbreviations (L=left, R=right): POC: parietal operculum, T: thalamus, STGpd: superior temporal gyrus posterior division, H: hippocampus, LG: lingual gyrus, TOFC: temporal occipital fusiform cortex, PGpd: parahippocampal gyrus posterior division, PP: planum polare, FOC: frontal orbital cortex.

Structural connectivity/behavior relationships

Finally we assessed what constraints individual variations in structural connection strength may place on memory performance. First, the direct connection strengths between each of the RCN ROIs were assessed. Only three of these pairs of these regions were directly connected in all subjects (parietal operculum/fusiform gyrus, parietal operculum/frontal orbital cortex, and orbital cortex/lingual gyrus). Using the fiber count as a measure of connection strength, these counts were correlated with recognition score but no significant relationships were found.

Next, the shortest path weights for the paths between the hippocampus and the 5 RCN ROIs were summed for each subject. Five "net path weight" measures were obtained per subject, where the net weight was simply the sum of fibers for each edge along a given path. These were net path weights were linearly correlated with recognition score but were not found to be significant ($r=.39$, $p=.15$).

Thus, while the structural paths were informative regarding the topology of the RCN, the individual variations in connection strength within this network were not predictive of behavior.

Discussion

We assessed the role that changes in resting state functional connectivity may have on associative episodic memory consolidation. We indexed consolidation by administering a cued recollection test 24 hours after the encoding task was performed. While consolidation and hippocampal-cortical transfer are known to occur on longer timescales (days to weeks; Frankland and Bontempi, 2006), evidence from this study suggests that memory servicing interactions between the hippocampus and cortex begin in the idle periods immediately following a learning episode.

Previous studies in humans have reported similar post-task alterations in functional connectivity being predictive of subsequent retrieval (Tambini et al., 2010). Tambini and colleagues used a similar task associating faces with places or objects and found that increases in post-task hippocampal FC with the lateral occipital cortex were important for recognition on a memory task immediately following the scan session. In that case, while an effect on subsequent memory was apparent, it was not determined whether the hippocampal-cortical interactions were of a consolidative nature. We delayed the memory test for a sufficiently long interval to eliminate any short-term memory effects (Takashima et al., 2009).

Importantly, the hippocampus also showed active engagement during the encoding task for subsequently recognized associations. Associative memory typically requires the hippocampus more than extra hippocampal structures, which tend to engage more in single item encoding (Davachi and Wagner, 2002). As a further support for the associative role of the hippocampus, two of the regions for which it displayed most elevated FCΔ were the lingual gyrus and the fusiform gyrus. The lingual gyrus has been associated with the parahippocampal gyrus in the visual processing of places, specifically buildings (Gorno-Tempini and Price, 2001), which constituted the majority of our “place” stimuli. Meanwhile, the fusiform gyrus is a key component of the system for facial recognition (Kanwisher et al., 1997).

We also detected that FCΔ increases between the hippocampus and the OFC were predictive of subsequent recall. The orbitofrontal cortex has previously been shown to interact with the hippocampus during the encoding of novel objects (Ranganath et al., 2005) and associations involving faces (Tsukiura and Cabeza, 2008). Here the association was with the lateral OFC, which is known from connectivity studies in primates to be a convergence zone for limbic and heteromodal association areas (Elliott et al., 2000) and may be involved in the active retrieval of information from posterior association areas (Petrides, 1996).

The structural integration of this subnetwork of regions was investigated using DSI tractography and graph theory. Direct connectivity between the six areas of the RCN was relatively sparse (3 out of 18 possible pairs). We therefore calculated the shortest paths between our primary region of interest, the hippocampus, and the remaining nodes. All of the shortest pathways traversed the parahippocampal gyrus. This finding is consistent with existing neuroanatomic literature. From primate neuroanatomy studies, it is known that most cortical input to the hippocampus stems from the parahippocampal gyrus via the entorinal cortex, acting as a gateway (Squire et al., 2004). We tested various properties of structural connectivity at the individual level for potential relationships to performance on the cued recognition test (see Results) but did not detect any within this subnetwork. It may be that basic tests like ours exhibit more variability than do more rigorous tests of stable cognitive traits, like those that have revealed relationships between structural connectivity and IQ (Li et al., 2009) and risk-seeking behavior (Cohen et al., 2009). Connectivity between the hippocampus and the orbitofrontal cortex involves the uncinate fasiculus, whose pathway converged largely with the shortest path we detected between these regions. A study by Metzler-Baddeley and colleagues (Metzler-Baddeley et al., 2012) found a relationship between the fractional anisotropy of the uncinate fasciculus in aging individuals and performance on an object-location paired associate learning task similar to the one used here. Our method was able to triangulate the uncinate as a likely pathway binding part of this network. Graph theory and shortest pathway detection is likely to be a more sensitive method for detecting connectivity between areas that may not have fibers from fiber tractography directly connecting them.

It remains to be seen whether the post-task alterations in functional connectivity are indicative of a) memory performance at more delayed points and b) later hippocampal independence when retrieving the episode. It is possible that they are residual fluctuations among regions that were previously engaged in the task, in which case their nature would be more biophysical than psychological. We also did not detect any relationship between functional

connectivity of the medial prefrontal cortex and the hippocampus with consolidation, as was our hypothesis. Instead we found that hippocampal-lateral prefrontal (orbitofrontal) connectivity was predictive of memory performance. Previous work has indicated a role for OFC in the processing of the semantic aspects of memory encoding. Given that subjects in our task were instructed to actively form an association between each place and person, such elaboration may well engage this cortical area.

Methods

Subjects

Healthy young subjects were recruited from the University of Caifornia Los Angeles (UCLA) community to participate in this experiment. All subjects provided written informed consent for the study which was approved by the UCLA Institutional Review Board. 15 right-handed subjects, 8 male/7 female, mean age 25.5 +/- 3 years (range 21.9-31.5) participated in the study.

Experimental Design

Subjects participated in the study on two consecutive days. On day 1, subjects were first familiarized with a set of 45 recognizable faces (e.g. Barack Obama, Kim Kardashian, Leonardo DiCaprio) and 45 recognizable places (e.g. Eiffel Tower, Golden Gate Bridge, Taj Mahal) outside of the scanner. Two familiarization tasks were administered. In the first task, the subject would be shown a single 200x200 image of a face or place without any identifying text and prompted, 'How well do you recognize this person?', to which they were instructed to select one of four possible replies from 'Not at all, Vaguely, Pretty Well, Instantly.' This was completed for all 90 subjects. In the second task, they were shown the same set of 90 images in a different sequence, along with the name of the object above the object, and instructed to ‘Type the name exactly as it appears.’ The purpose of these tasks were to 1) assess subject familiarity with the

stimuli and 2) to train them on the specific handles associated with each stimulus for a surprise free recall test the following day.

Inside the scanner, subjects underwent fMRI scanning while performing the memory association task. Subjects were told they were playing a game called 'Traveling with the Stars,' where they would be seeing a pair of one person at one place. They were asked to try and remember the association but were not informed of any subsequent memory test. Each person place pair appeared side by side with the name of each printed directly below the image. The left/right position of faces and places was pseudo-randomized to approximately half in each position. The pairing of places and faces was randomly assigned when the experiment was created and was subsequently kept constant for all subjects, in order to assure that any common semantic associations between people and places were maximally similar across subjects. The presentation order was randomized for each subject and also randomized with respect to the presentation order during training. Stimuli appeared on the screen for 5 seconds, followed by a 5 second period of fixation on a dot in the center of the screen. This was followed by a baseline task were the subject was shown a single digit in the middle of the display between 1-8 and instructed to press button 1 on the button box for odd digits and button 2 for even digits. This simple but active baseline was intended to enhance the ability to detect memory encoding-related activation (Stark and Squire, 2001). The task was self-paced and the duration was jittered to exponentially decay from a maximum of 10s (mean=9.4 +/- .6s). This sequence continued until the subject had been shown all 45 pairs.

In addition to the fMRI task, subjects also received a resting state fMRI scan both before and after the task. They were instructed to keep their eyes open, blinking normally, and fixate on a green dot in the center of the screen with a gray background. Each resting state scan lasted 8:30.

The final fMRI task was a functional localizer intended to map out the brain regions of maximal activation during the viewing of faces and places, specifically the fusiform face area (FFA; Kanwisher et al., 1997) and the parahippocampal place area (PPA; Epstein and Kanwisher, 1998). In order to maximize the similarity to the task, different famous faces were selected (e.g. David Beckham, Penelope Cruz) and "famous looking" places were selected from an online database (http://cvcl.mit.edu/database.htm) based on characteristics of ornate or striking architecture. As a control, subjects were also shown images of common objects from an online database. There were seven blocks each of faces, places, and objects. Each block contained 14 total images, two of which were repeats of the previously shown image. Subjects were instructed to take mental note of when the same image appeared consecutively. Images were shown for .75s followed by a .25 second fixation. Blocks were separated by a 14s fixation. Block order was pseudo randomized and the total duration of the scan was 6:52.

Subjects returned the following day, 24 +/- 2 hours following their initial visit. They were given a surprise test that consisted of the components. The first was a "free recall" written test in which they were instructed to write down as many person/place pairs as they could remember. Guessing was permitted but subjects were instructed to maintain a one-to-one mapping between people and places (ie no repeats). The identity of each correctly recalled pair was tallied, along with the total score. In the second portion, "cued recollection", a computer test was administered in which one cue image would appear on the screen, either a previously seen face or place, along with its name. Next to it was a blank where the subject was instructed to type the corresponding face/place name if they recalled. The same guessing rules were explained. The percentage of faces and/or places was pseudo-randomized to be approximately balanced. In the third portion of the test, "cued recognition", the subject was shown one face or place, along with its name, and beneath it five choices from the corresponding category (ie one face and five possible places). One of the five choices was always correct, and all five choices were selected

from the set of 45. This ensured that some choices were repeated though this set was pseudo-randomized in order for each item to appear approximately (5*22)/45= 2 times.

MRI Acquisition Parameters

All scanning was conducted at the UCLA Staglin IMHRO Center for Cognitive Neuroscience on a Siemens 3T Tim Trio scanner using a Siemens 12-channel head coil. All fMRI data were acquired with a T2*-weighted sequence with TR=2000ms, TE=30ms, voxel size=3mm^3, FoV=192x192, 36 slices with slice thickness=3mm and a .75 mm gap, flip angle=78 degrees. Scan prescription was oriented obliquely to be approximately parallel with the base of the temporal lobes. The pre-task and post-task rsfMRI scans lasted for 8:30. The task fMRI had a duration of ~16:30, depending on the length of the jitter. The localizer scan had a duration of 7:00.

Diffusion spectrum imaging (DSI) data were acquired using a twice-refocused spin-echo EPI sequence with 257 diffusion encoding directions. A half sphere scheme with 5 q-values was used (TR=9200ms, TE=156ms, voxel size=2.5mm^3, FoV=236x236, 48 slices, maximum b-value=7000s/mm^2). A T1-weighted MP-RAGE anatomical scan was collected with TR=1900ms, TE=2.26ms, voxel size=1mm^3, FoV=256x246, flip angle=9 degrees. Finally, a T2-weighted sequence coplanar and matched in bandwidth to the fMRI sequence was obtained (TR=5000ms, TE=34ms, 36 slices, voxel size=3x3x3.75mm).

MRI Preprocessing

Resting state fMRI were processed with tools from the FMRIB Software Library (FSL; http://fsl.fmrib.ox.ac.uk/fsl/fslwiki/). Resting state data were skull stripped using BET and motion corrected using MCFLIRT. Next spatial smoothing was applied with a 6mm FWHM Gaussian kernel. The first five volumes were dropped in order to allow for scanner equilibration. Data were bandpass temporal filtered between .08-.009 Hz to isolate low-frequency fluctuations and

attenuate ultralow frequencies related to scanner drift and higher frequencies related to cardiac and respiratory fluctuations. Each subject's anatomical scan was segmented into gray matter, white matter (WM), and CSF tissue-type masks using FSL FAST. These masks were registered to each subject's functional scan and thresholded at a very high level in order to obtain high-confidence "core" WM and CSF masks. Mean WM and CSF timeseries were calculated and statistically regressed out of the fMRI data, along with their temporal derivatives and the six motion parameters output by MCFLIRT. Denoised rsfMRI data were resampled to 4mm isotropic MNI152 standard space, via intermediate registration between the matched bandwidth T2 scan, the skull-stripped T1 structural scan, and standard space.

Whole brain data was processed similarly up unto the point of bandpass filtering. Instead, only a high pass filter was used. No subject in any scan had more than 1.5mm of absolute motion.

fMRI Analysis

Denoised fMRI data were subjected to functional parcellation using the spatially constrained spectral clustering method (Craddock et al., 2012). This method is a purely data-driven way to obtain an arbitrary number of functionally homogenous, roughly equally sized regions of interest that are maximally consistent across subjects. This method is preferred to anatomical parcellation methods which may include large anatomical areas such as the precuneus or anterior cingulate that are known have functionally independent dissociations within them (Margulies et al., 2009; Shirer et al., 2012). We input all 15 subjects' pre-task and post-task scans (30 total) in order to obtain a functional atlas that was tailored to our experimental conditions, while enforcing group consistency to eliminate behaviorally driven differences. We used similarity of each voxels' timeseries (tcorr) as the similarity measure. We also used a mask covering the cortical gray matter and subcortical areas as defined by the Harvard-Oxford cortical/subcortical atlas distributed with FSL. We obtained a set of 199 cortical

and subcortical ROIs with an average size of ~7000mm^3. For each scan, the average timeseries from each ROI was obtained and the Pearson correlation coefficient between each pair of ROIs was plugged into a 199x199 functional connectivity matrix. The functional connectivity change (FCΔ) measure was calculated by subtracting the post – pre FC matrices.

Whole brain fMRI were statistically analyzed using FSL FEAT. Regressors were produced for each subject's correct and incorrect responses on the free recall, cued recollection, and cued recognition tests. For each of the three task types, single subject analyses were run looking at contrasts of correct events vs. baseline, incorrect events vs. baseline, all events vs. baseline, and correct events vs. incorrect events, both during stimulus presentation and post-stimulus fixation. Analysis here employed a pre-thresholding mask of the bilateral hippocampus using masks of hippocampus and parahippocampal gyrus. Z-statistic parametric maps were analyzed for contiguous cluster with $Z > 2.0$ ($p < .05$).

DSI Analysis

All DSI analysis was performed using DSI Studio (http://dsi-studio.labsolver.org/). Data were reconstructed using the GQI method and a half-sphere scheme with an eight-fold orientation distribution function tessellation for modeling diffusion within each voxel. 3 potential fibers were resolved per voxel. Fiber tracking was run with the default subject-specific fiber threshold with a maximum turn angle of 75 in order to detect near orthogonal fibers that have recently been characterized (Wedeen et al., 2012). A step size of .5mm was used with 80% smoothing, a minimum length of 10mm (4 voxels), sampling the main direction at the subvoxel level requesting 100000 streamlines, in order to ensure a constant count across subjects and search for relative differences in fiber density.

The ROIs from the functional atlas were used as seeds for tractography. These standard space ROIs were registered to the generalized fractional anisotropy (GFA) map via the intermediate T1 structural scan. Once all 199 ROIs had been registered to subject-specific

diffusion space, they were dilated once using fslmaths. This ensured the inclusion of the gray/white matter interface where tractography estimates are more reliable (Wedeen et al., 2008). Because of slight overlap in masks, they were subjected to a winner-take-all thresholding step, where the masks with the highest probability value in each voxel kept that voxel. ROIs maintained they homogenous volume throughout this process. For each pair of ROIs, the number of tractography streamlines that intersected both of them at any point were counted and plugged into a 199x199 structural connectivity (SC) matrix.

Network Analysis

SC matrices were assessed for shortest paths between the hippocampus and the five other regions in the recognition consolidation network using Dijkstra's algorithm in NetworkX (http://networkx.github.com/).

Statistical Analysis

All relationships between neuroimaging measures and test scores were performed using linear corrleations in MATLAB (http://www.mathworks.com).

Chapter 4 References

Andrews-Hanna, J.R., Reidler, J.S., Sepulcre, J., Poulin, R., Buckner, R.L., 2010. Functional-anatomic fractionation of the brain's default network. Neuron 65, 550–562.

Ben-Yakov, A., Dudai, Y., 2011. Constructing realistic engrams: poststimulus activity of hippocampus and dorsal striatum predicts subsequent episodic memory. J. Neurosci. 31, 9032–9042.

Cohen, M.X., Schoene-Bake, J.-C., Elger, C.E., Weber, B., 2009. Connectivity-based segregation of the human striatum predicts personality characteristics. Nat Neurosci 12, 32–34.

Craddock, R.C., James, G.A., Holtzheimer, P.E., 3rd, Hu, X.P., Mayberg, H.S., 2012. A whole brain fMRI atlas generated via spatially constrained spectral clustering. Hum Brain Mapp 33, 1914–1928.

Davachi, L., Wagner, A.D., 2002. Hippocampal contributions to episodic encoding: insights from relational and item-based learning. J. Neurophysiol. 88, 982–990.

Elliott, R., Dolan, R.J., Frith, C.D., 2000. Dissociable Functions in the Medial and Lateral Orbitofrontal Cortex: Evidence from Human Neuroimaging Studies. Cereb. Cortex 10, 308–317.

Epstein, R., Kanwisher, N., 1998. A cortical representation of the local visual environment. Nature 392, 598–601.

Euston, D.R., Tatsuno, M., McNaughton, B.L., 2007. Fast-Forward Playback of Recent Memory Sequences in Prefrontal Cortex During Sleep. Science 318, 1147–1150.

Felleman, D.J., Van Essen, D.C., 1991. Distributed hierarchical processing in the primate cerebral cortex. Cereb. Cortex 1, 1–47.

Frankland, P.W., Bontempi, B., 2005. The organization of recent and remote memories. Nat Rev Neurosci 6, 119–130.

Frankland, P.W., Bontempi, B., 2006. Fast track to the medial prefrontal cortex. PNAS 103, 509–510.

Gorno-Tempini, M.L., Price, C.J., 2001. Identification of famous faces and buildings A functional neuroimaging study of semantically unique items. Brain 124, 2087–2097.

Ji, D., Wilson, M.A., 2007. Coordinated memory replay in the visual cortex and hippocampus during sleep. Nat Neurosci 10, 100–107.

Kanwisher, N., McDermott, J., Chun, M.M., 1997. The fusiform face area: a module in human extrastriate cortex specialized for face perception. J. Neurosci. 17, 4302–4311.

Kesteren, M.T.R. van, Fernández, G., Norris, D.G., Hermans, E.J., 2010. Persistent schema-dependent hippocampal-neocortical connectivity during memory encoding and postencoding rest in humans. PNAS 107, 7550–7555.

Li, Y., Liu, Y., Li, J., Qin, W., Li, K., Yu, C., Jiang, T., 2009. Brain Anatomical Network and Intelligence. PLoS Comput Biol 5, e1000395.

Logothetis, N.K., Eschenko, O., Murayama, Y., Augath, M., Steudel, T., Evrard, H.C., Besserve, M., Oeltermann, A., 2012. Hippocampal-cortical interaction during periods of subcortical silence. Nature 491, 547–553.

Margulies, D.S., Vincent, J.L., Kelly, C., Lohmann, G., Uddin, L.Q., Biswal, B.B., Villringer, A., Castellanos, F.X., Milham, M.P., Petrides, M., 2009. Precuneus shares intrinsic functional architecture in humans and monkeys. Proceedings of the National Academy of Sciences 106, 20069 –20074.

Metzler-Baddeley, C., Jones, D.K., Steventon, J., Westacott, L., Aggleton, J.P., O'Sullivan, M.J., 2012. Cingulum Microstructure Predicts Cognitive Control in Older Age and Mild Cognitive Impairment. J. Neurosci. 32, 17612–17619.

Petrides, M., 1996. Specialized systems for the processing of mnemonic information within the primate frontal cortex. Philos. Trans. R. Soc. Lond., B, Biol. Sci. 351, 1455–1461; discussion 1461–1462.
Ranganath, C., Heller, A., Cohen, M.X., Brozinsky, C.J., Rissman, J., 2005. Functional connectivity with the hippocampus during successful memory formation. Hippocampus 15, 997–1005.
Shirer, W.R., Ryali, S., Rykhlevskaia, E., Menon, V., Greicius, M.D., 2012. Decoding subject-driven cognitive states with whole-brain connectivity patterns. Cereb. Cortex 22, 158–165.
Squire, L.R., Stark, C.E.L., Clark, R.E., 2004. The Medial Temporal Lobe*. Annual Review of Neuroscience 27, 279–306.
Stark, C.E.L., Squire, L.R., 2001. When zero is not zero: The problem of ambiguous baseline conditions in fMRI. PNAS 98, 12760–12766.
Takashima, A., Nieuwenhuis, I.L.C., Jensen, O., Talamini, L.M., Rijpkema, M., Fernández, G., 2009. Shift from Hippocampal to Neocortical Centered Retrieval Network with Consolidation. The Journal of Neuroscience 29, 10087 –10093.
Takashima, A., Petersson, K.M., Rutters, F., Tendolkar, I., Jensen, O., Zwarts, M.J., McNaughton, B.L., Fernández, G., 2006. Declarative memory consolidation in humans: A prospective functional magnetic resonance imaging study. Proceedings of the National Academy of Sciences of the United States of America 103, 756 –761.
Tambini, A., Ketz, N., Davachi, L., 2010. Enhanced Brain Correlations during Rest Are Related to Memory for Recent Experiences. Neuron 65, 280–290.
Tsukiura, T., Cabeza, R., 2008. Orbitofrontal and hippocampal contributions to memory for face-name associations: The rewarding power of a smile. Neuropsychologia 46, 2310–2319.
Wedeen, V.J., Rosene, D.L., Wang, R., Dai, G., Mortazavi, F., Hagmann, P., Kaas, J.H., Tseng, W.-Y.I., 2012. The Geometric Structure of the Brain Fiber Pathways. Science 335, 1628–1634.
Wedeen, V.J., Wang, R.P., Schmahmann, J.D., Benner, T., Tseng, W.Y.I., Dai, G., Pandya, D.N., Hagmann, P., D'Arceuil, H., De Crespigny, A.J., 2008. Diffusion spectrum magnetic resonance imaging (DSI) tractography of crossing fibers. NeuroImage 41, 1267–1277.

Chapter 5

The UCLA Multimodal Connectivity Database: A Web-Based Platform for Brain Connectivity Matrix Sharing and Analysis[2]

Jesse A. Brown, Jeffrey D. Rudie, Anita Bandrowski, John D. Van Horn, Susan Y. Bookheimer

Abstract

Brain connectomics research has rapidly expanded using functional MRI (fMRI) and diffusion-weighted MRI (dwMRI). A common product of these varied analyses is a connectivity matrix (CM). A CM stores the connection strength between any two regions ("nodes") in a brain network. This format is useful for several reasons: 1) it is highly distilled, with minimal data size and complexity, 2) graph theory can be applied to characterize the network's topology, and 3) it retains sufficient information to capture individual differences such as age, gender, intelligence quotient, or disease state. Here we introduce the UCLA Multimodal Connectivity Database (http://umcd.humanconnectomeproject.org), an openly available website for brain network analysis and data sharing. The site is a repository for researchers to publicly share CMs derived from their data. The site also allows users to select any CM shared by another user, compute graph theoretical metrics on the site, visualize a report of results, or download the raw CM. To date, users have contributed over 2000 individual CMs, spanning different imaging modalities (fMRI, dwMRI) and disorders (Alzheimer's, autism, Attention Deficit Hyperactive Disorder). To demonstrate the site's functionality, whole brain functional and structural connectivity matrices are derived from 60 subjects' (ages 26-45) resting state fMRI (rs-fMRI) and dwMRI data and uploaded to the site. The site is utilized to derive graph theory global and regional measures for the rs-fMRI and dwMRI networks. Global and nodal graph theoretical measures between functional and structural networks exhibit low correspondence. This example demonstrates how this tool can enhance the comparability of brain networks from different imaging modalities and

[2] *Frontiers in Neuroinformatics*. 28 November 2012. doi: 10.3389/fninf.2012.00028

studies. The existence of this connectivity-based repository should foster broader data sharing and enable larger-scale meta analyses comparing networks across imaging modality, age group, and disease state.

Introduction

Successful neuroimaging data sharing efforts have taken a variety of organizational approaches, including top-down centralized strategies and bottom-up grassroots efforts. Centralized projects such as the Alzheimer's Disease Neuroimaging Initiative (ADNI; http://www.adni-info.org) begin by defining a targeted subject population, the type of imaging data to be included, and a set of criteria to ensure the quality and similarity of the data collection across multiple sites and scanners. Grassroots projects like the International Neuroimaging Datasharing Initiative (INDI; http://fcon_1000.projects.nitrc.org/index.html) are less restrictive and encourage the broad sharing of data across centers, subject pools, and scan types. Once data has been collected, it can be stored in a database where users can search and download desired data. This allows researchers to freely access the data, enabling them to apply their own preprocessing and run custom analyses. These sites typically collect image files in a specific format such as NiFTI or DICOM along with relevant meta-information about the data acquisition, the individual receiving the scan, and the study design.

Another variety of neuroimaging databases store processed data and/or analysis results. The BrainMap database (http://brainmap.org) stores stereotaxic standard-space coordinates of activation peaks from fMRI and PET data analyses and associated metadata including the number of subjects, the subject disease state (healthy or diseased), the applied analysis techniques, the experimental paradigm, and the cognitive process under investigation (e.g. working memory) (Fox and Lancaster, 2002) (Laird et al., 2005). SUMS-DB is a database for sharing structural and functional brain mapping study results, also based on stereotaxic coordinates (http://sumsdb.wustl.edu). These databases foster meta-analyses by compiling

findings across studies into a common coordinate space, allowing users to probe for findings within a specific brain region or network.

In between the extremes of stereotaxic foci and raw data repositories exist many intermediates of “processed” neuroimaging data. Processed data is beneficial in a shared data setting because it requires less analysis by subsequent users than raw data, while enabling more thorough re-analysis than a set of significant spatial coordinates does. One example of processed neuroimaging data that has been particularly useful in explaining brain connectivity properties is the “connectivity matrix” (CM). A typical connectivity analysis in a neuroimaging study measures the strength of connection between different brain regions. Connection strength definition is based on a variety of methods. In functional MRI (fMRI), the statistical correlation of BOLD intensity changes in two regions is commonly used as a measure of “functional connectivity”. In diffusion tensor imaging (DTI) and related diffusion-weighted MRI (dwMRI) modalities, the experimenter quantifies the density of axonal bundles or “structural connectivity” between two regions using fiber tractography methods. For neuroimaging experiments whose field of view is sufficiently large to cover the entire brain, one can determine the whole brain connectivity “graph” by portioning the brain into constituent regions and determining the direct connectivity between every pair of regions. In this graph representation of connectivity, the pattern of connections between nodes is stored in a CM where rows/columns in the matrix represent brain regions (nodes) and the matrix cell where these two regions intersect stores the connection strength between the two regions (edges).

Graph theoretical analyses can be performed on a CM in order to characterize a network’s global integration, local interconnectivity, modularity, cost efficiency, and robustness to lesioning (Bullmore and Sporns, 2009) (Sporns, 2010). Analyses of CMs derived from structural and functional neuroimaging modalities have led to the recognition of a core set of structural hubs in the posterior cingulate and precuneus (Hagmann et al., 2008); the determination that functional network hubs coincide with the sites of greatest amyloid deposition

in Alzheimer's Disease (Buckner et al., 2009); and the discovery that flexible reconfiguration of functional connectivity modules is critical for motor learning (Bassett et al., 2011b). CMs have been derived from structural and functional MRI data from the same subjects in several studies, indicating moderate correspondence of the structural and functional connectivity strength between regions (Honey et al., 2007) (Honey et al., 2009) (Hagmann et al., 2010).

Connectivity matrices are a highly distilled representation of brain connectivity. Despite this reduction, they contain sufficient information to capture individual characteristics such as age (Dosenbach et al., 2010), gender (Yan et al., 2011), intelligence quotient (IQ) (Li et al., 2009) (Van den Heuvel et al., 2009b), and disease state (Supekar et al., 2008) (Craddock et al., 2009) (Lo et al., 2010). Graph theory adds to the utility of a connectivity matrix by quantifying how brain regions are integrated into a global unit, rather than how they act in isolation. A great deal of research effort and funding has been dedicated to describing the human connectome, which is at its essence a CM (Sporns et al., 2005). CMs are therefore an ideal product to compile and share with the community. Here we present the UCLA Multimodal Connectivity Database (UMCD henceforth; http://umcd.humanconnectomeproject.org), a website that allows CMs and meta-information to be uploaded and shared with the public. It provides a dynamic, sortable search engine for locating relevant datasets. It also provides a platform for graph theory analysis of any publicly shared CM, reporting basic graph properties, graph theoretical metrics, and interactive 3D/2D visualizations.

Material and Methods

The UCLA Multimodal Connectivity Database

The UMCD is a public website found at http://umcd.humanconnectomeproject.org. The site has five main options:

1) ‘Analyze a network’, where the user selects any publicly shared network, configures analysis parameters, and the initiates the network analysis **(Figure 1)**. Once the analysis is complete, the user is redirected to a Results page (contents described below)

2) ‘Compare networks’, similar to ‘Analyze’ but allows the user to select two networks to compare side by side

3) ‘Lesion a network’, similar to ‘Analyze’, with the additional option to select any subset of regions in the chosen network to virtually ‘lesion’, setting all connections from the selected nodes to zero; the results of the analysis for the unlesioned and lesioned versions of the network are displayed side by side

4) ‘Browse networks’, allows the user to view all available networks and keyword search for specific datasets or sort all datasets based on different criteria **(Figure 2)**

5) ‘Upload a network’, where the user can upload data, either to share with the public or to keep private but compare to public data. **(Figure 3)**

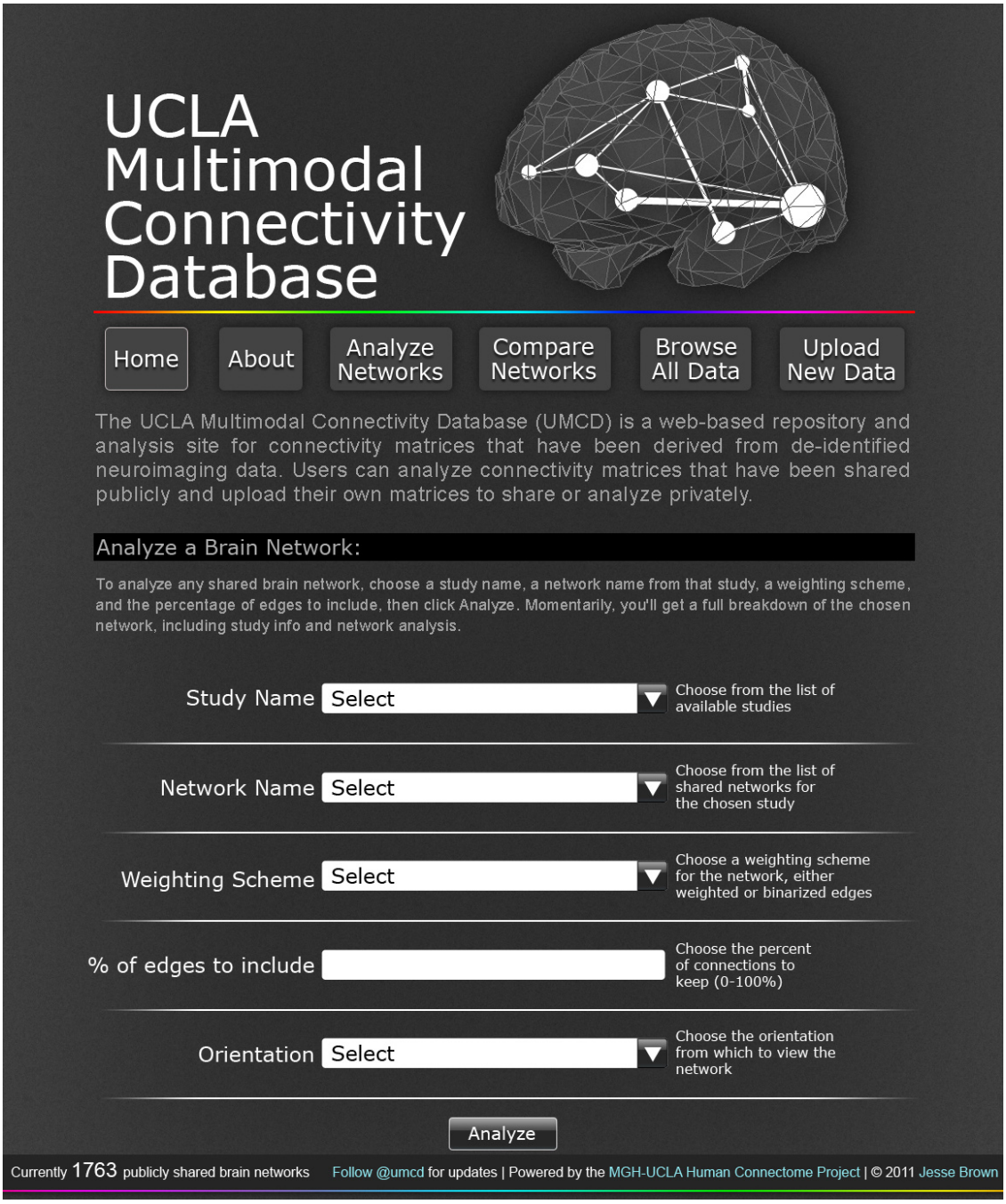

Figure 1: The UCLA Multimodal Connectivity Database homepage, where a user can configure the analysis for any connectivity matrix publicly shared on the site. The user can select from any of the studies for which data has been publicly shared on this site with the 'Study Name' dropdown menu. Once a study is selected, all the individual brain networks that have been shared for that study will appear in the 'Network Name' dropdown menu. After selecting an individual network to analyze, the user must specify a 'Weighting scheme' and '% of edges to include' for the analysis, choose an orientation in which to render the analysis-based network images, and click 'Analyze'.

Browse All Data

All datasets are viewable here that are publicly shared. If you're logged in, you can also see all of your private data. Click on any column to sort or just enter a search term.

Display 25 entries Search:

Details Page	Analyze	Study Name	Network Name	Atlas	Imaging Modality	Share	Scanner Device	Age Ran
View/Download	Analyze	ICBM	UCLA_ICBM_1004_DTI	Freesurfer 85	DTI	Public	Siemens 1.5T	45
View/Download	Analyze	ICBM	ICBM_thickness_corrmat	Freesurfer_68	Strucutral MRI	Public	Siemens Allegra 1.5T	18
View/Download	Analyze	ICBM	ICBM_DTI_tractography	Freesurfer_68	DTI	Public	Siemens 1.5T	18
View/Download	Analyze	ADHD200_CC200	KKI_2371032	Craddock 200	fMRI	Public		10.73
View/Download	Analyze	ADHD200_CC200	KKI_2026113	Craddock 200	fMRI	Public		12.99
View/Download	Analyze	ADHD200_CC200	KKI_3434578	Craddock 200	fMRI	Public		8.12
View/Download	Analyze	ADHD200_CC200	KKI_8628223	Craddock 200	fMRI	Public		10.81
View/Download	Analyze	ADHD200_CC200	KKI_1623716	Craddock 200	fMRI	Public		12.65

Figure 2: The 'Browse All Data' page. Studies are initially listed in the order in which they were shared by users. Any column can be sorted by clicking on the heading, allowing for example the grouping of all DTI studies, or the sorting of networks based on the age of the subject. The 'Search' field can be used to dynamically constrain which records from the database are shown. The 'View/Download' link takes the user to a 'profile' page for the individual network that contains more detailed information **(see Figure 5).** The 'Analyze' link takes the user to the 'Analyze Network' page with the 'Study Name' and 'Network Name' pre-selected, allowing the user to run a network analysis simply by clicking 'Analyze'.

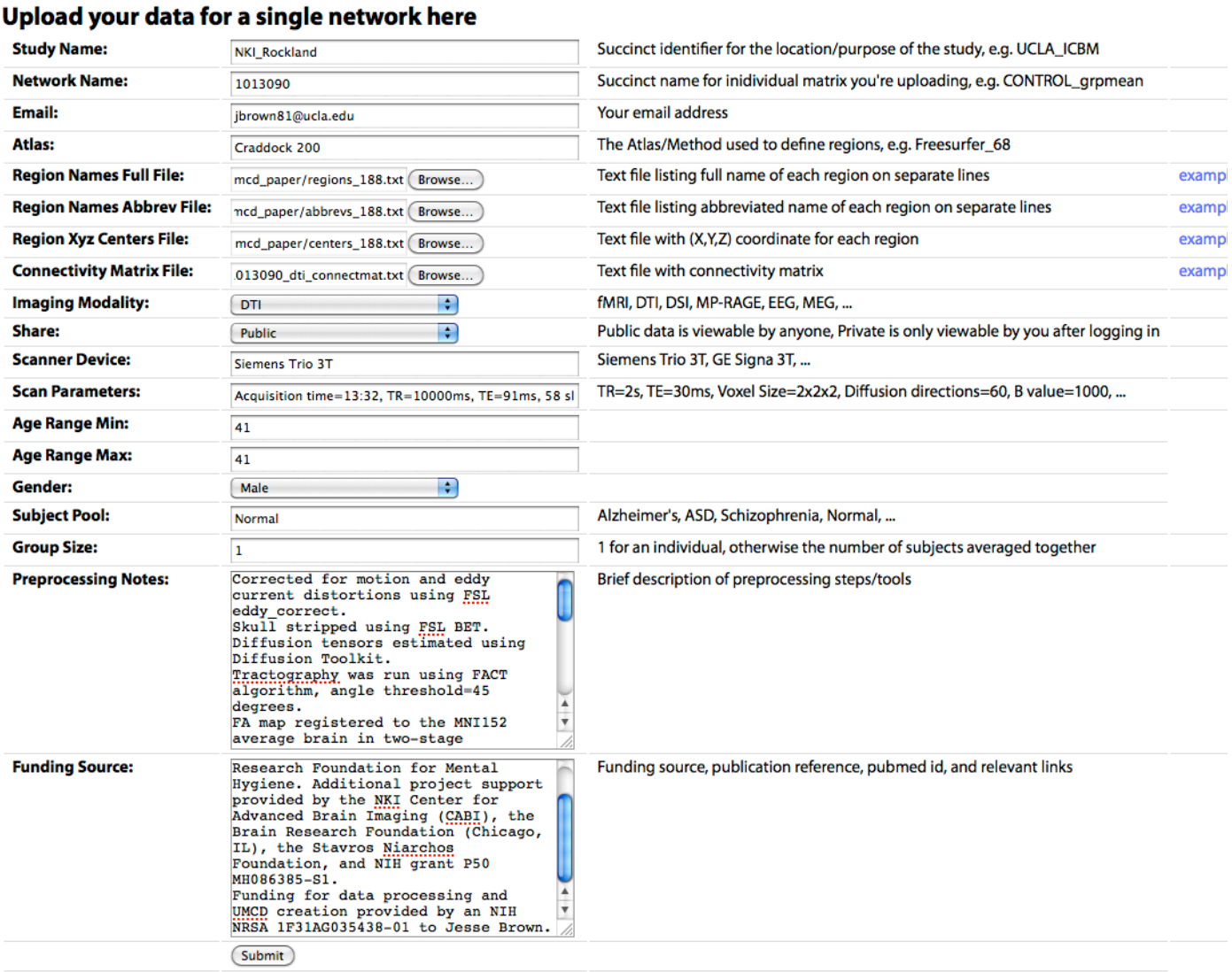

Figure 3: The 'Upload New Data' page, where a user can upload a connectivity matrix. Descriptions of each field are included in the main text.

The UMCD requires users to register with an email address and a password in order to share data. Once an account has been created, the user has the option to share data Publicly, in which case any site visitor can analyze or download the data, or Privately, allowing only the user to access this data when they are logged in.

Design

The UMCD is built with the web2py framework (http://web2py.com). This Python-based framework uses the Model-View-Controller (MVC) architecture. This enables the seamless

coupling of HTML pages with Python code and libraries for performing data analysis and visualization. The site uses a MySQL (http://www.mysql.com) database to store all data including user account information and shared data. The NetworkX Python library is used for all graph theory analyses (http://networkx.lanl.gov). This open source library has excellent documentation, an active community, and the ability to easily create network-based visualizations. These visualizations are rendered by passing custom NetworkX Graph objects from NetworkX to matplotlib (http://matplotlib.sourceforge.net), an extensive library for creating data visualizations in Python. All mathematical and statistical calculations use the numpy (http://numpy.scipy.org) and scipy (http://www.scipy.org) libraries.

Analysis

On the analysis page, the user can select any "Study Name" for which data has been shared. Once a Study Name has been selected, the individual connectivity matrices associated with that study name will become selectable in the "Network Name" dropdown. The user can select any Network Name. To conduct the network analysis, the user selects a Network Name and then must specify two variables: the Weighting Scheme, which can be binary (the default option) or weighted, specifying the % of edges to include, which can be any integer value between 0-100 (20 is the default option). An additional variable, Orientation, dictates the imaging plane in which the network figures will be rendered: axial (default), sagittal, or coronal view. Once all options are specified, the user clicks the Analyze button to run the network analysis.

The analysis can take between 10 seconds to 3 minutes depending on the size of the network, the weighting scheme, and the threshold. When the analysis is complete, the results are displayed on the Analyzed Network page (**Figure 4**).

A Analyzed Network

Network information

Name	NKI_fc_avg_26_45
Atlas	Spatially Constrained Spectral Clustering 200
Imaging Modality	fMRI
Subject Pool	Normal
Group Size	60
Age Range	26-45
Preprocessing Notes	1) FSL slicetimer, 2) FSL MCFLIRT, 3) FSL BET, 4) spatially smooth w/ 5mm FWHM Gaussian, 5) scale to mean 10000, 6) band pass temporal filter from .08-.0099Hz, 7) FSL FAST MPRAGE, 8) register CSF and WM masks to fMRI space, 9) mask the CSF and WM masks with conservative ventricular and core white matter masks derived from the MNI152 atlas, 10) extract mean timeseries from the core CSF, core WM, and whole brain, 11) regress CSF, WM, whole brain signal, six motion parameters, and all temporal derivatives from BOLD data, 12) motion scrubbing of TRs w/ relative motion displacement greater than .5mm or relative BOLD signal intensity change greater than .5% (Power et al., 2012), 13) register BOLD w/ FSL FLIRT to MNI152 average brain with 4mm3 voxel resolution in three stage registration from fMRI > initial T2 structural > MPRAGE > MNI152, 14) Residual BOLD data analyzed w/ spatially constrained spectral clustering method (Craddock et al., 2011) at group level to derive group-level 188 gray matter ROIs, 15) mean timeseries for each ROI correlated with all remaining ROI timeseries'.

Global Network Metrics

Raw Density (%) ?	100.0
Chosen Density (%) ?	5
Characteristic Path Length ?	3.97101135274
Clustering Coefficient ?	0.406553854663
Number of Components ?	1
Global Efficiency ?	0.314900815021
Modularity (Q) ?	0.690986578019
Small world attributes	
Sigma ?	4.21784165125
Gamma ?	7.14431944982
Lambda ?	1.69383301711
Edge weight attributes	
Unthresholded (raw) network	
Edge weight mean +/- stddev:	0.0172391155304 +/- 0.198908950318
Edge euclidean length mean +/- stddev:	83.4942918566 +/- 30.6834030805
Thresholded network	
Edge weight mean +/- stddev:	0.539129988767 +/- 0.0998049709707
Edge euclidean length mean +/- stddev:	43.7330501574 +/- 27.7003353918

View Regional Report | Download Regional Measures as .txt | Download Entire Report as PDF

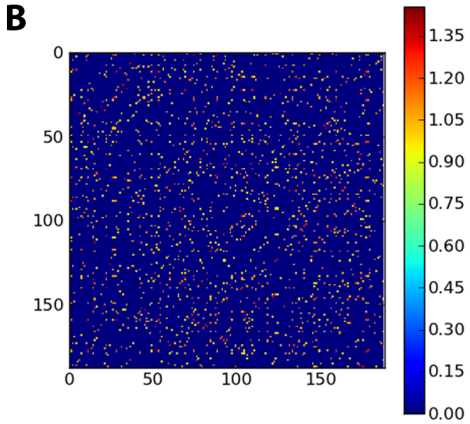

C Region report

NKI_fc_avg_26_45

Region Name	Degree	Clustering Coefficient	Betweenness Centrality	Module	Regional Efficiency	Participation Coefficient
Brain-Stem	10	0.459374666576	0.0135127364729	0	0.301177635426	0.408220597038
Right Planum Polare	17	0.505625740095	0.026220458858	1	0.377793066886	0.198274942469
Left Temporal Pole	8	0.499324426633	0.00350756138232	2	0.298384297214	0.0
Right Frontal Pole	4	0.155992794956	0.00402507043873	3	0.271294587623	0.0
Right Temporal Fusiform anterior	10	0.543748266429	0.00546259559542	2	0.307917238813	3.33066907388e-16
Left Frontal Pole	2	0.0	0.0	3	0.235100848715	0.0
Left Precuneous	5	0.474215962729	0.0128227243977	4	0.318101309601	0.639753344516
Right Juxtapositional Lobule	15	0.467095134617	0.0254154447703	1	0.356270192612	0.0
Right Supramarginal posterior	6	0.363777287816	0.0119602093037	3	0.31600540757	-2.22044604925e-16
Left Middle Temporal posterior	8	0.379791642522	0.011385199241	2	0.322647308912	0.204878765398
Left Temporal Fusiform anterior	10	0.539684759857	0.0021275372319	2	0.306795402775	0.0
Left Planum Temporale	16	0.593812593807	0.00161002817549	1	0.350516068043	3.33066907388e-16
Right Caudate	2	0.0	0.0	5	0.189376138419	0.0
Left Crus II	5	0.422710324122	0.0	0	0.217964324019	-4.4408920985e-16
Left Supramarginal anterior	17	0.525016417347	0.00759013282732	1	0.352663955979	5.55111512313e-16
Right Occipital Pole	14	0.613890898154	0.000115002012535	6	0.323806452715	0.0
Left Paracingulate	9	0.388767616622	0.0261629578518	3	0.320112009506	0.0
Right Inferior Temporal posterior	4	0.0	0.0258179518142	2	0.299063792895	0.597815536093
Left Caudate	2	0.0	0.0	5	0.196308037978	0.0
Left Thalamus	4	0.528926840971	0.0110976942096	5	0.262264961596	0.332923797096
Right Middle Frontal	7	0.46469827795	0.00143752515669	3	0.310786993903	0.0
Right Crus I	5	0.498679243299	0.000345006037606	0	0.222087382164	0.0
Left Postcentral	23	0.483028628709	0.004082571445	1	0.373240009066	3.33066907388e-16
Left Lateral Occipital superior	4	0.293167723961	0.00483008452648	4	0.299939342027	0.352315883388
Right Precuneous	5	0.510766932115	0.00885515496521	1	0.319106281661	0.290777380243

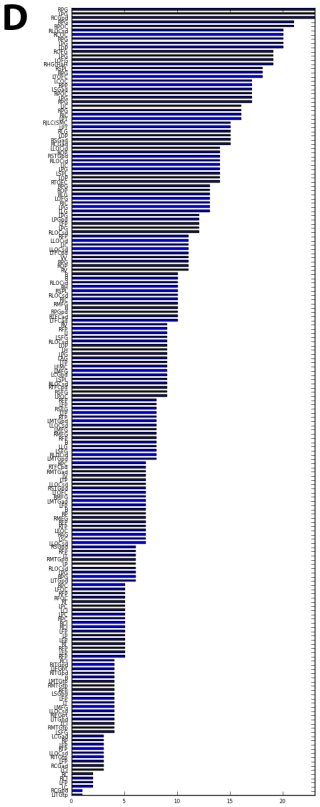

E 3D Network

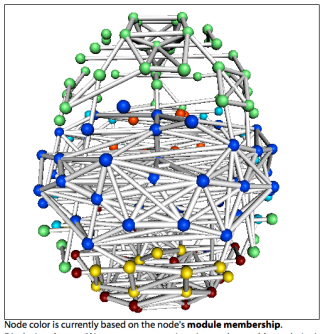

Node color is currently based on the node's **module membership**.
Displaying the top **4%** strongest connections (capped to enable rendering).

Click to view: Degree | Betweenness Centrality | Clustering | Modularity

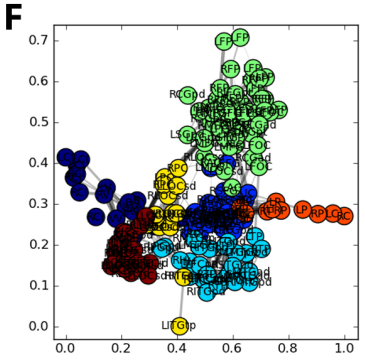

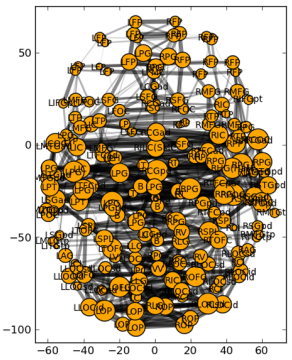

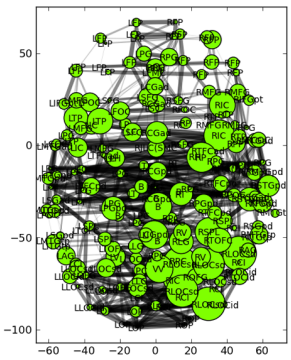

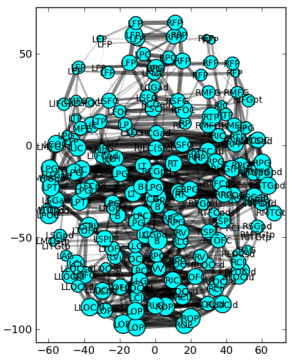

Figure 4: The appearance of the UMCD report based on the analysis of the NKI fcMRI group-average network, thresholded at 5% with weighted edges. A) The meta-information on the network and the global network metrics, including basic edge statistics, graph theory measures, and edge length measures, B) the connectivity matrix after thresholding, C) the region report, listing the graph theory measures for each node, D) the bar plot of node degree for each node, E) the interactive 3D network rendering from a top view with node color indicating module membership, F) 2D network plot with nodes laid out using the Fruchterman-Reingold force-directed algorithm, with node color indicating module membership, G) the 2D network plot from the top/axial view, with node radius indicating node degree, H) 2D network plot with node radius indicating betweenness centrality, I) 2D network plot with node radius indicating clustering coefficient.

Meta-information for the network that has been analyzed appears at the top of the page and includes the Atlas (i.e. parcellation scheme), Imaging Modality, Subject Pool, Group Size, Age Range, Preprocessing Notes, and Funding Information. Next, a table displays the following Global Network Metrics: the Raw Connection Density (%), the Chosen Density (%), Characteristic Path Length, Mean Clustering Coefficient, Number of Components, Global Efficiency, Modularity (Q), and the small world attributes Gamma, Lambda, and Sigma. Each metric contains a tooltip with a brief description and a link to the NetworkX function used to calculate the measure or the reference from which the formula was taken. For a more complete description of the graph measures calculated on the UMCD, the reader is referred to (Bullmore and Sporns, 2009), (Rubinov and Sporns, 2010), and (Sporns, 2010). For each edge in the raw and thresholded networks, the edge weight mean and standard deviation are shown, along with the edge Euclidean length mean and standard deviations.

The report contains a link to “View Regional Report” where the following nodal network measures appear in a table: full region name, degree, clustering coefficient, betweenness centrality, module membership, regional efficiency, and participation coefficient. These measures can also be downloaded by clicking “Download Regional Measures as .txt” which links to a tab-delimited text file containing all of these metrics. This file can be easily loaded into Matlab or other statistical software in order to perform offline statistical analysis.

The network analysis report includes both three-dimensional and two-dimensional visualizations. The 3D network view is an interactive rendered ball-and-stick model of the network implemented using WebGL (**Figure 2**). The rendering engine is a modified version of the ChemDoodle Web Components javascript library (http://web.chemdoodle.com). The center of mass for each node in the network appears as a sphere whose radius corresponds to the specific network metric that is selected: degree, betweenness centrality, clustering coefficient, regional efficiency, or participation coefficient**.** For modularity, all radii are equal and the node color indicates module membership. Each non-zero connection in the network is shown as a cylinder directly connecting the two nodes, whose radius is constant (= 1) for a binary network analysis and is scaled for a weighted analysis. The number of displayed edges is capped in order to allow smooth rendering in the browser. Equivalent 2D figures are displayed for the same set of network measures, where again the node radius corresponds to the specific measure and the edge width corresponds to edge weight. For each 2D network measure, a bar graph shows the sorted distribution of values for each node in the network.

The analysis also produces figures depicting the thresholded CM with a color bar corresponding to the range of weights in the network. The report displays the distribution of node degrees in the network in the Node Degree Histogram, which simply bins the degree of each node in the network. Another representation of the network is shown in the Spring Embedded Plot. This diagram collapses the connectivity structure of the network into two dimensions, where each node's "nearness" to each other node is based on the degree of connectivity between them, based on the Fruchterman-Reingold force-directed algorithm implemented in NetworkX. Nodes that are in the same module have the same color.

In order to compare two networks side by side, the user selects the networks on the Compare Networks page. After the two networks have been selected, the same set of options from the Analyze Network page – Weighting Scheme and % of edges to include – must be

specified for each network. Once the analysis is run, the same set of measures from the single network analysis are computed for each network. The results are displayed side by side.

Users assess the impact of a virtual lesion on a network using the Lesion a Brain Network page. Once a network is selected, the user presses 'Get Regions' in order to display a checklist of all the brain regions in the given network. Any region that is checked will be 'lesioned', meaning that all of the connections to this node from any other node in the network will be set to zero. The unlesioned and lesioned networks will then be analyzed and the results will be presented side by side in the exact same fashion as the Compare Networks results page.

Data sharing

Users share connectivity matrices on the Upload New Data page **(Figure 2)**. To share data, the following are required: 1) Study Name, a succinct identifier for the location/purpose of the study, e.g. UCLA_ICBM, 2) Network Name, a succinct name for individual matrix to be uploaded, e.g. CONTROL_grpmean, 3) the uploader's email address, 4) Region Names File, a text file listing the full name of each brain region in the network on separate lines, 5) Region Names Abbreviations File, a text file listing the abbreviated name of each region on separate lines, 6) Region XYZ Centers File, a text file with (X,Y,Z) coordinate for each region (preferably based on mm coordinates in MNI152 space), 7) Connectivity Matrix File, a tab-delimited text file containing the network CM, 8) Imaging Modality, and 9) Share, the sharing status of the data, which can be public (viewable and downloadable by any site visitor) or private (viewable only by the sharer of the data when they are logged in). Other requested meta-information includes the Scanner Device, Scan Parameters, Age Range Minimum and Maximum (the same for an individual subject, different for a group average), Gender, Subject Pool, Group Size, Preprocessing Notes, and Funding Source. Optional fields are also provided for specific imaging parameters for Magnetic Resonance (MR; field strength, MR TR, MR TE, MR Voxel Size, MR Field of View) and data processing steps for fMRI (Motion Correction, Skull Stripping, Temporal

Filtering, Spatial Smoothing, Slice Timing Correction, Intensity Normalization, EPI Unwarping, CSF Signal Regression, White Matter Signal Regression, Global Signal Regression), dwMRI (Number of Directions, Maximum b Value, Eddy Correction, Skull Stripping, Deterministic Tractography, Probabilistic Tractography), and structural MRI (sMRI; Skull Stripping, Intensity Normalization).

Data can be shared either for one network at a time or for a set of matrices. In the case of a batch upload, the entries for each of the four required text files simply needs to be stacked vertically for as many networks as will be uploaded. For example, if the network size was 100x100, the CM text file for six networks would be 600 rows by 100 columns. For the region names, region abbreviations, and region coordinates files, the list simply needs to be repeated as many times as there are networks. When performing a batch upload, the meta-information need only be entered once and all of the data can be uploaded with a single entry.

Users search for data on the UMCD using the Browse All Data page **(Figure 3)**. Each publicly shared network appears as a row where each column lists a different field describing that entry, as was specified on the Upload Data page when the data was shared. If a user has shared any data privately and is logged in, those data entries will also appear. The user may sort any column by clicking on the column header, allowing the user to group data by imaging modality or study name, for example. A search box allows the user to enter any term and dynamically display only the rows that contain that term, allowing rapid location of a dataset of interest. Any row has an option to View/Download, linking to an individual “profile” page for the network including the study and network name, the study and subject information, and links to download the raw CM **(Figure 5)**.

Id:	3032
Study Name:	UCLA_Autism
Network Name:	ASD102_rsfMRI
Atlas:	PowerNeuron_264
Region Names Full File:	file
Region Names Abbrev File:	file
Region Xyz Centers File:	file
Connectivity Matrix File:	file
Imaging Modality:	fMRI
Share:	Public
Scanner Device:	Siemens 3T Trio
Scan Parameters:	6 minutes resting state, TR=3s, TE=28ms, 3x3x4mm voxels
Age Range Min:	11.81
Age Range Max:	11.81
Gender:	Male
Subject Pool:	Autism Spectrum Disorder
Group Size:	1
Preprocessing Notes:	Motion correction, brain extraction, bandpass filtering (.1-.01Hz), regression motion parameters, motion spikes, WM, CSF, global signals. Extraction of timeseries from regions in transformed to subject native space
Funding Source:	NICHD grant P50 HD055784 (S.Y.B), NIMH grants R01 HD06528001 (S.Y.B), T32 GM008044 (J.D.R), T32 MH073526-05 (J.D.R), NIH grants (RR12169, RR13642, and RR00865) and Autism Speaks

Number of times analyzed:	31
Last time analyzed:	2012-05-10 13:05
Number of times downloaded:	2
Last time downloaded:	2012-04-23 17:58
Shared by:	rudie [AT] ucla [DOT] edu

Figure 5: The profile page for an individual connectivity matrix. All of the parameters specified by the sharer of the data appears on this page. The connectivity matrix and associated files (region names/abbreviations/XYZ centers) can be downloaded by clicking the 'file' links. The number of times the network has been analyzed or downloaded by any user of the site are also shown.

If the user is logged in and accessing data they shared, they can also edit or delete the entry on this page. The profile page for each network also shows the number of times the network has been analyzed or downloaded, as a measure of interest the community has in this dataset. On the Browse Data page, each entry also has an Analyze link, which will take the user to the Analyze page with the form prefilled to run the analysis for this network.

Users who wish to download all of the metadata or data for a study can do so on the Browse Studies page. The user downloads the metadata for a study as either a Comma

Separated Value (CSV) or Javascript Object Notation (JSON) file using a URL of the format http://humanconnectomeproject.org/get_study_metadata.<filetype>/<studyname> where 'filetype' is one of *csv* or *json* and 'studyname' is the study name provided by the individual who shared the data. The user downloads the connectivity matrices for a given study in a zip file, along with the region names, abbreviations, and XYZ centers, by accessing the URL http://humanconnectomeproject.org/get_study_data/<studyname>.

At the time of writing, the UMCD has 2155 publicly available CMs. These include 1003 functional connectivity MRI (fcMRI) matrices from the 1000 Functional Connectomes sample (Biswal et al., 2010), 522 fcMRI matrices from the ADHD200 sample (http://fcon_1000.projects.nitrc.org/indi/adhd200), 189 DTI matrices from the International Consortium for Brain Mapping dataset (http://www.loni.ucla.edu/ICBM), 175 fcMRI/DTI matrices from a study of autistic children (Rudie et al., under review), 55 DTI matrices from a study of aging and genetic risk for Alzheimer's Disease (Brown et al., 2011), the 392 fcMRI/DTI matrices from the Nathan Kline Institute/Rockland sample on the International Neuroimaging Data-Sharing Initiative site (INDI; including the 60 subjects in the 26-45 age range and another 136 subjects outside that range, from 4-85), and a small set of other miscellaneous contributions. All currently available matrices have largely complete metadata including subject demographics, scan parameters, and preprocessing notes. All currently available fMRI matrices are based on Pearson correlation of regional timeseries and all DTI matrices are based on tensor-based deterministic tractography. We anticipate that fMRI and dwMRI matrices from more diverse processing streams will eventually be shared on the site.

Interface with Neuroscience Information Framework

In order to facilitate the search of connectivity for specific brain regions in data shared on the UMCD, it is important to interface with various catalogs and wider scope data sharing initiatives. The Neuroscience Information Framework (NIF; http://neuinfo.org) is a project supported by the

Blueprint for Neuroscience Research, a pan-NIH initiative with a stated goal of facilitating data discovery and sharing among scientists (Gardner et al., 2008). The NIF works with database partners to gather relevant data and facilitate its' discovery by making data searchable via the user interface and web services. Since September of 2011, public UMCD data has been included in the NIF data index with brain region names aligned to NIF terminology. In order to compensate for brain region naming heterogeneity, regional name synonyms are aligned with the NIF standard ontology (NIFSTD). These data are searchable as a part of the NIF pan-mammalian brain connectivity data set. The human MRI functional/structural connectivity can be viewed alongside rodent and monkey connectivity data (http://neuinfo.org/nif/nifgwt.html?query=nlx_83091). To keep data up to date, NIF 'crawls' the UMCD and to find new data on a monthly basis, and curators are prompted to evaluate new data as changes are detected. The current portal and web services are hit more than a million times a month, increasing the possibility of users discovering UMCD data.

Guidelines for Data Sharing and Analysis

Data Description and Connectivity Matrix Derivation

To create a connectivity database that can maximize the research and clinical utility of the contributed data, it is essential to first define a set of best practices for deriving CMs. This section will discuss the procedure for deriving CMs from different neuroimaging modalities and the methodological issues that need to be addressed. We will limit the discussion to MRI modalities. For any MRI data shared on the UMCD, the parameters of the scan should be entered in the MR-specific fields and additional details should be noted in the *Scan Parameters* field on the Upload Data page (http://umcd.humanconnectomeproject.org/upload**)**. This generally includes the magnetic field strength, repeat time (TR), echo time (TE), scan duration, field of view, voxel resolution, slice thickness/gap, and other modality-specific factors.

fMRI Preprocessing

When sharing fMRI-derived connectivity matrices on the UMCD, the user should list check boxes for all included preprocessing steps in the fMRI-specific fields and details should be noted in the *Preprocessing Notes* field. fMRI-specific preprocessing steps include motion correction, linear detrending, smoothing, statistical removal of nuisance variables from white matter, CSF and whole brain signal, and bandpass filtering. For each step, the user should also include which software program was used (FSL, SPM, AFNI, in house, etc.). Although preprocessing methods differ between laboratories, the UMCD does not enforce strict criteria regarding data processing in the interest of remaining open to a maximal number of contributions. Instead, the responsibility is placed with the contributor to ensure that their shared data has been carefully processed, and equally with the site user to use their own discretion for assessing data quality.

When a subject performs a task during fMRI, networks are known to reconfigure to some degree based on the specific cognitive demands of the task (Shirer et al., 2012) (Mennes et al., 2012) (Bassett et al., 2011b). When task-based functional connectivity matrices are submitted to the UMCD, they should be annotated with a description of the task design and the cognitive processes that the experimenter expected to engage.

Diffusion-Weighted MRI Preprocessing

When sharing dwMRI-derived CMs on the UMCD, the user should specify the scan type as DTI, HARDI (High Angular Resolution Diffusion Imaging), or DSI (Diffusion Spectrum Imaging). In the dwMRI-specific fields, the user should note the number of gradient directions included in the scan sequence along with the maximum *b* value, whether eddy correction was performed, and the tractography method (deterministic or probabilistic). In the *Preprocessing Notes*, the user should describe the software package used and preprocessing details including whether multiple dwMRI scans were acquired and averaged, how diffusion tensors/orientation

distribution functions were calculated, the tractography algorithm, any voxelwise masking criteria, and the maximal angular threshold allowed for fibers to turn between adjacent voxels.

Parcellation Scheme/Choice of Atlas

In order to obtain connection strengths between brain regions, the regions must first be defined. This task typically takes one of several routes. Structural parcellation takes a structural image and parcellates it with an algorithm that uses anatomical information in the image and prior models to determine cortical and subcortical regional boundaries. Common analysis packages for performing parcellation are Freesurfer (http://surfer.nmr.mgh.harvard.edu) and Automated Anatomical Labeling (AAL) (Tzourio-Mazoyer et al., 2002). Functional parcellation algorithms performed on fMRI data search for regions whose functional connectivity patterns are statistically similar in time and/or space (Craddock et al., 2012). A third strategy is to use predefined subregions of cortex/subcortex from a predefined atlas such as the Harvard-Oxford cortical/subcortical probabilistic atlas distributed with the FMRIB Software Library (FSL). The set of ROIs are normally spatially registered to the subject's image space where connectivity is to be estimated. A fourth strategy is to use a set of meta-analytically defined coordinates in a standard stereotactic space (e.g. MNI152) based on sites of peak activation during behavioral tasks. Small regions of interest, typically spheres of 5-10mm radius, are created around each coordinate and used as seeds to calculate connectivity strength with the remaining spheres (Power et al., 2011). For any parcellation scheme, different tissue types may be included or excluded. fMRI-based analyses are typically uninterested in white matter signal and may use gray matter ROIs. Conversely, dwMRI studies are more focused on water diffusion in white matter and often use the gray/white matter interface as a starting point for tractography. In this case, ROIs may include portions of both gray and white matter. For atlas-based ROIs, region boundaries are commonly defined using probabilistic estimates rather than hard cutoffs. In this case, the user must decide a probability threshold above which to assign regional labels.

For submission to the UMCD, the user should note the atlas/software package used to parcellate the brain in the *Atlas* field and any masking operation that was performed for each ROI in the Preprocessing Notes field (e.g. gray matter, white matter, probability threshold). For each ROI, the (x, y, z) spatial coordinate describing its spatial location is also required in order to generate network renderings. The spatial center of mass is an ideal descriptive coordinate for an ROI. Users are strongly encouraged to use millimeter coordinates based in the Montreal Neurological Institute coordinate system after registering their ROIs to the MNI152 average brain. This is not strictly enforced and caution is warranted for any site user planning to compare connectivity loci across different datasets on the UMCD.

General Connectivity Matrix Preprocessing

Once a CM has been calculated, there are a variety of post-processing strategies that are specific to different imaging modalities, software packages, and laboratories. We urge those who share data on the UMCD to submit "raw" CMs. This precludes thresholding of edge weights below a certain weight cutoff, binarization of edges, or adjustment of weights to deal with issues of non-normal distribution and negative weights. Additionally, all current UMCD analyses assume that CMs are symmetric, meaning that the connection weight from node *i* to *j* is identical to the connection weight from *j* to *i*. The storage of raw data is necessary for subsequent downloaders of the data to make their own decisions about how to treat the data.

General Connectivity Matrix Analysis

The only options the user can configure when running an analysis on the UMCD are the weighting scheme and the edge density. All graph measures calculated by the UMCD are interpretable for binary and weighted graphs. While the various arguments for using binary or weighted edges are beyond the scope of this paper, it is generally helpful to test both options when analyzing a network in order to see how different graph metrics will vary. The selected

edge density will also affect the resultant graph metrics. At very low edge densities the network is likely to become disconnected, in which case path length-based measures like characteristic path length and lambda cannot be calculated for the graph as a whole. Other measures like global efficiency, clustering coefficient, and modularity can be calculated for disconnected graphs. From an analysis perspective, previous work considers sparse graphs (with <= ~25% of edges connected) to have higher "signal to noise" ratio (Alexander-Bloch et al., 2010), preserving only the strongest connections in the network. On the other hand, because the choice of threshold is arbitrary, any chosen threshold may exclude some edges that correspond to true biological connections. Thus, it is important to assess graph metrics across a range of different thresholds to ensure that they are not an artifact of one specific threshold value. For these reasons, users are encouraged to test different permutations of weighting schemes and thresholds to assess how network characteristics may vary.

There are important caveats with a general analysis pipeline like the UMCD. A graph is a very general representation of connectivity strengths in a network model of a system like the brain. Graphs derived from different types of data, such as fMRI and DTI-based graphs, may be more appropriate for certain network measures than others. For example, in functional graphs the edge weights are described based on a statistic, often the correlation coefficient. In this case, path length-based measures such as global efficiency may not be as meaningful as they are in a structural network, where the method determines physical connection densities. The UMCD does not attempt to stratify the networks based on the type of data from which they were derived. It will provide the same complete set of graph theory measures for any analysis. Additionally, most of the graph theory metrics calculated on the UMCD are "unnormalized" with respect to a random network. The only metrics that are calculated as ratios of the true network value to the "pseudo" value from a randomly wired network are gamma (normalized clustering coefficient) and lambda (normalized characteristic path length). Caution is urged to the user in interpreting graph measures to ensure they are used appropriately.

Connectivity Matrix Comparison

In order to compare CMs across studies in a meaningful way, all factors of each study's data collection and analysis must be considered. The imaging modality, scanner, scan sequence, subject pool, and analysis methods will all obviously impact the CM. The regional names used for a given study will also be unique, dependent on the parcellation scheme or atlas that was used to define ROIs. In any attempt to compare CMs from different studies, the user should consider how similar the regions from the studies are. This is a two-pronged issue: first, the spatial position and extent of the ROIs may differ; second, the nomenclature may differ. The UMCD only requests a name and spatial coordinate for each ROI. This is an incomplete description, based on a practical design decision to reduce file storage size and complexity. However, this means that the similarity of ROIs across studies cannot be fully assessed. Each ROI is uploaded with its MNI stereotaxic coordinate, which can establish a coarse measure of spatial similarity in ROI coordinates across studies. The spacing of the full set of coordinates for a given CM can give an idea of the density and average size of each ROI, assuming ROIs are not overlapping. In order to find studies that have connectivity estimates for a given region, the user is encouraged use the NIF interface to the UMCD. There, a user could search for the inferior frontal gyrus, pars triangularis, or Brodmann Area 45, and obtain the same results based on their alignment in the NIFSTD. A more systematic attempt to maximally align all regional names from two different studies is outside the scope of the current work but has been addressed elsewhere (Imam et al., 2012) (Bug et al., 2008). Of course, full alignment of ROIs may not be possible if the studies differ in the number of regions, the size of the defined regions, or the set of regions that are excluded (e.g. subcortical nuclei). For all of these reasons, the user must carefully consider how comparable two datasets are, and carry this in mind when comparing data from different studies shared on the UMCD.

Example Analysis

Here we perform an analysis based on publicly available DTI and rs-fMRI data from 60 subjects that were part of the NKI/Rockland study available for download on INDI (http://fcon_1000.projects.nitrc.org/indi/pro/nki.html).

Subjects

The purpose of this study was to generate a large scale, extensively phenotyped dataset to explore brain/behavior relationships in healthy individuals. For the current study, we were interested in comparing functional and structural brain networks in healthy adults. We selected 60 subjects from this sample for analysis, ranging in age from 26-45 years, mean=35.8 +/- 6.3. 37 males and 23 females were included. Subjects underwent diagnostic psychiatric interviews, along with a battery of psychiatric, cognitive, and behavioral assessments. Full-scale intelligence quotient (FSIQ) was measured with the Wechsler Abbreviated Scale of Intelligence. The mean subject FSIQ was 104.1 +/- 12.5.

MRI Scans

Resting state fMRI was performed on a Siemens Trio 3T with acquisition time=10:55, TR=2500ms, TE=30ms, on 38 slices with a voxel size=3mm^3. Diffusion tensor imaging had acquisition time=13:32, TR=10000ms, TE=91ms, on 58 slices with a voxel size=2mm^3 along 64 diffusion-weighted gradients with b=1000s/mm^2. A magnetization prepared rapid gradient echo (MPRAGE) scan had either a longer sequence with acquisition time=10:42, TR=2500ms, TE=3.5ms on 192 slices with a voxel size=1mm^3 or a shorter sequence with acquisition time=5:49, TR=2500ms, TE=3.5ms, on 192 slices with voxel size=1mm^3. The raw data for these scans was accessed from http://fcon_1000.projects.nitrc.org/indi/pro/nki.html.

rs-fMRI/DTI Processing

Resting state fMRI data was preprocessed using the following pipeline: 1) corrected for differential slice timing using FMRIB Software Library's (FSL) slicetimer, 2) rigid-body motion corrected each volume to the middle volume using FSL Motion Correction using FMRIB's Linear Image Registration Tool (MCFLIRT), 3) stripped the skull using FSL Brain Extraction Tool (BET), 4) spatially smoothed the data with a Gaussian kernel with 5mm full-width half maximum, 5) grand-mean scaled the entire 4D dataset, 6) band pass temporal filtered the data from .08-.009Hz, 7) performed tissue-type segmentation of the MPRAGE using FSL FAST, 8) registered cerebrospinal fluid (CSF) and white matter (WM) masks to the first fMRI volume, 9) mask the CSF and WM masks with conservative ventricular and core white matter masks derived from the MNI152 atlas, 10) extracted mean timeseries from the core CSF, core WM, and whole brain, 11) constructed a model that included timeseries for core CSF, core WM, whole brain signal, the six motion parameters, and all temporal derivatives, performed linear regression with this model on the data, and obtained the residuals, 12) ran motion scrubbing to identify TRs with a relative motion displacement greater than 0.5mm or a relative BOLD signal intensity change greater than .5% (Power et al., 2012), and 13) registered with FSL FLIRT to the MNI152 average brain with a $4mm^3$ voxel resolution in a three stage registration from fMRI > initial T2 structural > MPRAGE > MNI152. The residual BOLD data was then analyzed using the spatially constrained spectral clustering method (Craddock et al., 2012) in order to derive 188 gray matter/subcortical/cerebellar ROIs that were spatially contiguous and maximally functionally homogenous across subjects. These ROIs ranged in volume from 28-180 voxels. No subjects had more than 100 TRs flagged by motion scrubbing and thus none were dropped from subsequent analysis. An average of 9 +/- 17 TRs were flagged for removal. After marking flagged TRs, the mean timeseries for each ROI was calculated and then correlated with all remaining ROI timeseries (excluding flagged TRs) to derive a 188x188 functional connectivity MRI (fcMRI) matrix.

DTI data was corrected for motion and eddy current distortions using FSL eddy_correct. The skull was stripped using FSL BET. Diffusion tensors were estimated using Diffusion Toolkit (http://trackvis.org/blog/tag/diffusion-toolkit/) and tractography was run using the fiber assignment by continuous tracking (FACT) algorithm (Mori and Van Zijl, 2002), with an angle threshold of 45 degrees. The fractional anisotropy (FA) map for each subject was registered to the MNI152 average brain in a two-stage registration from FA to MPRAGE using a mutual information cost function and 7 degrees of freedom, then from MPRAGE to MNI152 using a correlation ratio cost function and 12 degrees of freedom. The transformation matrices were combined and inverted. We then registered the 188 ROIs defined from the fMRI data in standard space to each subject's DTI space. Masks were dilated by one voxel width in order to include the gray/white matter interface, and then thresholded in order to assign each voxel to only the ROI for which it had the highest intensity value (greatest likelihood of membership). For each ROI, all fibers were counted that intersected at least one voxel in the source ROI and at least one voxel in any target ROI using custom code (http://ccn.ucla.edu/wiki/index.php/UCLA_Multimodal_Connectivity_Package). In this way the 188x188 structural CM was obtained.

Function/Structure Weight Comparisons

Connection weights for functional and structural networks were correlated with each other across subjects using Matlab (The Mathworks, Natick, MA) in order to determine network similarity.

Graph Theory

All 120 matrices (60 functional + 60 structural) were uploaded to the UMCD. The individual networks are publicly shared on the site under the study name 'NKI_Rockland.' The network names are in the format 'NKI_<subject_id>_<modality>', e.g. 'NKI_1013090_fcmri' and

'NKI_1013090_dti.' For all fcMRI matrices, we also sought to examine the effect of global signal regression (GSR) on functional network topography and similarity to structural networks. GSR is a controversial step in fcMRI preprocessing. Proponents argue that this step controls for common, non-brain sources of variation that affect the entire image (Fox et al., 2009), while opponents have shown that this step may obscure the distribution of connectivity weights and introduce artifactual anticorrelations between networks (Murphy et al., 2009) (Saad et al., 2012). We therefore prepared a parallel set of CMs that were processed in identical fashion but without the GSR step. These matrices are labeled as, e.g. 'NKI_1013090_fcmri_NoGSR.' From these individual matrices, group-average functional and structural matrices were calculated. These group average matrices increase the stability of connectivity estimates between regions for a relatively homogenous group from a developmental/aging standpoint. The rationale was that individuals in the 26-45 age range are fully mature but have not yet experienced cognitive aging, placing them in the maximally "normal" adult age range. The group averages are named 'NKI_fcmri_avg_<age_range_min>_<age_range_max>' and 'NKI_dti_avg_<age_range_min>_<age_range_max>'. Finally, in order to test the affect of global signal regression on the resultant networks, equivalent functional connectivity matrices without the global signal regression stepped are stored under the name 'NKI_fcmri_avg_<age_range_min>_<age_range_max>_NoGSR'.

For the current study, the goal was to demonstrate the capacity of the UMCD to compare functional and structural CMs. Hence, only the NKI_dti_avg_26_45, NKI_fcmri_avg_26_45_GSR, and NKI_fcmri_avg_NoGSR matrices were analyzed. They are henceforth referred to as NKI_dti_avg, NKI_fcmri_avg_GSR, and NKI_fcmri_avg_NoGSR. These matrices were analyzed at two different edge density levels, 5% and 20%. The 5% threshold created sparser matrices that preserved only the strongest edges and highlighted different network modules. The DTI network was disconnected at a 5% threshold, preventing the computation of characteristic path length and small worldness. At the 20% threshold, all

networks were fully connected, allowing the computation of global path length-based measures. Matrices were also analyzed with two different weighting schemes, binary and weighted. For functional networks, edge weights spanned a range of -1 to 1, as dictated by the Pearson correlation formula. For structural networks, the fiber connection weights spanned four orders of magnitude (10^0-10^4). In cases like these where the distribution of weights for different matrices are significantly different, the binarization of network weights can significantly obscure the underlying connectivity patterns. However, binarization has advantages, including simpler graph theory calculations and a more straightforward randomization scheme (degree preserving rewiring) for determining null reference networks. We therefore found it pertinent to examine both weighted and binarized functional and structural networks.

Each matrix was analyzed and all global/regional measures were downloaded from the UMCD and imported to Matlab. The adjusted Rand index was used to quantify the similarity of modularity partitions in individual functional vs. structural networks, where 0 indicates no agreement between nodes and 1 indicates total agreement between all nodes.

Results

Basic Graph Properties

First, the similarity of functional and structural connection weights was assessed by Pearson correlation. For the NKI_fcmri_avg_GSR and NKI_dti_avg CMs, the edge weight correlation was r=.39 (all $p < 10^{-5}$; **Figure 6**). When only considering regions with existent structural connections (> 1 fiber, averaged across the group), the edge weight correlation increased to r=.42. For the NKI_fcmri_avg_NoGSR and NKI_dti_avg, the edge weight correlation was r=.30 considering all connections. When limiting to only existent structural connections, the correlation increased slightly to r=.34.

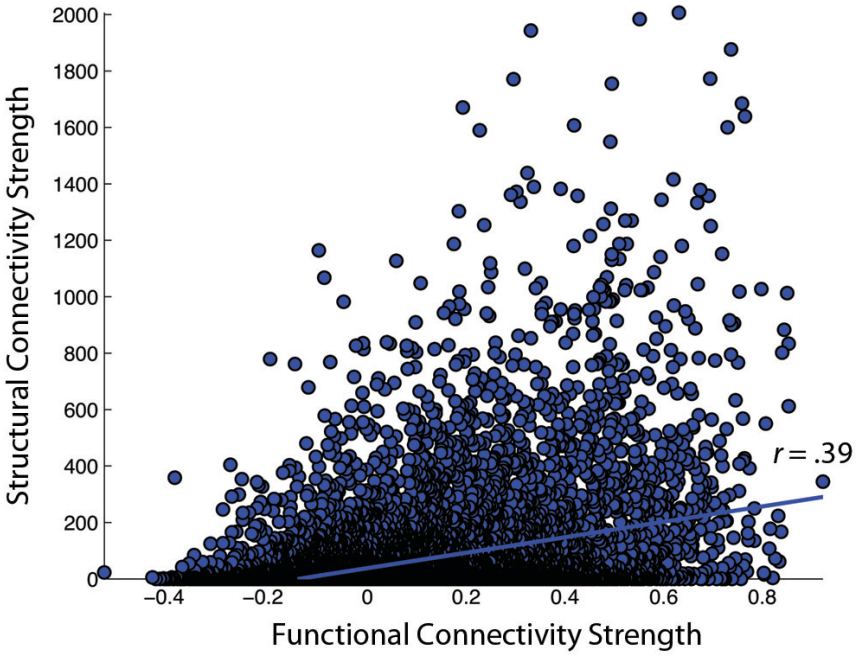

Figure 6: A) Correlation of functional and structural connectivity strengths for the group-average 188x188 connectivity matrices, identified as NKI_fcmri_avg_GSR and NKI_dti_avg in the text.

Global Graph Theory Measures

Next, the fcMRI and DTI networks were compared to one another using UMCD's 'Compare Networks' feature. The raw NKI_fcmri_avg_GSR network was 100% connected with an average edge weight of .017 +/- .199 (**Table 1**). The average Euclidean distance between ROI coordinates was 83.5 +/- 30.7mm. The raw NKI_fcmri_avg_NoGSR network was also 100% connected, with a higher average edge weight of .28 +/- .17, as expected. The average Euclidean distance between ROIs was exactly the same as the GSR network, given that every ROI is connected in the raw CMs. The raw NKI_dti_avg network was 76.04% connected with an average edge weight of 56.56 +/- 156.10 and an average Euclidean distance of 76.85 +/- 29.94mm.

Network measures were assessed with binary edges at an edge density of 20% (**Table 1**). The networks differed from each other for nearly every metric. The measures are listed here in the format (fcMRI GSR/NoGSR vs. DTI). The fcMRI network had greater characteristic path

length (CPL; 2.00/2.06 vs. 1.96), lower clustering coefficient (CC; .57/.57 vs. .62), equivalent global efficiency (GE; .57/.56 vs .57), higher small worldness for GSR (2.42/1.71 vs. 1.81), higher gamma for GSR (2.72/1.92 vs. 1.95), higher lambda (1.12/1.12 vs. 1.08), and higher modularity (Q; .47/.39 vs .33).

Measure	NKI_fcmri_avg_GSR	NKI_fcmri_avg_NoGSR	NKI_dti_avg
Raw Density	100%	100%	76.04%
Raw Edge Weights	.017 +/- .199	.28 _/- .17	56.56 +/- 156.10
Raw Euclidean distance	83.5 +/- 30.7mm	83.5 +/- 30.7mm	76.85 +/- 29.94mm
Thresholded Edge Weights	.33 +/- 14	.54 +/- .1	204.52 +/- 249.66
Thresholded Euclidean distance	59.55 +/- 30.41mm	61.19 +/- 29.84mm	50.43 +/- 22.74mm
CPL	2.00	2.06	1.96
MCC	.57	.57	.62
eGlob	.57	.56	.57
Modularity	.47	.39	.33
Small worldness	2.43	1.71	1.81
Gamma	2.72	1.92	1.95
Lambda	1.12	1.12	1.08

Table 1: Basic network and global graph theory properties for the fcMRI networks with/without Global Signal Regression and the DTI network.

Nodal Graph Theory Properties

For the nodal measures, the Pearson correlations between functional and structural measures were calculated across the 188 nodes (**Table 2**). For binarized networks thresholded at 20%, the correlations were significant at a p-level of .01 for betweenness centrality (r=.19, p=.008) and participation coefficient (r=-.2, p=.005) and nearly significant for clustering coefficient (r=.18, p=.016), though the betweenness result was driven by outliers. The correlation was not significant for strength (r=-.06, p=.45) or regional efficiency (r=-.05, p=.54). For comparison, nodal measures were also correlated between the functional and structural networks for binary networks thresholded at 5% and weighted networks thresholded at 5% and

20% (**Table 2**). Each of the measures were also compared using the Spearman rank correlation. In no cases was the Spearman correlation coefficient substantially different from the Pearson correlation coefficient (mean difference in r: .015).

	Binary, 5%	**Binary, 20%**	**Weighted, 5%**	**Weighted, 20%**
Strength	-.02 (.83)	-.06 (.45)	-.02 (.83)	-.06 (.45)
Clustering Coefficient	.09 (.2)	.18 (.016)	.12 (.11)	.11 (.12)
Betweenness Centrality	.15 (.036)	.19 (.008)*	.14 (.06)	.15 (.04)
Regional Efficiency	-.01 (.91)	-.05 (.54)	-.1 (.15)	-.01 (.93)
Participation Coefficient	.15 (.04)	-.2 (.005)*	.15 (.04)	.04 (.6)
Adjusted Rand index	.19	.09	.19	.12

Table 2: Correlation of nodal fcMRI and DTI graph theory measures across all 188 nodes for the NKI_fcmri_avg_GSR and NKI_dti_avg networks. Values are mean r-value (p-value) except for the Rand index. * indicates significance at $p < .01$.

A side-by-side visual comparison of the networks revealed the fcMRI network had more bilateral connectivity (**Figure 7 and 8**), particularly in the motor and visual cortices. The average length of edges between nodes, as measured by Euclidean distance, was longer in the fcMRI network than the DTI network **(Table 1)**. The nodes with the highest "hubness", based on the combined rank of strength, betweenness centrality, and regional efficiency are shown in **Table 3**.

The functional network with GSR exhibited hubs in the temporal lobe, cingulate cortex, parietal lobe, and cerebellum. Without GSR, hubs were more apparent in occipital and temporal lobes. Structural hubs were found in the subcortical areas (thalamus, caudate, putamen, pallidum), medial temporal lobe, and insula.

fcMRI w/ global signal regression, Binary 20%	**fcMRI w/out global signal regression, Binary 20%**	**DTI, Binary 20%**
Right planum polare	Left temporal occipital	Left thalamus

	fusiform gyrus	
Right precuneus	Right temporal occipital fusiform gyrus	Right pallidum
Cerebellum vermis VI	Right anterior cingulate	Right thalamus
Right anterior middle temporal gyrus	Left occipital fusiform gyrus	Left pallidum
Right posterior parahippocampal gyrus	Right temporal pole	Left posterior parahippocampal gyrus
Left posterior cingulate	Right precuneus	Right putamen
Right anterior cingulate	Right superior lateral occipital cortex	Right posterior parahippocampal gyrus
Left posterior middle temporal	Right temporooccipital inferior temporal gyrus	Left insula
Right paracingulate	Right posterior superior temporal gyrus	Left caudate
Right posterior superior temporal gyrus	Right planum polare	Right hippocampus

Table 3: Regions with the highest combined rank for node strength, betweenness centrality, and regional efficiency, based on fcMRI/DTI networks binarized and thresholded to keep the 20% strongest edges.

The strength, betweenness centrality, and modularity of each node for the NKI_fcmri_avg_GSR and NKI_dti networks, weighted and thresholded at 4% for visualization purposes, are displayed visually on the 2D network in **Figure 7**. fcMRI network nodes with high strength and betweenness centrality were spatially distributed while in the DTI network they tended to cluster in the subcortical nodes. The fcMRI modules corresponded to well characterized functional systems including the default mode network (turquoise), temporal lobe network (blue), fronto-parietal network (light blue), dorsal and ventral sensory-motor networks (blue and seafoam green), visual network (yellow), posterior parietal network (orange), subcortical network (line green), and cerebellar network (dark blue) (Power et al., 2011) (Tomasi and Volkow, 2011) (**Figure 8**). DTI modules corresponded to neighboring anatomical regions including the frontal lobe/anterior midline (blue), left temporal lobe/parietal lobe/subcortex (seaform green), right temporal lobe/parietal lobe (blue), right central midline/sensory-motor cortex/cingulate cortex (turquoise), occipital lobe/right posterior parietal/temporal lobe (light blue), and cerebellum (dark blue).

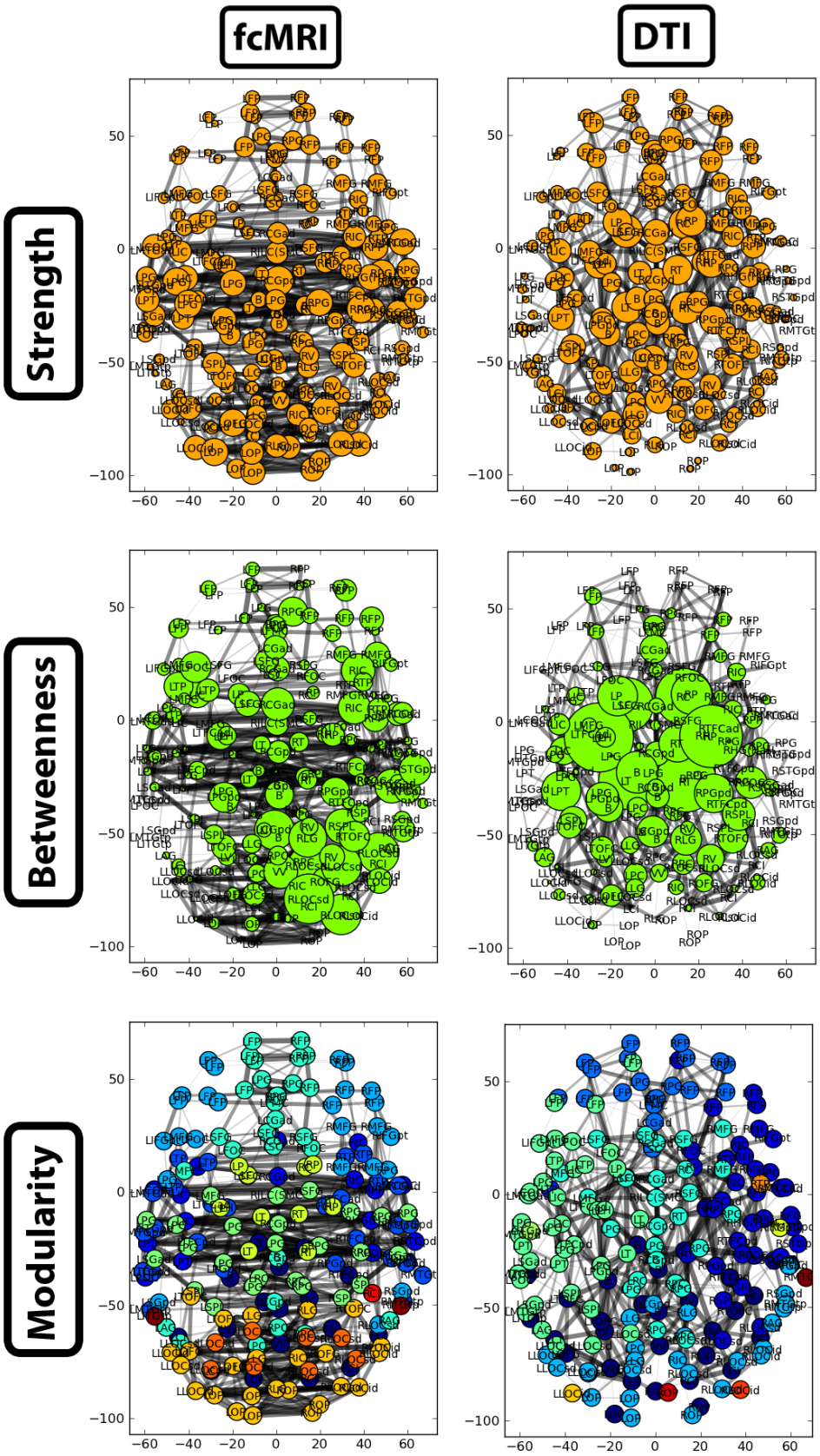
fcMRI
DTI
Strength
Betweenness
Modularity

Figure 7: Two-dimensional network plots from fcMRI and DTI group average networks. Networks are viewed from a top/axial view with edge width proportional to connection strength and node radius/color related to the given network measure. For each network, the top 4% of weighted edges based on strength are shown. In the first row, the radius of each node is based on its connection strength. In the second row, the radius of each node is based on its betweenness centrality. The third row shows nodes grouped into different modules by color.

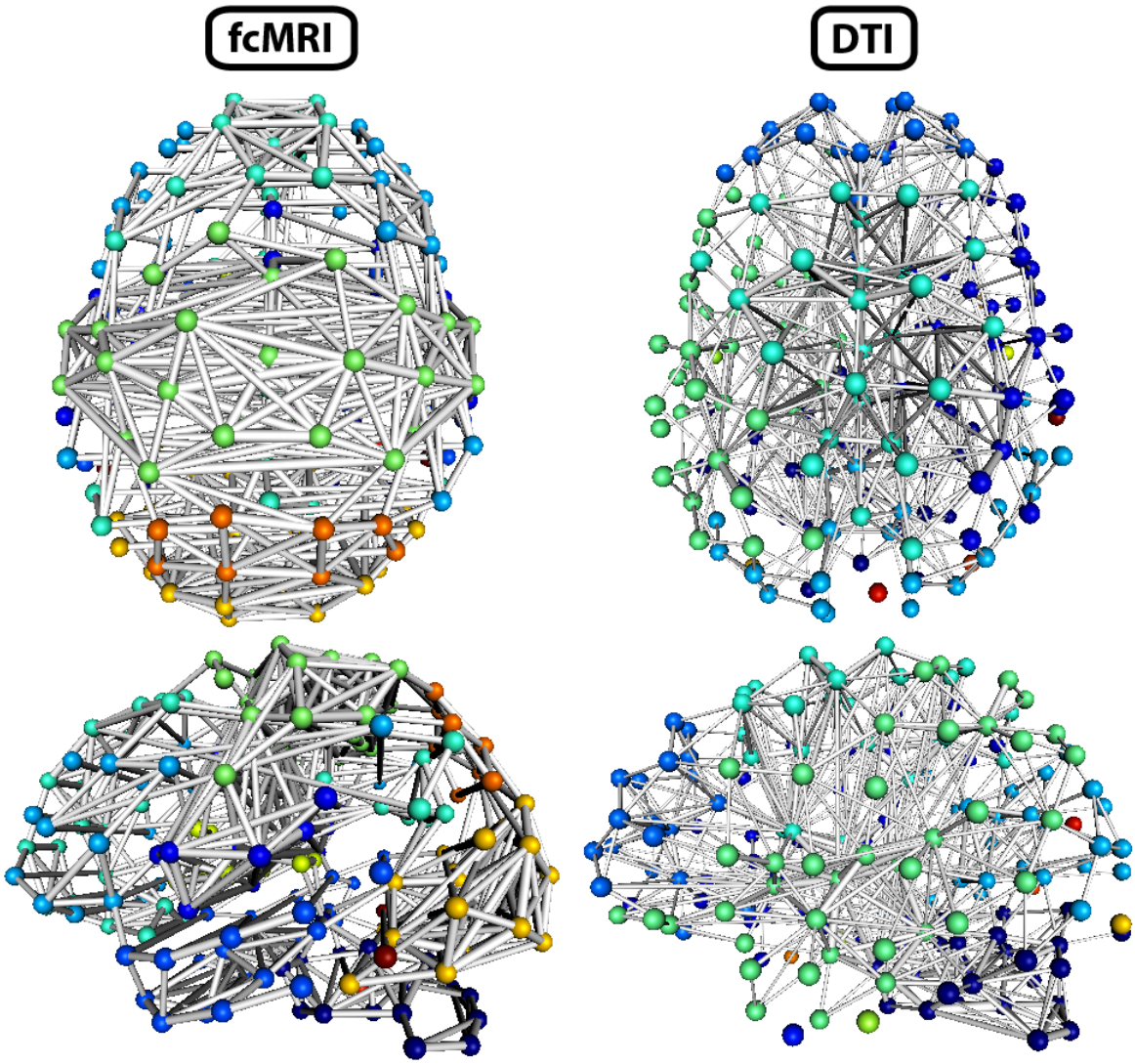

Figure 8: Three-dimensional network renderings of the fcMRI and DTI group average networks, thresholded to show the top 4% of weighted edges based on connection strength. Node colors are based on module membership. The same networks are shown from a top view and a left side view. The fcMRI network shows modules agreeing with known functional networks, longer edge Euclidean lengths, and more bilateral connectivity. The DTI network shows more anatomically confined modules, shorter edge Euclidean lengths, and more local connectivity.

Discussion

Data Sharing and Neuroinformatics

The UMCD allows any user to publicly share brain connectivity matrices, run graph theory-based analyses on the website, and search available data across any imaging modality, demographic category, or disease status. The ability to archive these data in their complete form and make them publicly available should enable more extensive brain connectivity meta-analyses. Here we illustrated the capability of the UMCD to compare functional (fMRI) and structural (DTI) CMs derived from the same set of subjects in order to assess similarities and differences in their connectivity patterns.

The UMCD decreases the barrier to entry for performing a graph-theory based analysis of a CM. We emphasize that this platform is not primarily designed for statistical analysis. It is first and foremost a data sharing site. We provide graph theory based tools to allow users to explore and compare CMs of interest on the site. While we consider the richness of this environment to be beneficial, caution is warranted in the application and interpretation of graph theory measures from UMCD. As with any software package that provides quantitative data metrics, users are urged to thoroughly consider how these measures were calculated and whether they are appropriate to compare across individual, imaging modality, or study.

MRI-based connectivity analyses offer hope in improving the ability of a clinician to diagnose a neurological disease or neuropsychiatric disorder. In order to achieve accurate diagnosis of individual patients, sensitivity and specificity of classification must be pushed to extremely high levels (Pepe et al., 2004). One obvious way to improve classification accuracy is to increase the number of training samples. Community-driven repositories are an effective strategy for rapidly aggregating large amounts of data from the international community (Van Horn et al., 2004) (Milham, 2012). These repositories have already been leveraged to build neuroimaging-based classifiers of neuropsychiatric disorders such as Attention Deficit

Hyperactive Disorder and evaluate their efficacy (Cheng et al., 2012; Colby et al., 2012; Eloyan et al., 2012). A downside of this strategy is the increased likelihood of data with suspect quality. While users are encouraged to share data on the UMCD only after publication, this is not strictly enforced. We leave the accessors of the data the responsibility of vetting data that they analyze on the UMCD or download for off-site use.

One aim of the neuroinformatics field is the integration of databases with one another into large federations (Akil et al., 2011). These efforts are dependent on the establishment of ontologies and the use of application programming interfaces (APIs). The Neuroscience Information Framework (NIF) is a semantic search engine that allows a user to search a broad set of databases spanning many species, recording methods, and laboratories (Gupta et al., 2008). The UMCD connectivity data are regularly crawled by NIF as they are uploaded to the system, using the region names associated with each shared CM. This allows a NIF user to perform a connectivity-based meta-analysis at a broader scale. This is a challenging task because data from the various source databases catalogued by NIF are often customized to a particular technique and a particular species, rather than across species and techniques. While mapping Brodmann areas to corresponding cortical structures in rodents may be an ill-posed problem, even simple differences such as “cornu ammonis 1” versus “Hippocampal region, CA1” present a problem when comparing connectivity measures in different datasets. Note, these are two perfectly valid ways to describe the CA1 region and yet no computer will be able to find these terms together because they are not lexical variants unless the computer is told that these are in fact synonyms. Therefore, NIF superficially aligns brain region labels to the NIF standard ontology, the NIFSTD, where labels can be toggled for search and browsing. NIF also performs a search across all known synonyms per brain region, as it is unlikely that all data will be aligned at any one time. If users wish to investigate connectivity for a specific brain region based on data in the UMCD, they should first perform a search on the NIF system for that

region. Once relevant datasets have been identified, they can use the UMCD to further probe the connectivity of their region of interest in those datasets.

Comparison of Functional and Structural Connectivity Matrices

As a demonstration of the UMCD platform, we compared group-averaged functional and structural connectivity matrices from a group of 60 healthy subjects aged 26-45. Functional and structural graph theory-based studies have expanded in parallel in recent neuroimaging literature. Several studies have made direct comparisons of connectivity strengths in rs-fMRI and dwMRI data (Hagmann et al., 2008; Honey et al., 2009) but to our knowledge, none have systematically compared graph-theory based measures. We found that despite a positive correlation of functional and structural connectivity strengths, there was a low correspondence of global and nodal graph theory measures. For the connection weights of fcMRI and DTI networks, the correlation was moderate but statistically significant. The fcMRI network had greater characteristic path length (CPL; 2.00/2.06 vs. 1.96), lower clustering coefficient (CC; .57/.57 vs. .62), equivalent global efficiency (GE; .57/.56 vs .57), higher small worldness for GSR (2.42/1.71 vs. 1.81), higher gamma for GSR (2.72/1.92 vs. 1.95), higher lambda (1.12/1.12 vs. 1.08), and higher modularity (Q; .47/.39 vs .33). The differences in modularity highlight the differences between these networks. The higher modularity in the fcMRI networks relates to the longer path length, as fcMRI networks are more spatially distributed. The DTI network has a more regular, lattice-like topology. Importantly, global signal regression exaggerates the differences between the fcMRI and DTI networks. Modularity and small worldness both increase drastically in fcMRI data with GSR applied, exaggerating the differences in global graph theory measures to between the fcMRI and DTI networks. This step may enhance within-module correlations while dampening between-module correlations. Surprisingly, the weight correlations for the fcMRI and DTI networks were more similar with GSR applied. Thus, while individual

functional and structural weights are more similar after GSR, global network properties become more dissimilar.

DTI and fMRI have their own limitations for determining connectivity strengths. A tensor is a basic model of water diffusion that is insufficiently complex for describing the intersection of multiple fiber populations within a voxel (Wedeen et al., 2008). DTI tractography therefore has limited ability to detect crossing fibers. Alternative diffusion weighted imaging methods like DSI collect data with more gradient directions and larger b-values. This enables the modeling of diffusion as a more complex Orientation Distribution Function (ODF), which can better resolve the intravoxel crossing of fiber bundles. The corpus callosum can be difficult to fully resolve using DTI because of its crossing with the heavily myelinated corona radiata. Here we derived connectivity matrices from DTI tractography and thus may have slightly underestimated interhemispheric connectivity. Meanwhile, rs-fMRI functional connectivity robustly detects bilaterally symmetric functional connections (e.g. Damoiseaux et al., 2006). Future studies with DTI data, DSI data, and resting state fMRI data will be required to determine how variable the DTI/DSI interhemispheric connectivity measures are, and how these both relate to rs-fMRI connectivity strengths.

The comparison of nodal measures from functional and structural networks revealed mostly non-significant correlations. Importantly, the relationship tended to be non-significant regardless of the weighting scheme or weight threshold, suggesting that these factors do not highly influence the network measures. The only significant finding was a negative correlation of nodal participation coefficients in binary networks at a 20% weight threshold. In order to probe the relationship deeper, we examined the effects of all structural regional measures – degree, clustering, betweenness, regional efficiency, and participation – on functional participation using hierarchical regression. The most significant model for predicting functional participation included structural clustering ($p=3.15 \times 10^{-6}$) and participation (2.61×10^{-7}), both with negative coefficients. Thus, for binarized graphs thresholded at 20%, low structural diversity and sparse

local connectivity related to higher functional diversity. A structural “connector” region is one that is sparsely connected and bridges between different areas of the network. In these networks, structural connector regions tended to functionally interact with multiple different functional modules.

Functional and structural modules had a low degree of correspondence in these networks. One explanation for the disparity between these network types is simply that brain structure and function are not isomorphic (Deco et al., 2011). While the structural connective backbone does provide the scaffolding upon which neuronal communication occurs, it may not substantially constrain the functional integration and segregation of brain networks. Structural fiber connections do exist between most intrinsic functional connectivity networks (Van den Heuvel et al., 2009a) but such connections do not necessarily imply a similar community structure. Resting state functional connectivity patterns have relatively high test-retest reliability across sessions, indicative of a stable resting state configuration (Shehzad et al., 2009). However, it has been demonstrated that nodes of the brain’s functional network exhibit characteristic macroscale reconfigurations in the service of motor tasks (Bassett et al., 2011b), visual perception (Ekman et al., 2012), and episodic memory (Shirer et al., 2012). It appears that certain brain regions may be more predisposed for task-related adaptation while others maintain more stable roles maintaining intrinsic connectivity (Mennes et al., 2012). Meanwhile, the brain’s structural macroscale connectivity is known to be largely static and reproducible on short timescales (days to weeks) (Bassett et al., 2011a) (Cammoun et al., 2012). The presence of an adaptive functional network on a static structural scaffold obviously indicates some divergence of structural and functional network properties. The aggregation of functional connectivity matrices across resting state and different tasks, when collected in parallel with structural connectivity matrices, should further our understanding of the constraints that structural connectivity places on functional integration and segregation.

Conclusion

Here we introduced the UCLA Multimodal Connectivity Database, a web-based resource that is openly available for brain network analysis and data sharing. Within this framework, a user can share CMs derived from neuroimaging data or access the matrices that have been publicly shared by other users. The site allows the user to conduct a graph theory analysis of any shared CM and view a report of global and nodal graph theory metrics, 3D and 2D network visualizations, along with study/demographic information about the network. We hope that this website will encourage broader sharing of CMs, enabling large-scale meta-analyses of brain connectivity.

Acknowledgements

The UMCD is hosted by the Laboratory of Neuroimaging (LONI) at UCLA, in affiliation with the MGH-UCLA Human Connectome Project (HCP). Thanks to Joe Franco for assistance with the hosting of the UMCD. Thanks to Jonathan Cachat for assistance with NIF integration. Edward Lau and Mike Durnhofer provided valuable technical assistance in earlier stages of hosting. Tessa Harrison provided valuable comments on the manuscript. The work was supported by NIH NRSA F31AG035438-01 to JAB and NIH Neuroscience Blueprint HHSN271200800035C via NIDA.

Chapter 5 References

Akil, H., Martone, M. E., and Van Essen, D. C. (2011). Challenges and Opportunities in Mining Neuroscience Data. *Science* 331, 708–712.

Alexander-Bloch, A. F., Gogtay, N., Meunier, D., Birn, R., Clasen, L., Lalonde, F., Lenroot, R., Giedd, J., and Bullmore, E. T. (2010). Disrupted Modularity and Local Connectivity of Brain Functional Networks in Childhood-Onset Schizophrenia. *Front Syst Neurosci* 4.

Bassett, D. S., Brown, J. A., Deshpande, V., Carlson, J. M., and Grafton, S. T. (2011a). Conserved and variable architecture of human white matter connectivity. *NeuroImage* 54, 1262–1279.

Bassett, D. S., Wymbs, N. F., Porter, M. A., Mucha, P. J., Carlson, J. M., and Grafton, S. T. (2011b). Dynamic reconfiguration of human brain networks during learning. *Proc. Natl. Acad. Sci. U.S.A.* 108, 7641–7646.

Biswal, B. B., Mennes, M., Zuo, X.-N., Gohel, S., Kelly, C., Smith, S. M., Beckmann, C. F., Adelstein, J. S., Buckner, R. L., Colcombe, S., et al. (2010). Toward discovery science of human brain function. *Proc. Natl. Acad. Sci. U.S.A.* 107, 4734–4739.

Brown, J. A., Terashima, K. H., Burggren, A. C., Ercoli, L. M., Miller, K. J., Small, G. W., and Bookheimer, S. Y. (2011). Brain network local interconnectivity loss in aging APOE-4 allele carriers. *Proc. Natl. Acad. Sci. U.S.A.* 108, 20760–20765.

Buckner, R. L., Sepulcre, J., Talukdar, T., Krienen, F. M., Liu, H., Hedden, T., Andrews-Hanna, J. R., Sperling, R. A., and Johnson, K. A. (2009). Cortical Hubs Revealed by Intrinsic Functional Connectivity: Mapping, Assessment of Stability, and Relation to Alzheimer's Disease. *J. Neurosci.* 29, 1860–1873.

Bug, W. J., Ascoli, G. A., Grethe, J. S., Gupta, A., Fennema-Notestine, C., Laird, A. R., Larson, S. D., Rubin, D., Shepherd, G. M., Turner, J. A., et al. (2008). The NIFSTD and BIRNLex Vocabularies: Building Comprehensive Ontologies for Neuroscience. *Neuroinformatics* 6, 175–194.

Bullmore, E., and Sporns, O. (2009). Complex brain networks: graph theoretical analysis of structural and functional systems. *Nat Rev Neurosci* 10, 186–98.

Cammoun, L., Gigandet, X., Meskaldji, D., Thiran, J. P., Sporns, O., Do, K. Q., Maeder, P., Meuli, R., and Hagmann, P. (2012). Mapping the human connectome at multiple scales with diffusion spectrum MRI. *Journal of Neuroscience Methods* 203, 386–397.

Cheng, W., Ji, X., Zhang, J., and Feng, J. (2012). Individual classification of ADHD patients by integrating multiscale neuroimaging markers and advanced pattern recognition techniques. *Front. Syst. Neurosci* 6, 58.

Colby, J. B., Rudie, J. D., Brown, J. A., Douglas, P. K., Cohen, M. S., and Shehzad, Z. (2012). Insights into multimodal imaging classification of ADHD. *Front. Syst. Neurosci* 6, 59.

Craddock, R. C., Holtzheimer, P. E., 3rd, Hu, X. P., and Mayberg, H. S. (2009). Disease state prediction from resting state functional connectivity. *Magn Reson Med* 62, 1619–1628.

Craddock, R. C., James, G. A., Holtzheimer, P. E., 3rd, Hu, X. P., and Mayberg, H. S. (2012). A whole brain fMRI atlas generated via spatially constrained spectral clustering. *Hum Brain Mapp* 33, 1914–1928.

Damoiseaux, J. S., Rombouts, S. a. R. B., Barkhof, F., Scheltens, P., Stam, C. J., Smith, S. M., and Beckmann, C. F. (2006). Consistent resting-state networks across healthy subjects. *PNAS* 103, 13848–13853.

Deco, G., Jirsa, V. K., and McIntosh, A. R. (2011). Emerging concepts for the dynamical organization of resting-state activity in the brain. *Nat. Rev. Neurosci.* 12, 43–56.

Dosenbach, N. U. F., Nardos, B., Cohen, A. L., Fair, D. A., Power, J. D., Church, J. A., Nelson, S. M., Wig, G. S., Vogel, A. C., Lessov-Schlaggar, C. N., et al. (2010). Prediction of Individual Brain Maturity Using fMRI. *Science* 329, 1358 –1361.

Ekman, M., Derrfuss, J., Tittgemeyer, M., and Fiebach, C. J. (2012). Predicting errors from reconfiguration patterns in human brain networks. *PNAS* 109, 16714–16719.
Eloyan, A., Muschelli, J., Nebel, M. B., Han, F., Zhao, T., Barber, A. D., Pekar, J. J., Mostofsky, S. H., and Caffo, B. (2012). Automated diagnoses of attention deficit hyperactive disorder using magnetic resonance imaging. *Front. Syst. Neurosci* 6, 61.
Fox, M. D., Zhang, D., Snyder, A. Z., and Raichle, M. E. (2009). The Global Signal and Observed Anticorrelated Resting State Brain Networks. *J Neurophysiol* 101, 3270–3283.
Fox, P. T., and Lancaster, J. L. (2002). Opinion: Mapping context and content: the BrainMap model. *Nat. Rev. Neurosci* 3, 319–321.
Gardner, D., Akil, H., Ascoli, G. A., Bowden, D. M., Bug, W., Donohue, D. E., Goldberg, D. H., Grafstein, B., Grethe, J. S., Gupta, A., et al. (2008). The neuroscience information framework: a data and knowledge environment for neuroscience. *Neuroinformatics* 6, 149–160.
Gupta, A., Bug, W., Marenco, L., Qian, X., Condit, C., Rangarajan, A., Müller, H. M., Miller, P. L., Sanders, B., Grethe, J. S., et al. (2008). Federated Access to Heterogeneous Information Resources in the Neuroscience Information Framework (NIF). *Neuroinformatics* 6, 205–217.
Hagmann, P., Cammoun, L., Gigandet, X., Meuli, R., Honey, C. J., Wedeen, V. J., and Sporns, O. (2008). Mapping the Structural Core of Human Cerebral Cortex. *PLoS Biology* 6, e159 EP –.
Hagmann, P., Sporns, O., Madan, N., Cammoun, L., Pienaar, R., Wedeen, V. J., Meuli, R., Thiran, J.-P., and Grant, P. E. (2010). White matter maturation reshapes structural connectivity in the late developing human brain. *Proceedings of the National Academy of Sciences* 107, 19067 –19072.
van den Heuvel, M. P., Mandl, R. C. W., Kahn, R. S., and Hulshoff Pol, H. E. (2009a). Functionally linked resting-state networks reflect the underlying structural connectivity architecture of the human brain. *Hum. Brain Mapp.* 30, 3127–3141.
van den Heuvel, M. P., Stam, C. J., Kahn, R. S., and Hulshoff Pol, H. E. (2009b). Efficiency of Functional Brain Networks and Intellectual Performance. *J. Neurosci.* 29, 7619–7624.
Honey, C. J., Kötter, R., Breakspear, M., and Sporns, O. (2007). Network Structure of Cerebral Cortex Shapes Functional Connectivity on Multiple Time Scales. *PNAS* 104, 10240–10245.
Honey, C. J., Sporns, O., Cammoun, L., Gigandet, X., Thiran, J. P., Meuli, R., and Hagmann, P. (2009). Predicting human resting-state functional connectivity from structural connectivity. *Proceedings of the National Academy of Sciences* 106, 2035–2040.
Imam, F. T., Larson, S. D., Bandrowski, A., Grethe, J. S., Gupta, A., and Martone, M. E. (2012). Development and use of Ontologies Inside the Neuroscience Information Framework: A Practical Approach. *Front Genet* 3, 111.
Laird, A. R., Lancaster, J. L., and Fox, P. T. (2005). BrainMap: the social evolution of a human brain mapping database. *Neuroinformatics* 3, 65–78.
Li, Y., Liu, Y., Li, J., Qin, W., Li, K., Yu, C., and Jiang, T. (2009). Brain Anatomical Network and Intelligence. *PLoS Comput Biol* 5, e1000395.
Lo, C.-Y., Wang, P.-N., Chou, K.-H., Wang, J., He, Y., and Lin, C.-P. (2010). Diffusion Tensor Tractography Reveals Abnormal Topological Organization in Structural Cortical Networks in Alzheimer's Disease. *J. Neurosci.* 30, 16876–16885.
Mennes, M., Kelly, C., Colcombe, S., Castellanos, F. X., and Milham, M. P. (2012). The Extrinsic and Intrinsic Functional Architectures of the Human Brain Are Not Equivalent. *Cerebral Cortex*. Advance Access published January 31, 2012. doi: 10.1093/cercor/bhs010
Milham, M. P. (2012). Open Neuroscience Solutions for the Connectome-wide Association Era. *Neuron* 73, 214–218.

Mori, S., and van Zijl, P. C. M. (2002). Fiber tracking: principles and strategies - a technical review. *NMR Biomed* 15, 468–480.
Murphy, K., Birn, R. M., Handwerker, D. A., Jones, T. B., and Bandettini, P. A. (2009). The impact of global signal regression on resting state correlations: are anti-correlated networks introduced? *Neuroimage* 44, 893–905.
Pepe, M. S., Janes, H., Longton, G., Leisenring, W., and Newcomb, P. (2004). Limitations of the Odds Ratio in Gauging the Performance of a Diagnostic, Prognostic, or Screening Marker. *Am. J. Epidemiol.* 159, 882–890.
Power, J. D., Barnes, K. A., Snyder, A. Z., Schlaggar, B. L., and Petersen, S. E. (2012). Spurious but systematic correlations in functional connectivity MRI networks arise from subject motion. *NeuroImage* 59, 2142–2154.
Power, J. D., Cohen, A. L., Nelson, S. M., Wig, G. S., Barnes, K. A., Church, J. A., Vogel, A. C., Laumann, T. O., Miezin, F. M., Schlaggar, B. L., et al. (2011). Functional Network Organization of the Human Brain. *Neuron* 72, 665–678.
Rubinov, M., and Sporns, O. (2010). Complex network measures of brain connectivity: uses and interpretations. *Neuroimage* 52, 1059–1069.
Saad, Z. S., Gotts, S. J., Murphy, K., Chen, G., Jo, H. J., Martin, A., and Cox, R. W. (2012). Trouble at Rest: How Correlation Patterns and Group Differences Become Distorted After Global Signal Regression. *Brain Connectivity* 2, 25–32.
Shehzad, Z., Kelly, A. M. C., Reiss, P. T., Gee, D. G., Gotimer, K., Uddin, L. Q., Lee, S. H., Margulies, D. S., Roy, A. K., Biswal, B. B., et al. (2009). The resting brain: unconstrained yet reliable. *Cereb. Cortex* 19, 2209–2229.
Shirer, W. R., Ryali, S., Rykhlevskaia, E., Menon, V., and Greicius, M. D. (2012). Decoding subject-driven cognitive states with whole-brain connectivity patterns. *Cereb. Cortex* 22, 158–165.
Sporns, O. (2010). *Networks of the Brain*. 1st ed. Cambridge: The MIT Press.
Sporns, O., Tononi, G., and Kötter, R. (2005). The Human Connectome: A Structural Description of the Human Brain. *PLoS Comput Biol* 1, e42.
Supekar, K., Menon, V., Rubin, D., Musen, M., and Greicius, M. D. (2008). Network analysis of intrinsic functional brain connectivity in Alzheimer's disease. *PLoS Comput. Biol* 4, e1000100.
Tomasi, D., and Volkow, N. D. (2011). Association between functional connectivity hubs and brain networks. *Cereb. Cortex* 21, 2003–2013.
Tzourio-Mazoyer, N., Landeau, B., Papathanassiou, D., Crivello, F., Etard, O., Delcroix, N., Mazoyer, B., and Joliot, M. (2002). Automated anatomical labeling of activations in SPM using a macroscopic anatomical parcellation of the MNI MRI single-subject brain. *Neuroimage* 15, 273–289.
Van Horn, J. D., Grafton, S. T., Rockmore, D., and Gazzaniga, M. S. (2004). Sharing neuroimaging studies of human cognition. *Nature Neuroscience* 7, 473–481.
Wedeen, V. J., Wang, R. P., Schmahmann, J. D., Benner, T., Tseng, W. Y. I., Dai, G., Pandya, D. N., Hagmann, P., D'Arceuil, H., and de Crespigny, A. J. (2008). Diffusion spectrum magnetic resonance imaging (DSI) tractography of crossing fibers. *NeuroImage* 41, 1267–1277.
Yan, C., Gong, G., Wang, J., Wang, D., Liu, D., Zhu, C., Chen, Z. J., Evans, A., Zang, Y., and He, Y. (2011). Sex- and Brain Size–Related Small-World Structural Cortical Networks in Young Adults: A DTI Tractography Study. *Cerebral Cortex* 21, 449 –458.

Chapter 6

Conclusion

This work has investigated the activity and connectivity of brain circuitry involved in episodic memory processing in individuals at genetic risk for Alzheimer's Disease and healthy young adults. In Chapter 2, we reported that decreases in local structural connectivity in cortical regions were accelerated in APOE-4 carriers and were statistically correlated with episodic memory retrieval scores. In Chapter 3, we found that APOE-4 carriers had reduced functional activity in the left entorhinal cortex (ERC) during associative episodic memory encoding. ERC activity was negatively correlated with whole brain modularity during the task. In Chapter 4, a study of healthy young adults found increased right hippocampal activity during successfully encoded face/place associations. The degree of right hippocampal functional connectivity increase after the task with higher-order visual and prefrontal regions was predictive of individual performance on a cued recognition memory task 24 hours after encoding. The structural connections binding these regions all traversed the parahippocampal gyrus. In Chapter 5, a web-based tool for connectivity analysis was used to show differences in the topology of whole brain structural and functional connectivity networks.

The motivation behind the study of structural networks in Chapter 2 was to pinpoint connectivity alterations that may occur between cortical areas or between cortical and sub-cortical areas. Hippocampal-cortical connectivity is of specific interest because AD-related impairments in episodic memory performance appear to be related to alterations in this circuitry (Salat et al., 2010). The hippocampus is known to functionally couple with the default mode network (Greicius et al., 2004), a set of brain regions that are critical for episodic memory encoding and retrieval (Andrews-Hanna et al., 2010; Kim et al., 2010). Cortico-cortical connectivity between regions of the default mode network is also critical for memory performance (Hampson et al., 2006) and degrades in AD (Damoiseaux et al., 2012a). Here we focus on connections 1) between cortical areas (anterior association, unimodal sensory, visual

and spatial, and posterior association), 2) between cortex and parahippocampal gyrus, 3) between parahippocampal gyrus (PHC) and entorhinal cortex, and 4) between entorhinal cortex and hippocampus (**Figure 1**). This model is a simplified version of that used by Libby and colleagues (Libby et al., 2012), which illustrates the convergence of cortical inputs in the PHC that then project to the ERC and finally to the hippocampus.

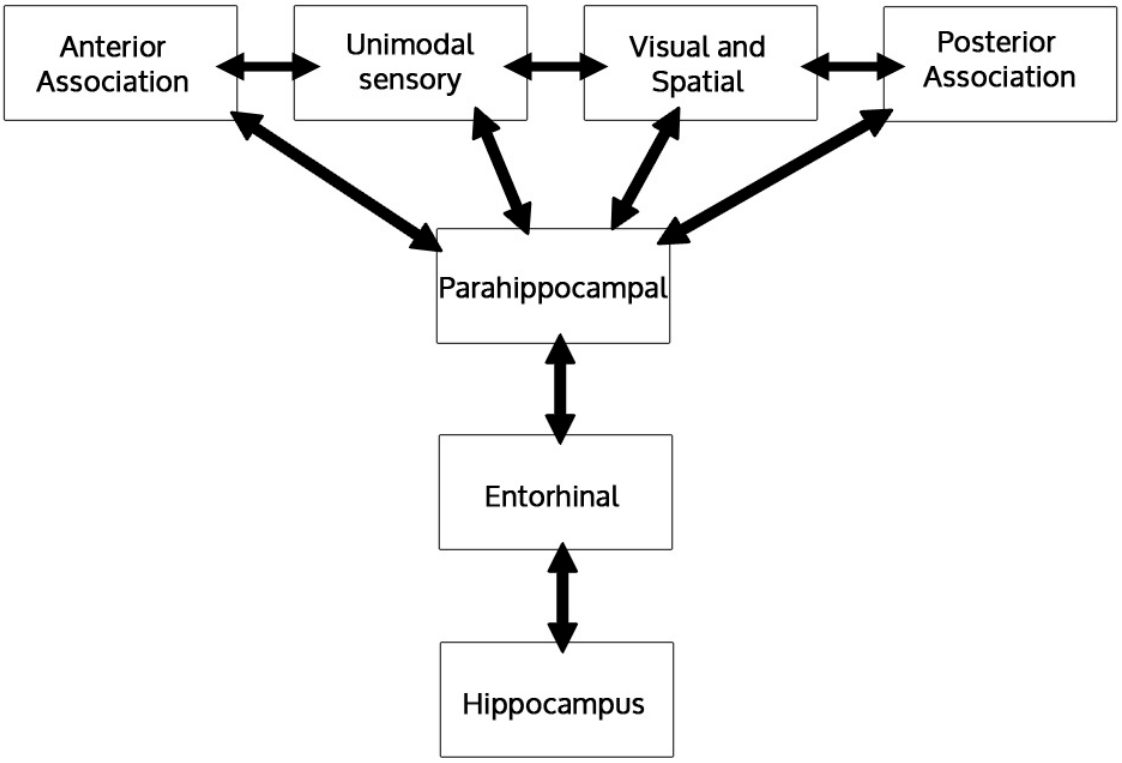

Figure 1: A model of cortical-cortical and cortico-hippocampal connectivity.

The connections that demonstrate significant negative correlations with age in APOE-4 carriers are primarily from anterior and posterior association areas (**Figure 2**). These regions include the precuneus, the orbitofrontal cortex, the supramarginal gyrus, and the inferior temporal gyrus. As discussed in Chapter 2, these regions have overlap with the default mode network. The detection of reduced local interconnectivity between these regions may relate to the differential connection patterns of these areas as opposed to medial temporal areas.

Cortical regions tend to have a large number of connections to other cortical regions (Hagmann et al., 2008), while medial temporal areas are more anatomically isolated (Squire et al., 2004). As clustering coefficient is a measure of connectivity among a node's first degree neighbors, it is likely to vary more for cortical regions that have a higher number of neighbors. Thus, this measure is likely to be more sensitive to alterations in cortico-cortical connectivity than cortico-hippocampal connectivity. Given that the changes in cortico-cortical connectivity tracked with changes in cognitive performance, clustering coefficient may be less of a leading indicator of cognitive alteration than other biomarkers like CSF AB, CSF tau, or hippocampal atrophy (Jack Jr et al., 2013).

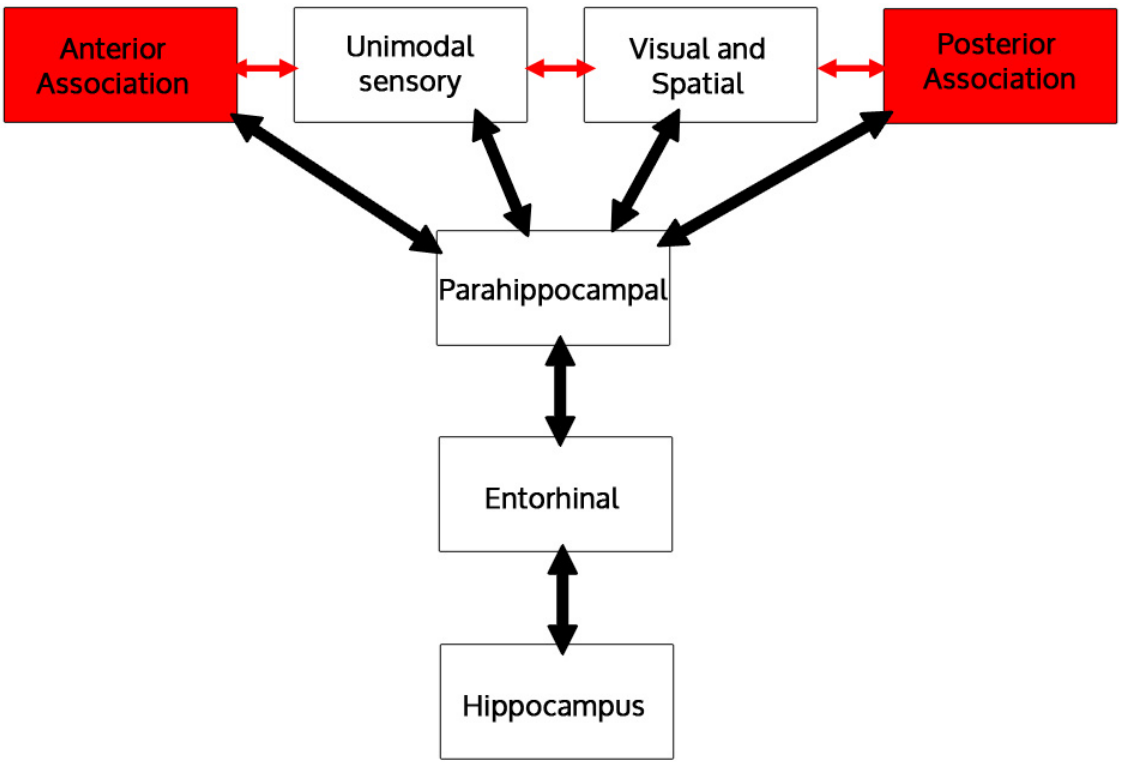

Figure 2: Alterations in structural local interconnectivity in aging APOE-4 carriers. Anterior association and posterior association regions (red boxes) in the cortex displayed more negative correlations of clustering coefficient and age for APOE-4 carriers. The connections between these areas and the remaining cortical areas (red arrows) predominantly contributed to this effect.

In Chapter 3, we reported decreased entorhinal cortical activity during associative episodic memory encoding in APOE-4 carriers. On an individual basis, the amount of whole-brain functional modularity negatively predicted the amount of entorhinal activity (**Figure 3**). In these whole-brain functional networks, lower modularity was related to higher global integration. There is evidence that effective performance of complex cognitive tasks requires greater global integration (Van den Heuvel et al., 2009b). It is conceivable that in individuals with reduced communication between functional brain networks (i.e. modules), reduced processing of task-related stimuli is occurring, leading to reduced engagement of the ERC.

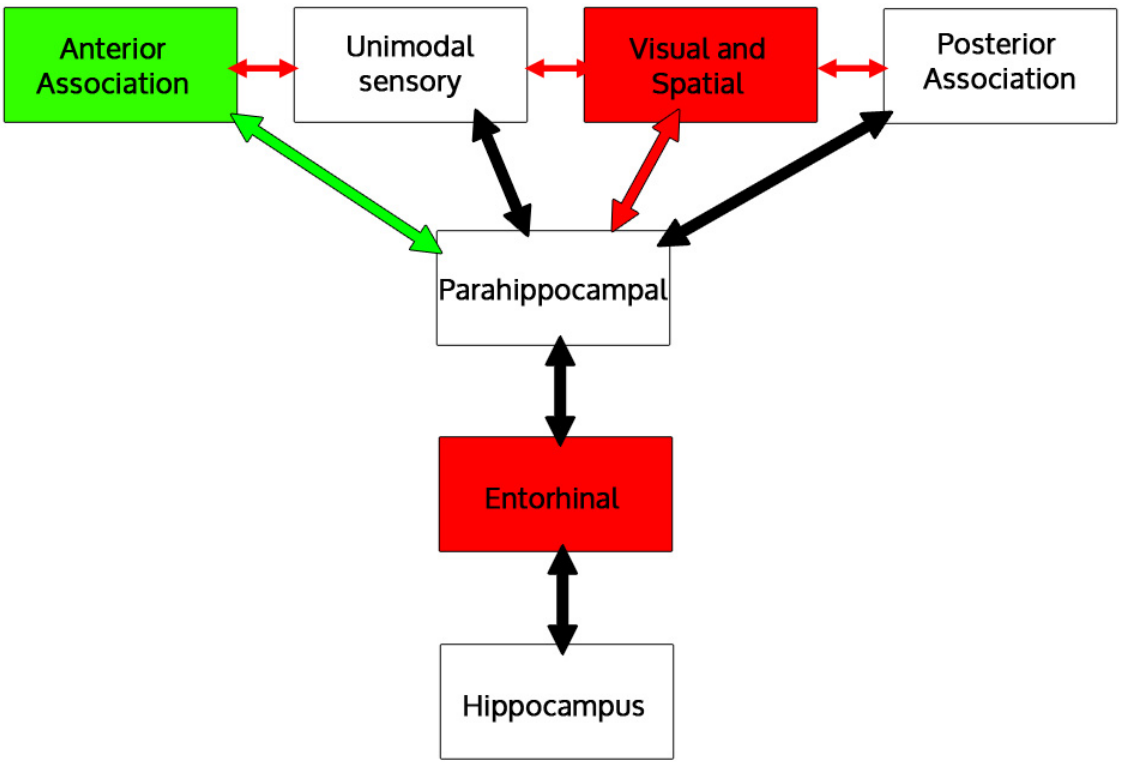

Figure 3: Alterations in regional activity and global functional connectivity during memory encoding. The entorhinal cortex (red box) demonstrated reduced activity in APOE-4 carriers. This effect was positively correlated with functional connectivity from visual/spatial cortical regions (red box and large red arrow) and negatively correlated with functional connectivity strength from anterior association cortical regions (green box and large green arrow). At a global level, increased modularity was predictive of decreased entorhinal activity, predominantly driven by a decreased number of intermodular cortico-cortical functional connections (small red arrows).

When region-specific functional connectivity of the ERC during encoding was assessed, one broad trend was evident: functional connectivity between visual/spatial areas and the ERC positively predicted ERC activity, while connectivity between the ERC and anterior association areas negatively predicted ERC activity. One interpretation of this result is that increased activity of the default mode network and coupling with task-specific regions may be more beneficial to task performance (Chadick and Gazzaley, 2011) and drive higher ERC activity. However, in APOE-4 carriers, decreased activity in the default mode network may occur simultaneously with a corresponding increase of activity in the salience network (Machulda MM, 2011) (Seeley WW, 2011). Increased salience activity may inhibit ERC activity, reducing the ability to encode new memories. Future work should examine the connectivity of the ERC with these functional brain networks during true resting state fMRI. This will help establish whether these connectivity alterations are intrinsic or are only evident during the performance of specific cognitive tasks. Given the simplicity of the memory task employed here, it is feasible to consider using it in a MRI-based biomarker assessment of AD risk.

In Chapter 5, we examined functional and structural connections of the hippocampus that enable episodic memory consolidation. AD is known to impair episodic memory performance in conjunction with hippocampal atrophy and structural isolation. We examined functional memory networks in order to clarify if specific brain regions are hubs in these networks in healthy individuals, and whether or not these regions converge with sites of known atrophy in AD. We designed a novel memory task called “Traveling with the Stars” that required

subjects to form a memory association between specific pairs of famous faces and famous places. They were given surprise memory tests 24 hours after memory encoding in order to assess memory consolidation as indexed by cued recognition performance. We found that during encoding, right hippocampal activity was higher for face/place pairs that were subsequently recognized versus those that were not (**Figure 4**). Previous studies have demonstrated predominant activation of the right hippocampus with respect to the left for pictorial versus verbal stimuli (Papanicolaou et al., 2002). The functional connectivity of the right hippocampus to the rest of the brain was examined both before and after the encoding task, in search of functional connectivity *changes* following a task that may predict the degree of individual memory performance. Indeed, increases in hippocampal functional connectivity to the fusiform gyrus, lingual gyrus, and orbitofrontal cortex were all positively correlated with the number of face/place pairs the subject correctly recognized. The fusiform and orbitofrontal cortex have both been previously implicated in the recognition of famous faces (Kanwisher et al., 1997) (Gorno-Tempini et al., 1998) while the lingual gyrus has demonstrated involvement in both face and place processing (Gorno-Tempini and Price, 2001). Functional connectivity changes in the idle moments following task are known to be related to immediate subsequent memory retrieval (Tambini et al., 2010) but here found that they are important for memory consolidation.

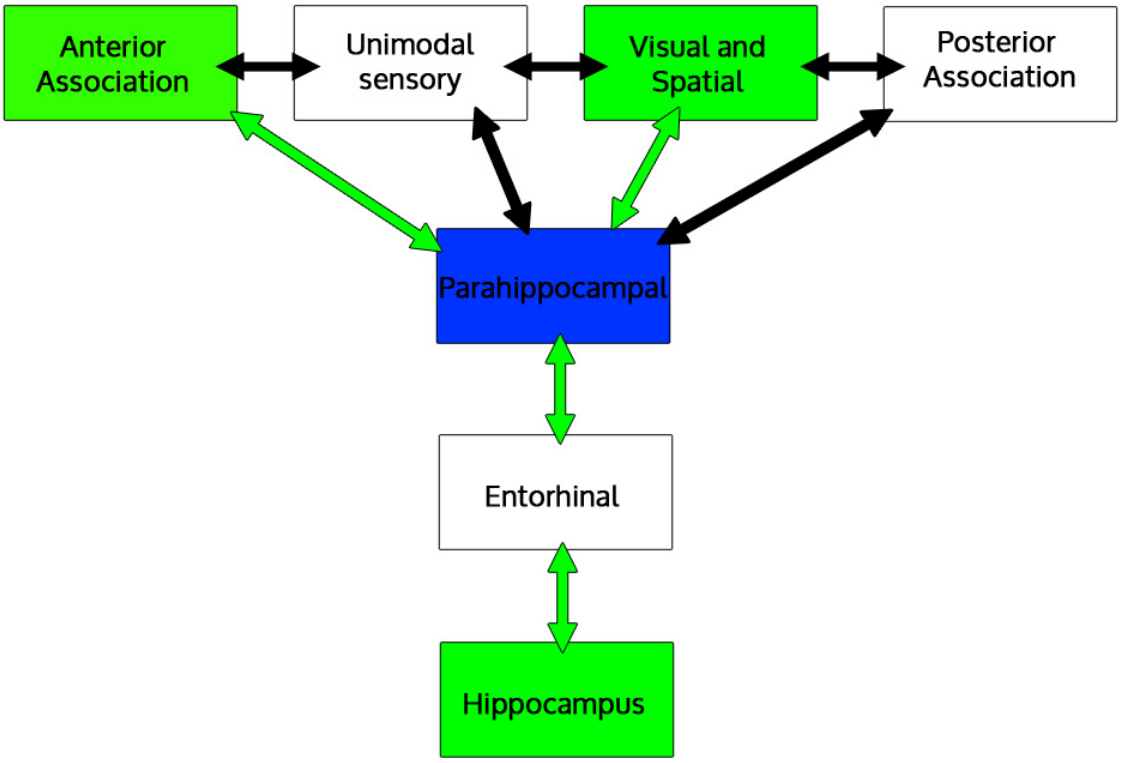

Figure 4: The episodic memory recognition consolidation network. During successfully encoded face/place memory associations, subjects demonstrated increased activity in the right hippocampus (green box). An assessment of post-task minus pre-task functional connectivity changes found that increased hippocampal connectivity to visual/spatial and anterior association areas (green boxes) predicted the level of individual memory performance on a cued recognition task administered 24 hours after encoding. The structural shortest-path connections of the hippocampus and associated cortical areas (green arrows) all traversed the parahippocampal gyrus (blue box).

We examined the structural connectivity of this “recognition consolidation” network diffusion spectrum imaging (DSI) tractography. Graph theory-based shortest path assessment of whole-brain structural connectivity networks revealed that all structural paths to the hippocampus traversed the parahippocampal gyrus. This agreed with the model specified in **Figure 4**. This provides evidence that in humans, anatomical cortical projections converge in the parahippocampal gyrus, similar to the pattern observed in non-human primates (Squire et al., 2004). Importantly, we did not detect any direct structural connections between the hippocampus and the other regions in the recognition consolidation network. Graph-theory based shortest-path calculation was required to detect the structural connectivity. We suggest

that future studies assessing relationships of structural and functional connectivity employ graph theory to triangulate networks of interest.

No specific relationship between individual variations in structural connection density of these regions and memory performance was detected. It is possible that functional variability within this network is more predictive of individual performance differences than structural variability. The hub-like nature of the parahippocampal gyrus in this network has relevance for AD and AD-risk. There is consistent evidence of white matter atrophy in the parahippocampal gyrus in older APOE-4 carriers (Honea et al., 2009; Persson et al., 2006; Ryan et al., 2011). The current findings suggest that alterations in episodic memory consolidation in prodromal AD may relate to reductions of the structural and functional connectivity of the parahippocampal gyrus with cortical regions.

Chapter 6 References

Andrews-Hanna, J.R., Reidler, J.S., Sepulcre, J., Poulin, R., Buckner, R.L., 2010. Functional-anatomic fractionation of the brain's default network. Neuron 65, 550–562.

Chadick, J.Z., Gazzaley, A., 2011. Differential coupling of visual cortex with default or frontal-parietal network based on goals. Nat Neurosci 14, 830–832.

Damoiseaux, J.S., Prater, K.E., Miller, B.L., Greicius, M.D., 2012. Functional connectivity tracks clinical deterioration in Alzheimer's disease. Neurobiology of Aging 33, 828.e19–828.e30.

Gorno-Tempini, M.L., Price, C.J., 2001. Identification of famous faces and buildings A functional neuroimaging study of semantically unique items. Brain 124, 2087–2097.

Gorno-Tempini, M.L., Price, C.J., Josephs, O., Vandenberghe, R., Cappa, S.F., Kapur, N., Frackowiak, R.S., Tempini, M.L., 1998. The neural systems sustaining face and proper-name processing. Brain 121, 2103–2118.

Greicius, M.D., Srivastava, G., Reiss, A.L., Menon, V., 2004. Default-mode network activity distinguishes Alzheimer's disease from healthy aging: Evidence from functional MRI. Proceedings of the National Academy of Sciences of the United States of America 101, 4637–4642.

Hagmann, P., Cammoun, L., Gigandet, X., Meuli, R., Honey, C.J., Wedeen, V.J., Sporns, O., 2008. Mapping the Structural Core of Human Cerebral Cortex. PLoS Biology 6, e159 EP –.

Hampson, M., Driesen, N.R., Skudlarski, P., Gore, J.C., Constable, R.T., 2006. Brain Connectivity Related to Working Memory Performance. The Journal of Neuroscience 26, 13338 –13343.

Honea, R.A., Vidoni, E., Harsha, A., Burns, J.M., 2009. Impact of APOE on the healthy aging brain: a voxel-based MRI and DTI study. J. Alzheimers Dis 18, 553–564.

Jack Jr, C.R., Knopman, D.S., Jagust, W.J., Petersen, R.C., Weiner, M.W., Aisen, P.S., Shaw, L.M., Vemuri, P., Wiste, H.J., Weigand, S.D., Lesnick, T.G., Pankratz, V.S., Donohue, M.C., Trojanowski, J.Q., 2013. Tracking pathophysiological processes in Alzheimer's disease: an updated hypothetical model of dynamic biomarkers. The Lancet Neurology 12, 207–216.

Kanwisher, N., McDermott, J., Chun, M.M., 1997. The fusiform face area: a module in human extrastriate cortex specialized for face perception. J. Neurosci. 17, 4302–4311.

Kim, H., Daselaar, S.M., Cabeza, R., 2010. Overlapping brain activity between episodic memory encoding and retrieval: Roles of the task-positive and task-negative networks. NeuroImage 49, 1045–1054.

Libby, L.A., Ekstrom, A.D., Ragland, J.D., Ranganath, C., 2012. Differential Connectivity of Perirhinal and Parahippocampal Cortices within Human Hippocampal Subregions Revealed by High-Resolution Functional Imaging. J. Neurosci. 32, 6550–6560.

Machulda MM, J.D., 2011. EFfect of apoe ε4 status on intrinsic network connectivity in cognitively normal elderly subjects. Arch Neurol 68, 1131–1136.

Papanicolaou, A.C., Simos, P.G., Castillo, E.M., Breier, J.I., Katz, J.S., Wright, A.A., 2002. The Hippocampus and Memory of Verbal and Pictorial Material. Learn. Mem. 9, 99–104.

Persson, J., Lind, J., Larsson, A., Ingvar, M., Cruts, M., Van Broeckhoven, C., Adolfsson, R., Nilsson, L.-G., Nyberg, L., 2006. Altered brain white matter integrity in healthy carriers of the APOE {varepsilon}4 allele: A risk for AD? Neurology 66, 1029–1033.

Ryan, L., Walther, K., Bendlin, B.B., Lue, L.-F., Walker, D.G., Glisky, E.L., 2011. Age-related differences in white matter integrity and cognitive function are related to APOE status. Neuroimage 54, 1565–1577.

Salat, D.H., Tuch, D.S., Van der Kouwe, A.J.W., Greve, D.N., Pappu, V., Lee, S.Y., Hevelone, N.D., Zaleta, A.K., Growdon, J.H., Corkin, S., Fischl, B., Rosas, H.D., 2010. White

matter pathology isolates the hippocampal formation in Alzheimer's disease. Neurobiol. Aging 31, 244–256.
Seeley WW, 2011. Divergent network connectivity changes in healthy apoe ε4 carriers: Disinhibition or compensation? Arch Neurol 68, 1107–1108.
Squire, L.R., Stark, C.E.L., Clark, R.E., 2004. The Medial Temporal Lobe*. Annual Review of Neuroscience 27, 279–306.
Tambini, A., Ketz, N., Davachi, L., 2010. Enhanced Brain Correlations during Rest Are Related to Memory for Recent Experiences. Neuron 65, 280–290.
Van den Heuvel, M.P., Stam, C.J., Kahn, R.S., Hulshoff Pol, H.E., 2009. Efficiency of Functional Brain Networks and Intellectual Performance. J. Neurosci. 29, 7619–7624.